POLITECNICO DI MILANO

SCUOLA DI INGEGNERIA INDUSTRIALE E DELL'INFORMAZIONE

Corso di Laurea Magistrale in Ingegneria Fisica

ELECTRIC CONTROL OF MAGNETIC PROPERTIES AND ELECTRONIC TRANSPORT IN MULTIFERROIC HETEROSTRUCTURES

Relatore: Prof. MATTEO CANTONI

Correlatori: Prof. RICCARDO BERTACCO

                      Dott. CHRISTIAN RINALDI

Tesi di laurea di:

MARCO ASA

Matr. 800817

Alla mia famiglia.

Abstract

In the last years, the steep rise of the amount of digital information stored and shared worldwide has posed a set of important challenges for research and industry in order to develop new storage technologies that are fast, nonvolatile and energy-efficient.

Among the different solid state technologies under development, the most innovative magnetic memories, based on the MRAM architecture, seem to be able to offer the best performances in terms of speed and reliability. However, the excessive power consumption, due to the high current densities required for magnetic state writing, limits the large-scale applications of these devices.

A potential alternative to current-driven writing in magnetic memories can be found in multiferroic systems that show magnetoelectric coupling. In these systems, coexistence of ferromagnetic (FM) and ferroelectric (FE) ordering and their reciprocal interaction allows a purely electric control of magnetism, with possible applications in low power storage devices.

The present work, carried on in the Nanobiotechnology and Spintronics group of Politecnico di Milano, aims at investigating magnetoelectric coupling effects in composite FE/FM heterostructures, with the goal to realize devices in which the magnetic properties of the

FM could be modified upon application of an electric voltage to the FE. This idea is exploited in two different kinds of devices: ferroelectric capacitors with magnetic electrodes and multiferroic tunnelling junctions.

Key components of ferroelectric capacitors are the FE oxyde $BaTiO_3$ (BTO) and the FM alloy $Co_{0.4}Fe_{0.4}B_{0.2}$ (CoFeB). The dependence of the perpendicular magnetic anisotropy of CoFeB thin films on BTO polarization at room temperature is revealed in these devices by the variation of the magnetic coercive field of CoFeB, measured by magneto-optical Kerr effect.

Multiferroic tunnelling junctions are based instead on the heterostructure $Co/Fe/BaTiO_3/La_{0.67}Sr_{0.33}MnO_3$, where $La_{0.67}Sr_{0.33}MnO_3$ and Co/Fe are the FM electrodes and BTO acts both as tunnel barrier and FE element. In these devices, both tunnelling electroresistance and tunnelling magnetoresistance are indipendently observed. Moreover, ferroelectric control of spin polarization of Fe layer is found, denoted by the dependence of the magnetoresistance values on the barrier polarization.

The magnetoelectric coupling effects shown by these devices finally demonstrate the opportunity of a purely electrical control of the magnetization, thus paving the way to a new generation of low power consumption magnetic memories.

Sommario

L'aumento vertiginoso della quantità di informazione digitale immagazzinata e scambiata ha posto negli ultimi anni ricerca e industria di fronte a importanti sfide per sviluppare nuove tecnologie di memorizzazione veloci, stabili e a basso consumo energetico.

Tra le diverse tecnologie a stato solido in via di sviluppo, le memorie magnetiche più innovative, basate sull'architettura MRAM, sembrano potere offrire le prestazioni migliori in termini di velocità e affidabilità. Tuttavia, l'eccessivo consumo energetico, dovuto alle alte densità di corrente necessarie per la scrittura dell'informazione magnetica, ne limita ancora l'applicazione su larga scala.

Una possibile alternativa alla scrittura per mezzo di correnti nelle memorie magnetiche è fornita dai sistemi multiferroici che presentano accoppiamento magnetoelettrico. In questi sistemi la coesistenza di ordinamento ferromagnetico (FM) e ferroelettrico (FE) e la loro reciproca interazione permette di ottenere un controllo puramente elettrico del magnetismo, con potenziali applicazioni in dispositivi di memorizzazione a basso consumo.

Il presente lavoro, svolto nel gruppo di Nanobiotecnologia e Spintronica del Politecnico di Milano, si propone di investigare possibili fenomeni di accoppiamento magnetoelettrico in eterostrutture compo-

site FE/FM, con l'obiettivo di realizzare dispositivi in cui le proprietà magnetiche del FM possano essere modificate dall'applicazione di una tensione al FE. Questa idea viene applicata a due diversi tipi di dispositivo: capacitori ferroelettrici con elettrodi magnetici e giunzioni multiferroiche ad effetto tunnel.

Gli elementi fondamentali dei capacitori ferroelettrici sono l'ossido FE $BaTiO_3$ (BTO) e la lega FM $Co_{0.4}Fe_{0.4}B_{0.2}$ (CoFeB). La dipendenza dell'anisotropia magnetica perpendicolare dei film sottili di CoFeB dalla polarizzazione del BTO a temperatura ambiente si traduce in questi dispositivi nella variazione del campo coercitivo magnetico del CoFeB, misurato per mezzo dell'effetto Kerr magneto-ottico.

Le giunzioni multiferroiche ad effetto tunnel sono basate invece sull'eterostruttura $Co/Fe/BaTiO_3/La_{0.67}Sr_{0.33}MnO_3$, dove $La_{0.67}Sr_{0.33}MnO_3$ e Co/Fe sono gli elettrodi FM e il BTO svolge la funzione di barriera ed elemento FE. Questi dispositivi presentano indipendentemente sia elettroresistenza che magnetoresistenza per effetto tunnel. Si osserva inoltre un controllo ferroelettrico sulla polarizzazione di spin del Fe, evidenziato dalla variazione dei valori di magnetoresistenza in funzione della polarizzazione della barriera.

Gli effetti di accoppiamento magnetoelettrico mostrati da questi dispositivi dimostrano la possibilità di un controllo puramente elettrico della magnetizzazione, aprendo la strada ad una nuova generazione di memorie magnetiche a basso consumo.

Ringraziamenti

Al termine di questo lavoro sono molte le persone che desidero ringraziare.

Un primo, doveroso e sentito ringraziamento va al Prof. Riccardo Bertacco per avermi offerto la possibilità di svolgere questo lavoro di tesi presso il suo gruppo di ricerca, per il sincero interesse dimostrato al mio lavoro e per tutti i preziosi insegnamenti.

Ringrazio in modo speciale il Prof. Matteo Cantoni per i numerosi consigli ricevuti, per il tempo e per la cura dedicati alla supervisione di questo lavoro. La tesi che tenete in mano non sarebbe mai esistita in questa forma se non grazie a lui.

Ringrazio il Dott. Christian Rinaldi per tutto il tempo e la pazienza dedicati al mio lavoro, per essere stato guida nell'attività di laboratorio e per la grande disponibilità con cui ha sempre chiarito i miei tanti dubbi.

Un enorme grazie va poi a tutto il magnifico gruppo di lavoro per l'amicizia e il supporto.

Grazie a To' e a Ste, i colleghi spintronici che mi hanno dovuto sopportare più degli altri.

Grazie a Daniela, Edo, Sha, Mons e Falcons, che mi hanno perdonato (forse) i continui furti di strumenti (e la PLD costantemente in funzione).

Grazie a Marco e a Lorenzo, perchè i tecnici fanno sempre la parte più importante.

Grazie a Dario e a Matteo, che hanno iniziato con me questa bellissima

esperienza.

Un Grazie va poi agli "Amicis" di sempre (Campi, Chiara, Lollo, Christian, Gaia, Colo, Davide, Ely, Jack, Elj, Mara, Fede, Fra, Gessman, Kappa, Maura, Marty, Mattia, Michele, Nicholas, Ruz, Simone e Vale), perchè su persone come voi si può sempre fare affidamento.

Grazie ai compagni di corso (in particolare Ale, Fabio, Fabri, Gio, LVP, Mara, Marco ($\nabla \times A$), Marghe, Silvio, Tommy e Villa) per aver condiviso con me le fatiche e le gioie del Poli.

Grazie a tutti gli amici della C.R.I. per tutto quello che mi avete insegnato sul piano professionale e umano.

Grazie, grazie di cuore alla compagnia dei Pischifralli che dopo anni riesce ancora a stupirmi; è un piacere e un onore lavorare con voi.

Infine il grazie più grande non può che andare alla mia splendida e numerosa famiglia: ai miei genitori e ai miei fratelli, per avermi offerto sempre dei modelli positivi ed avermi spronato a dare il massimo in ogni occasione. A voi è dedicato questo lavoro.

Contents

List of Figures

List of Tables

Chapter 1

Introduction

At the end of 2013, the amount of digital information stored worldwide was estimated in 4.4 zettabyte (a zettabyte is a trillion of gigabyte or 10^{21} byte), this value doubles approximately every two years and is expected to reach 44 zettabyte by 2020 [1]. This ever-increasing volume of data, as well as the pervasive diffusion of portable computing devices, is pushing new and more challenging demands to information storage technology.

The goal of a fast, high density, nonvolatile memory with special attention to low energy consumption is not currently met by any state of the art technology: magnetic recording in hard disk drives, the conventional method still in widespread use especially in big data facilities, requires electric current to write and erase bits, hindering both high-density integration and power consumption reduction. At the contrary, commercial ferroelectric devices such as FeRAMs have the advantages of high scalability and low power electric field writing, but a complex and destructive read-out process keeps those memories in a niche market.

Among the emerging devices, ferroelectric/ferromagnetic heterostructures that show magnetoelectric (ME) coupling may overcome the disadvantages of each technology taken singularly and pave the way for next generation memories. Growth and characterization of multiferroic structures of this kind will be de-

scribed in detail in this thesis work as well as results that prove the existence of ME coupling.

This first chapter will review current and emerging technologies in information storage, with particular focus on applications of multiferroic systems.

1.1   Survey of Information Storage Technology

Since the beginning of civilization, information recording has been a need for humanity: from runes carved in stones and clay tablets, through characters handwritten or printed on paper, till the billions of *bits* stored in every modern personal computer, increasing density and accessibility of information have always been a priority. In the digital information society we are living, the methods to record and access data have become crucial even more: for this reason multiple types of digital memories have been developed in the last decades and several still coexist in the variegated landscape of information technology. We will distinguish here three classes of memories on the base of their working principle.

- *Magnetic memories*, based on the stable spontaneous magnetization of ferromagnetic materials at room temperature. Data are written applying a magnetic field and read by magnetic head sensors. The development of magnetic memories is presented in section 1.1.1

- *Electrical memories*, in which information is stored in an electrical state. They include conventional Random Access Memories (S-RAM, D-RAM), Read Only Memories (ROM) and FLASH memories. Ferroelectric devices that will be discussed in section 1.1.2 also belong to this class.

- *Optical memories*, in which the digital value is related to reflection or absorption of a laser beam from a surface. Writing and reading of optical memories (CD-ROMs, DVDs) is completely achieved by optical means.

Different recording technologies are employed for different tasks on the base of their characteristics and performances. A comparison of the principal solid state technologies is shown in table 1.1.

Static random access memories (SRAMs) are used for their great read/write speed as low-level cache in microprocessors. As SRAM is actually a CMOS logic circuit it can not be scaled easily, and SRAMs storage capacity is limited to few megabyte. For this reason, main memories in computers are realized with the Dynamic RAM (DRAM) technology, which allows higher density at expense of slower operation speed. DRAMs hold binary information as charge in capacitors but, since capacitors tend to discharge rapidly, a continuous *refresh cycle* is needed to mantain the data stored, raising the power consumption.

Both SRAMs and DRAMs are volatile memories, meaning that they retain the information only as long as they are powered. For data storage, nonvolatile memories such as FLASH or FeRAMs (described in Section 1.1.2) are required. The former are widely used as mass storage devices but suffer of slow write speed, while the latter have intermediate performances and are used for specific applications in embedded systems.

Finally, the MRAM technology (discussed more in detail in Section 1.1.1) offers great performances in terms of speed, density and relaiability, but its ap-

Property	**Memory Type**				
	SRAM	DRAM	FLASH	FeRAM	MRAM
Read	Fast	Moderate	Fast	Moderate	Fast
Write	Fast	Moderate	Slow	Moderate	Fast
Retention	No	No	Yes	Partial	Yes
Endurability	Good	Good	Poor	Poor	Good
Refresh	No	Yes	No	No	No
Density	Low	High	High	Medium	High
Power consumption	Low	High	Low	Low	High

Table 1.1: Performance comparison of principal solid state memory technologies (from [2]).

plications are currently limited by the high power consumption.

1.1.1 Magnetic Storage Technology

The spontaneous magnetization of ferromagnetic materials has been employed in data storage since the early days of computing. In the 50s, magnetic-core memories, based on arrays of ferrite rings in which the sense of magnetization represented the digital information, were introduced and remained the predominant Random Access Memory (RAM) technology for over two decades. In the same period the first magnetic hard disk was presented by IBM (1956) and the technology has kept progressing since that moment until today. In particular the discoveries of magnetoresistive effects in magnetic thin films and heterostructures, Anisotropic Magnetoresistance (AMR) [4], Giant Magnetoresistance (GMR, section 2.1.2) [5] and Tunnel Magnetoresistance (TMR, section 2.1.3) [6], found immediate application in hard disks reading heads, improving by several orders of magnitude the sensitivity of magnetic detection and leading to unprecedented densities of stored information (Figure 1.1). In the years, many other magnetic
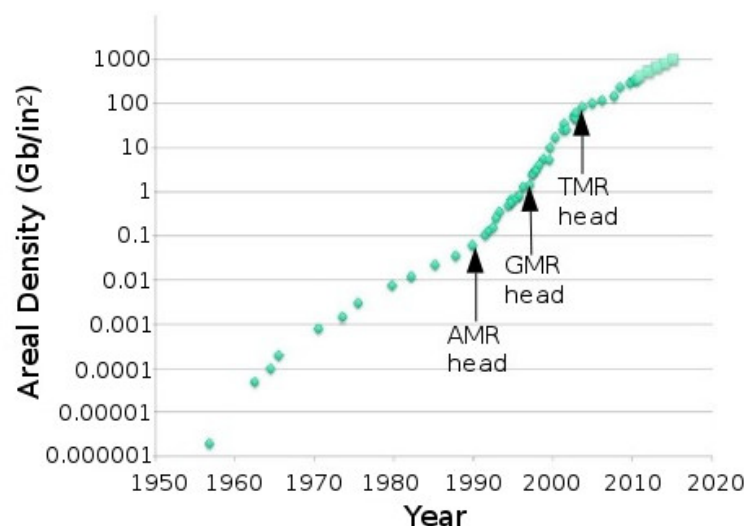
Figure 1.1: Evolution of areal density of information stored in commercial hard disks (adapted from [3]).

storage media have also been investigated and commercialized for different applications, including floppy disks, magnetic recording tapes, and magnetic stripes.

Magnetic storage technology has been successful in hard disk drives for its intrinsic non-volatility and low cost, nonetheless the continuously increasing requirements of density are pushing more challenges that have to be faced. First, the reduction in size of magnetic data cells results in less stable magnetization, and under a certain limit self-demagnetization is unavoidable at room temperature (superparamagnetic limit). Second, a large magnetic field is required to write the state, even more if materials with larger coercive fields are used to avoid the supermaramagnetic limit, thus the power consumption remains high if compared to other solid state technologies such as FLASH or FeRAM. Moreover, the moving parts of hard disks (spinning platters and reading head) increase the energy consumption even more, reducing at the same time the reliability of the storage medium because of the high failure risk of mechanical components.

A developing architecture of memories that try to address these issues, while retaining the advantages of conventional magnetic storage, is the so called Magnetic Random Access Memory or MRAM [7–10] represented in Figure 1.2. Unlike hard disk drives, MRAMs are solid state memories that do not present moving parts. They are based on Magnetic Tunneling Junctions (MTJs) i. e. two mag-
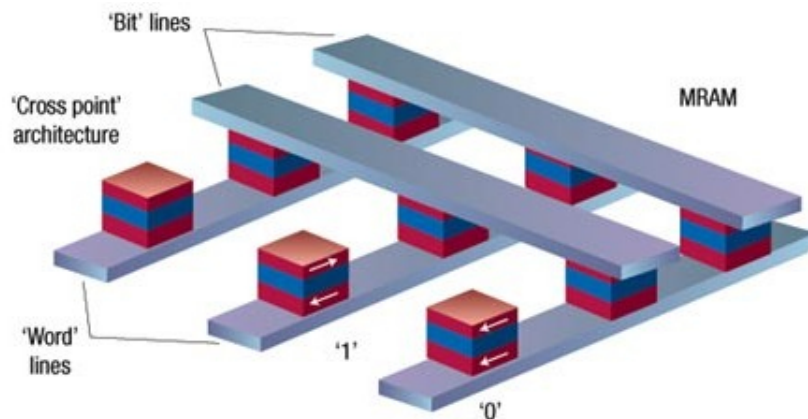
Figure 1.2: Structure of a standard cross-point MRAM architecture (from [7]).

netic films separated by a ultrathin insulating layer. These devices could be used both as mass data storage memories and as fast random access memories, with higher densities with respect to DRAMs and free from the need to refresh continuously the information thanks to the intrinsic stability of the ferromagnetic state. TMR allows easily to read the state of the cell non destructively and with small consumption, while writing may be obtained inducing local magnetic fields with a grid of current lines in a very similar fashion to what was done in magnetic-core memories. In MRAMs, the regular arrangement of current lines shown in Figure 1.2 allows to write a memory cell by composing the magnetic fields generated by the current flowing in the *word line* and in the *bit line* on which the addressed cell lies. Both the word and the bit line generate a magnetic field smaller than the coercive field of the memory cells, and just at the cross-point the sum of the two field is strong enough to write the cell, leaving all the others unchanged.

This cross-point architecture and the use of current lines, of course, limits scalability and reduction of energy consumption, for this reason the use of alternative mechanisms such as Spin Transfer Torque (STT) to flip magnetization is recognized as a better approach (STT-MRAM) [11]. Unfortunately, though, even employing STT, current densities of the order of 10^7 A/cm^2 are still required to write a a magnetic state [12].

In conclusion MRAMs hold potential to become the universal memory, but the problem of high power consumption during the writing process remains a major challenge to be faced before a massive breakthrough of this technology could happen.

1.1.2 Ferroelectric Storage Technology

Ferroelectric materials are named that way in analogy to ferromagnetic ones: while the latter hold a remanent magnetization in absence of magnetic field, ferroelectrics retain a remanent polarization in absence of an applied electric

field. As in the case of the magnetic counterpart, ferroelectric polarization can be switched by an external electrical field and hence used to store information. Here we present the state of the art of ferroelectric memories, while an introduction to the general physics of ferroelectric materials can be found in section 2.2.

The structure of a conventional Ferroelectric Random Access Memory (FeRAM) [13, 14] is illustrated in Figure 1.3a. As pointed out before, to write a state of polarization an electric field sufficiently large is applied to the ferroelectric capacitor. Readout process is slightly more difficult and is illustrated in Figure 1.3b: a voltage is applied as to write a "1" bit in the memory cell, if the ferroelectric is already in the "1" status nothing happens, but if it is in the "0" status the charge movement due to the polarization reversal causes a small current flow that can be detected.

Being the reading voltage sufficient to switch polarization, it is cleat that one of the disadvantages of this memory is the destructive readout (DRO): the ferroelectric polarization will always point in a certain direction at the end of the reading process and a write-after-read cycle is necessary to restore the original information. However, nonvolatile storage, high density, fast access and low power

(a)   (b)
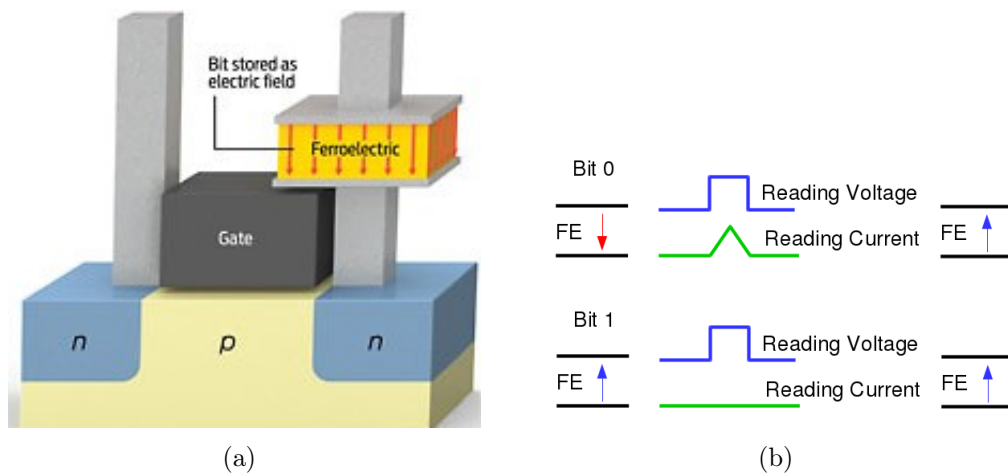
Figure 1.3: **a)**Structure of a FeRAM Device. **b)** Readout process for FeRAM, the ending configuration is the same for both initial states.
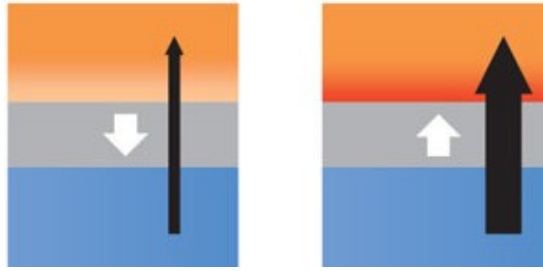
Figure 1.4: Principle of a ferroelectric tunnel junction. The direction of polarization in the ferroelectric (white arrow) influences the charge current (black arrow) between two conducting layers (from [21]).

consumption make FeRAMs a peculiar memory among the currently available commercial technologies, and its use is growing in embedded systems.

Another kind of ferroelectric memory currently in development is the Ferroelectric Tunneling RAM (FTRAM) [15]. This technology is based on the Tunneling Electroresistance (TER, discussed in detail in section 2.2.1) characteristic of asymmetrical ferroelectric tunnel junctions (FTJs). According to the sense of polarization the junction exhibits a variation of resistance (Figure 1.4) with an ON/OFF ratio, i. e. the ratio between highest and lowest resistance, up to 10^4 [16, 17]. For this reason, to read the status is sufficient to apply a small voltage much lower than the writing voltage and readout can be accomplished non destructively.

FTRAMs retain all other advantages of FeRAMs and are a promising technology for applications. Moreover some architectures show good memristive behaviour [18–20] and may be employed in the future as analogic memories in adaptive circuits. However, ultrathin ferroelectric film growth is still an embryonic field and better control of film properties have to be attained before large scale production could take place.

1.2 Applications of Multiferroics in Information Storage

We have seen that ferromagnetic and ferroelectric materials are interesting in themselves for information storage technology: magnetic recording grants easy reading and non-destructive readout (NDRO) but is limited in storage density and writing power consumption; commercial ferroelectric memories, by the contrary, offer high density and low writing energy, but requires complex and destructive readout . The ideal solution would be of course to combine the advantages of both ferromagnetic and ferroelectric memories in a single device and this justifies the rampant interest in multiferroic systems [22]. The word multiferroic
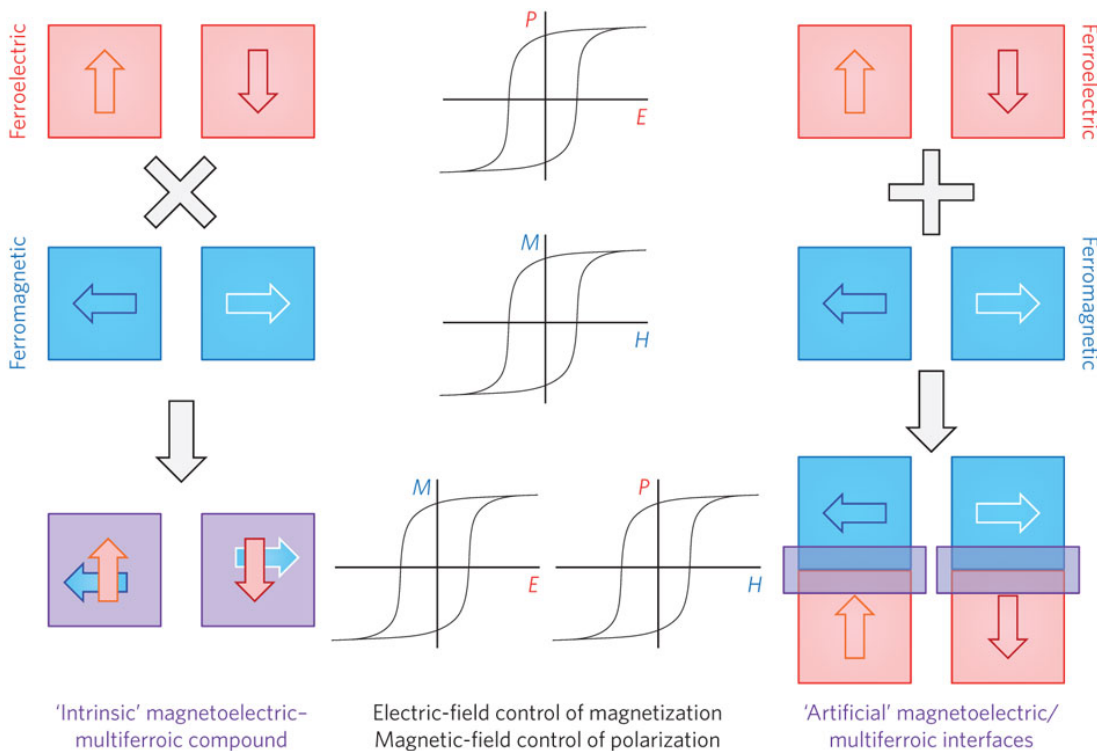
Figure 1.5: Schematic representation of a single phase multiferroic compound (left) and a composite multiferroic interface (right). In both systems, ferromagnetic and ferroelectric orders may coexist and influence each other through magnetoelectric coupling (from [21]).

defines materials and structures which exhibits (at least) two of the four ferroic orders (ferromagnetism, ferroelectricity, ferroelasticity, ferrotoroidism) [21]). Of particular interest for the scope of this work are multiferroics that present a magnetoelectric (ME) coupling between magnetic and electric order (Figure 1.5), as they may hold great potential to improve the performances of memory devices [21, 23]. Unfortunately the few multiferroic materials in nature exhibit weak ME coupling and often only below room temperature [24, 25], thus limiting applications in memory devices. Greater interest comes instead from *composite multiferroics* systems, i. e. heterostructures made of interacting single phase ferroelectric and ferromagnet. Several groups [26–30] reported results in which devices of this kind were employed with encouraging results in electric-field control of magnetizazion and multistate memory devices. Some of these results will be briefly reviewed in the following sections.

1.2.1 Electric Control of Magnetization

The issue of power consumption in magnetic based memories is bounded to the need of electric currents to write a magnetic state. Magnetoelectric coupling opens a different perspective, in which electric fields are used to control magnetization instead of currents. On the base of this idea, in year 2008, Bibes *et al.* [31] proposed the concept of electric-writing and magnetic-reading random access memories (MERAMs) by fabrication of MTJs on top of a multiferroic layer.

Electric-field control of magnetization have been demonstrated in a large variety of single phase Ferroelectric/Ferromagnetic heterostructures such as $BaTiO_3/CoFe_2O_4$ [32], $BaTiO_3/Fe$ [33, 34], $BaTiO_3/Ni$ [35], PMN-PT/CoFeB [36] and so on. Polarization can affect magnetization in several ways and some examples are shown in Figure 1.6.

Ferroelectric control of the Curie temperature (Figure 1.6a) has been demon-

strated in $La_{0.8}Sr_{0.2}MnO_3/PbZr_{0.2}Ti_{0.8}O_3$ bilayers [37]. Toggling between paramagnetic and ferromagnetic state (Figure 1.6b) has been predicted for palladium [38] and a switch from ferromagnetic to antiferromagnetic ordering has been observed at $Fe/BaTiO_3$ interface [30]. Spin polarization at the interface between a ferromagnet and a ferroelectric may also be tuned by the ferroelectric polarization direction [39–42] (Figure 1.6c). This effect has been demonstrated experimentally by observing the polarization dependence of the TMR in MTJs
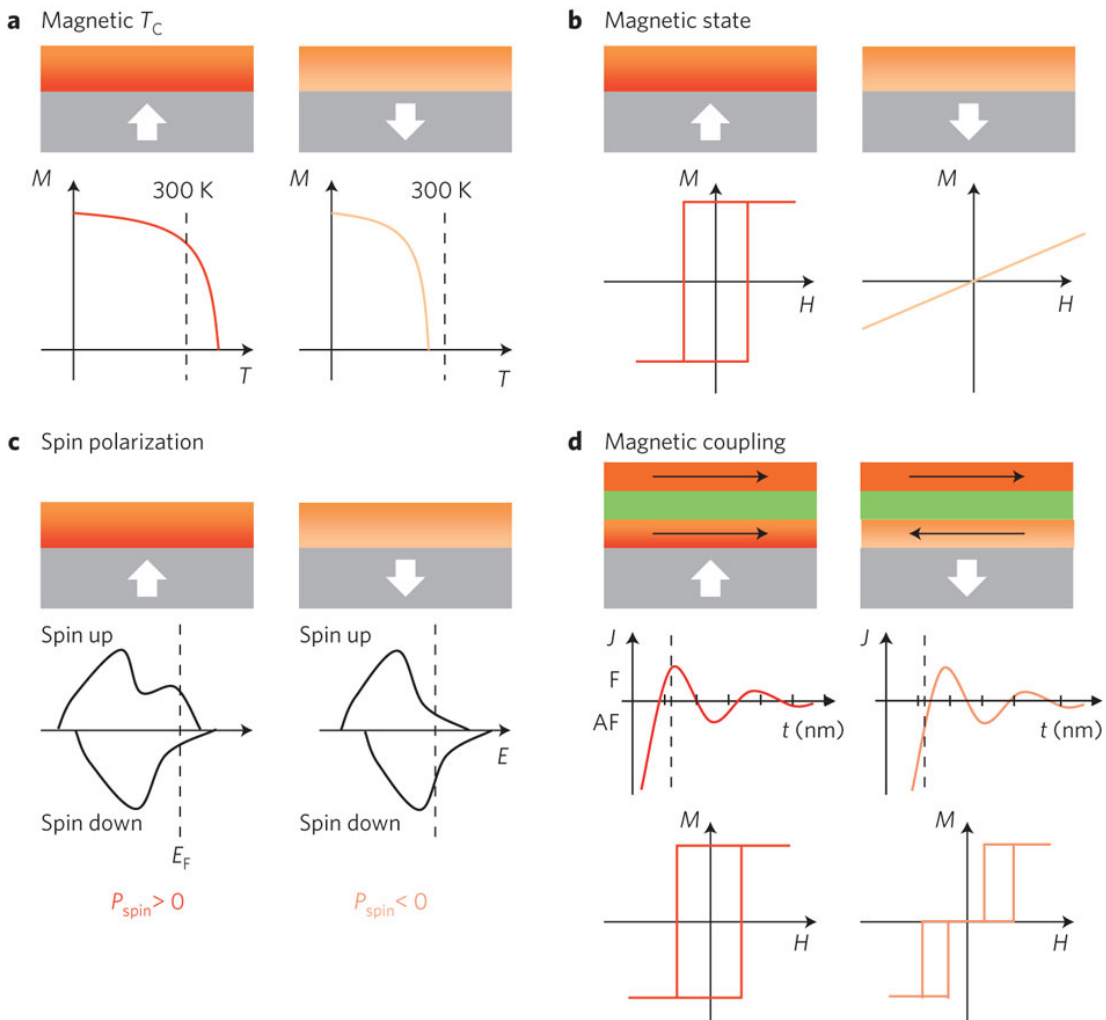
Figure 1.6: Possible effects of coupling with a ferroelectric in magnetic films: **a)** Control of the Curie Temperature. **b)** Magnetic toggling. **c)** Change in spin population. **d)** Modification of interlayer coupling (from [21]).

with a ferroelectric barrier [26, 29, 43].

All these interfacial magnetoelectric effects could be in principle amplified by combining them with bilinear exchange coupling. Magnetic layers separated by a thin nonmagnetic spacer are either coupled parallel or antiparallel, and the sign of the coupling depends on spacer thickness and interfaces magnetization [44]. By changing magnetic properties by means of a ferroelectric, it has been predicted a switch of the multilayer configuration from ferromagnetic to antiferromagnetic that may be employed in electrically controlled GMR devices [45] (Figure 1.6d).

A fifth different effect that could be exploited is the ferroelectric control of magnetic anisotropy. This method is particularly appealing because the magnetic anisotropy determines stable orientations of magnetization, and tailoring the anisotropy of a ferromagnetic film by means of electric fields could allow a switching of the magnetic moment. This magnetoelectric effect has been object of investigation by the group in which this thesis has been done. Preliminary results obtained on CoFeB/ $BaTiO_3$ structures have been reported in [46] and exhaustive characterization on devices of this kind is presented in chapter 4.

1.2.2 Magnetoelectric Multistate Systems

Coexistence of ferroelectric and ferromagnetic order in a single device may offer another advantage in information storage technology: in fact the two polarization states and the two magnetization states can be used to store two independent binary informations, thus realizing a four states memory. The idea in this case is to employ the ferroelectric material as the barrier in the MTJ, instead of conventional non-ferroelectric insulators (MgO, Al_2O_3), and combine TMR and TER effects to distinguish the four different cases (Figure 1.7c).

The first of this kind of Multiferroic Tunneling Junctions (MFTJs) was reported by Gajek *et al.* in 2007 in $Au/La_{0.1}Bi_{0.9}MnO_3/La_{0.67}Sr_{0.33}MnO_3$ heterostructures, exploiting the intrinsic multiferroicity of the barrier at low tem-
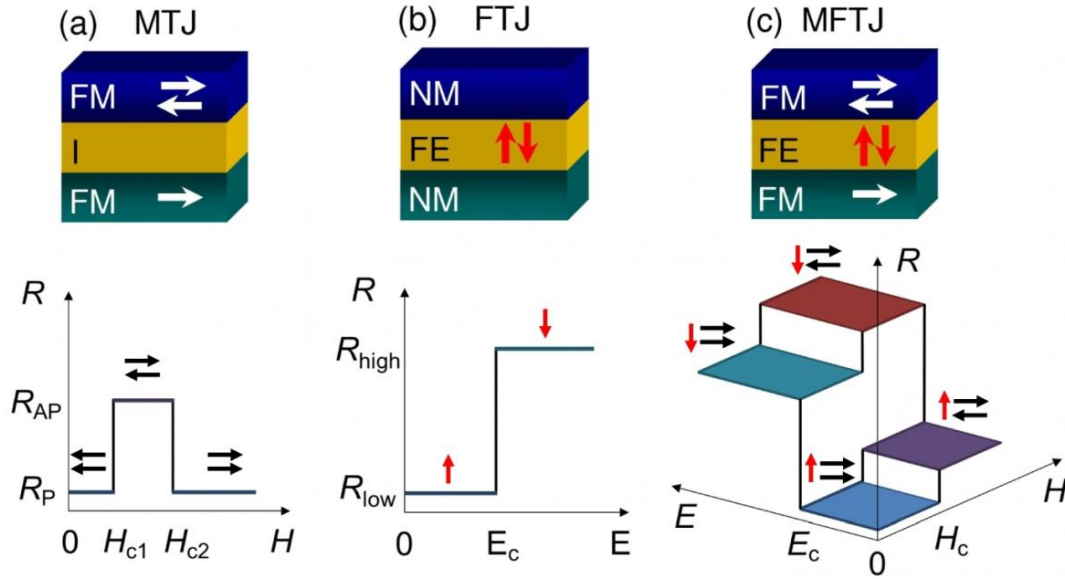
Figure 1.7: Comparison of MTJ, FTJ and MFTJ. **a)** Magnetic Tunnelling Junctions exhibit two resistive states for parallel and antiparallel alignment of magnetizations. **b)** Ferroelectric Tunnelling Junctions exhibit two resistive states for up and down polarization. **c)** Multiferroic Tunnelling Junctions show four states of resistance for combination of magnetic alignment and ferroelectric polarization.

peratures [47]. Subsequently ferroelectric control of spin tunneling was demonstrated in Fe/BaTiO$_3$/ La$_{0.67}$Sr$_{0.33}$MnO$_3$ [26], Co/BaTiO$_3$/ La$_{0.67}$Sr$_{0.33}$MnO$_3$ [43] and Co/PbZr$_{0.2}$Ti$_{0.8}$O$_3$/ La$_{0.67}$Sr$_{0.33}$MnO$_3$ [29] junctions, always below room temperature. MFTJs working at room temperature were first demonstrated by Yin *et al.* in all-oxide La$_{0.67}$Sr$_{0.33}$MnO$_3$/Ba$_{0.95}$Sr$_{0.05}$TiO$_3$/La$_{0.67}$Sr$_{0.33}$MnO$_3$ heterostructures [28].

In this work, fully epitaxial Fe/BaTiO$_3$/ La$_{0.67}$Sr$_{0.33}$MnO$_3$ MFTJs have been investigated and the results are reported in Chapter 5.

1.3   Thesis Outlook

As stated before, investigation of multiferroic systems which exhibit magnetoelectric coupling is interesting not only for its underlying fundamental physics, but

also for the severe impact that may have on storage technology applications. This thesis work is focused on the study of magnetoelectric (ME) coupling in composite multiferroic systems with the aim to demonstrate ferroelectric control of magnetization, both in single ferromagnetic layers and in complex heterostructures. Two different devices will be discussed in the text: the first will show electric control of interface magnetic anisotropy of $Co_{0.4}Fe_{0.4}B_{0.2}$ ultrathin films grown on top of ferroelectric $BaTiO_3$ (BTO) capacitors; the second, based instead on the coupling between BTO and epitaxial iron in $Fe/BTO/La_{0.67}Sr_{0.33}MnO_3$ MFTJs, will demonstrate ferroelectric control of spin polarization and TMR of the junction.

The project has been carried on in the NanoBiotechnology and Spintronics (NaBiS) group of Politecnico di Milano, coordinated by professor Riccardo Bertacco . The thesis work has been done at the L-NESS (Laboratory for Nanostructure Epitaxy and Spintronics on Silicon), at Polo Regionale di Como of Politecnico di Milano.

In the next chapters the results obtained during my thesis work will be presented, along with the underlying theory and the methods of fabrication and characterization employed.

Chapter 2 includes foundamental theory of ferromagnetic and ferroelectric materials, spin dependent transport and magnetoelectric coupling.

Chapter 3 describes growth techniques, the lithographic process and characterization methods.

Chapter 4 presents the investigation of CoFeB/BTO heterostructures and the results in electric control of magnetization.

Chapter 5 exposes the design and realization of $Fe/BTO/La_{0.67}Sr_{0.33}MnO_3$ multiferroic tunneling junctions and preliminary results of transport measurements in different polarization and magnetization states.

Chapter 2

Theory

In this chapter the basic physics behind multiferroic devices is exposed. Sections 2.1 and 2.2 introduce ferromagnetism and ferroelectricity, describing similarities and differences between the two phenomena and the related magnetoresistive/electroresistive behaviour in nanoscale heterostructures.

Section 2.3 is dedicated instead to the coupling between magnetic and electric ordering, starting from the general definition of multiferroic single-phase crystals to specific applications in composite multiferroics.

2.1   Ferromagnetism

Ferromagnetic materials exhibit a long-range ordering at the atomic level which causes the unpaired electron spins to line up parallel with each other in a region called a domain. In these materials, macroscopic magnetization can be changed reordering domains by means of an external magnetic field and the switching is associated to an hysteresis loop (Figure 2.1).

The origin of magnetic ordering is the exchange interaction between electrons. Depending on the electronic arrangement within the atoms and the crystalline structure, a parallel alignment of magnetic moments may be favoured: if this
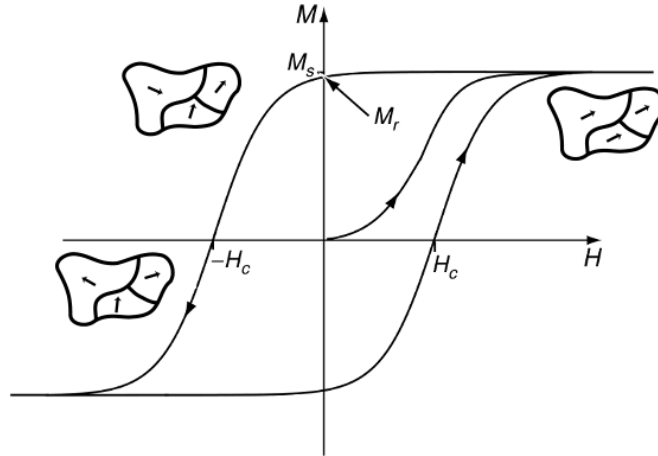
Figure 2.1: Magnetic domains and magnetic hysteresis loop in ferromagnetic materials (from [48]).

happens ferromagnetic order is enstablished [49].

2.1.1 Spin Polarization in Ferromagnets

In ferromagnetic materials, the asymmetry between electrons with opposite spin results in the splitting of the bands corresponding to the density of states (DOS) of the two electron populations as shown in Figure 2.2. The lower band in energy is called the *majority*-spin electrons band, while the higher one is the *minority*-spin electrons band.

Since electrons tend to occupy lower states in energy, the majority band is more populated, the difference of population between majority and minority spin band accounts for the spontaneous magnetization of ferromagnets.

This simplified representation also helps to introduce the concept of spin dependent transport. Only electrons with energy near to the Fermi level participate to transport phenomena and the DOS at Fermi level is different for minority and majority spins. This determines an intrinsic spin *polarization* of the current flowing in a ferromagnet that is given by

$$P = \frac{N_\uparrow(E_f) - N_\downarrow(E_f)}{N_\uparrow(E_f) + N_\downarrow(E_f)} \tag{2.1}$$
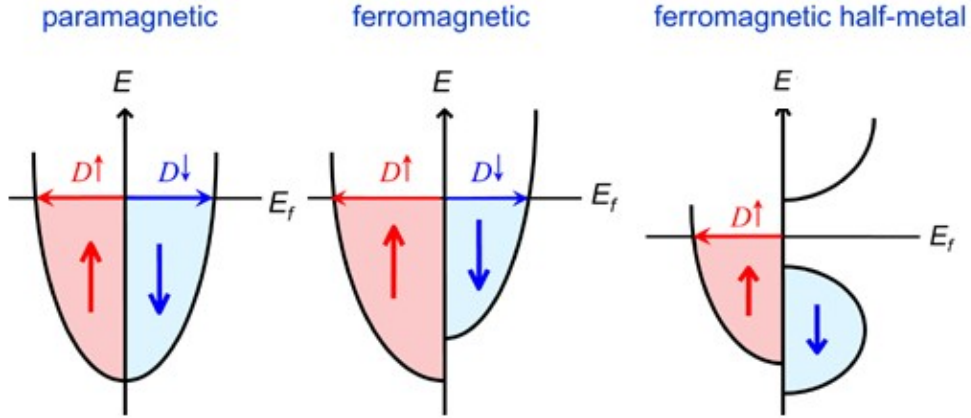
Figure 2.2: Simplified representation of the density of states in paramagnetic, ferromagnetic, and half-metal ferromagnetic materials. In ferromagnetic materials splitting of the bands is determined by exchange interaction that favours parallel alignment. In the case of an half-metal ferromagnet the density of states for minority-spin electrons is zero at the Fermi level, so that only majority-spin electrons are present and the population is 100% spin polarized.

where $N_{\uparrow(\downarrow)}$ corresponds to the density of states at Fermi level for majority (minority) spin.

In a non magnetic material there is no splitting of the DOS and the two bands are equally populated as shown in Figure 2.2a, so that spin-polarization P is zero. In a ferromagnetic material the spin splitting (Figure 2.2b) determines a polarization comprised between 0 and 1. As an extreme case, if minority-spin DOS at Fermi level is zero (Figure 2.2c), the polarization approaches 1 and ideally all the current flowing is carried by electrons with the same spin. This situation is proper of ferromagnetic half-metals such as $La_{0.67}Sr_{0.33}MnO_3$ and CrO_2 [50].

2.1.2 Giant Magnetoresistance

Giant Magnetoresistance (GMR) arises from the spin-dependent scattering of electrons in superlattices made of alternating ferromagnetic and nonmagnetic metals. The effect was first observed by Baibich *et al.* in 1988 in Fe/Cr superlattices [5] and independently by Binasch *et al.* [51]. For the discovery of GMR,

Albert Fert and Peter Grünberg were awarded the Nobel Prize in Physics in year 2007.

The origin of GMR can be understood considering different scattering coefficients for majoritary and minoritary spins in magnetic materials and at interfaces. In the *two-current model*, total conductivity can be expressed as sum of separate contributions from majority and minority electrons in the assumption that spin is preserved (spin flip events are neglected, so that the currents correspondings to the two different spins flow in parallel). Figure 2.3a shows the basic idea: parallel alignment of the magnetic moments of subsequent layers causes one spin channel to experience very high conductance, hence the total resistance, given by the parallel resistance of the two channels, is low (Figure 2.3b). Antiparallel alignment instead determines low conductance for both channels as electrons encounter a region in which scattering is more probable and the total resistance is high .

In these GMR devices, ferromagnetic films are held in antiparallel configuration at zero field thanks to exchange coupling. In this configuration scattering is maximum and device resistance is high. However, if parallel alignment of magne-
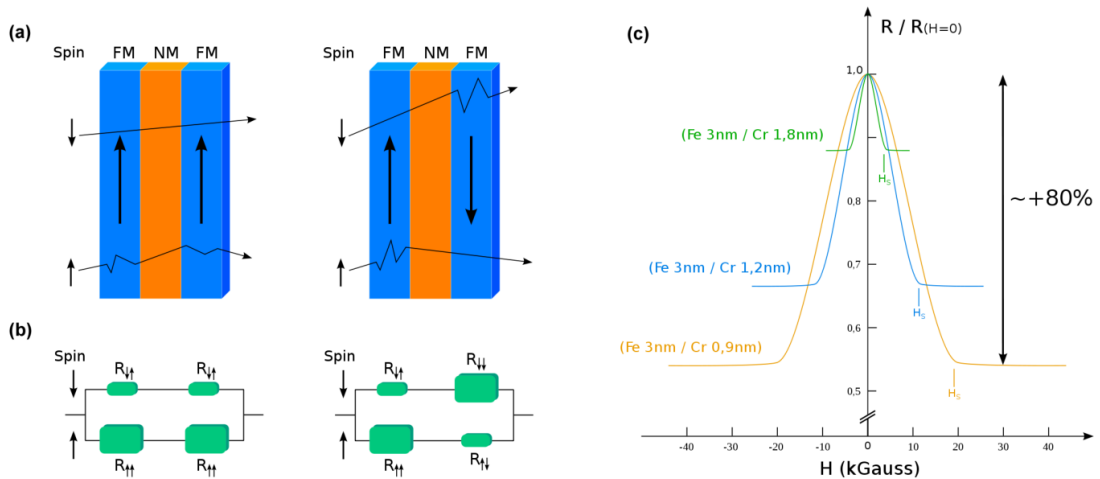
Figure 2.3: **a)** Representation of spin-dependent scattering and **b)** equivalent circuit in the two currents model. **c)** GMR at 4.2K in Fe/Cr superlattices for different Cr thicknesses [5]

tizations is forced through application of a large magnetic field a lower resistance is measured (Figure 2.3c).

The value of magnetoresistance is defined as

$$MR = \frac{R_{AP} - R_P}{R_P} \tag{2.2}$$

where R_{AP} is the resistance in the antiparallel state and R_P the resistance in the parallel state. In the pioneering work of Baibich *et al.* [5] on Fe/Cr/Fe multilayers, a GMR of 80% was measured at 4.2K and of 20% at 300K for a chromium thickness of 9Å. Being the effect seizable at room temperature and the ratio $\Delta R/R$ independent of area, GMR devices were well suited for circuit integration, that actually happened in few years [52].

2.1.3   Tunnel Magnetoresistance

Magnetoresistance in Ferromagnet/Insulator/Ferromagnet tunneling junctions was first studied by Julliére in 1975 [6]. As in the case of GMR, also in these structures a change of resistance is observed in case of antiparallel or parallel magnetizations. Julliére accounted for this behaviour completely within the spin split band representation discussed in section 2.1, in a simple model that neglects both tunnelling matrix elements and scattering events that may lead to a spin flip, so that, in a first approximation, transmission is proportional to the DOS on both sides of the barrier.

The idea is illustrated in Figure 2.4. In parallel state the DOS at Fermi level for one of the spin channels (minority in this case) is high at both sides of the barrier, determining a relatively high tunnelling probability and hence a low resistance. In antiparallel state instead, both spin-up and spin-down channels experience low tunneling probabilities, as they tunnel from a region with high DOS to a region with low DOS or viceversa.

On the base of this model Julliére derived a simple expression, equivalent to
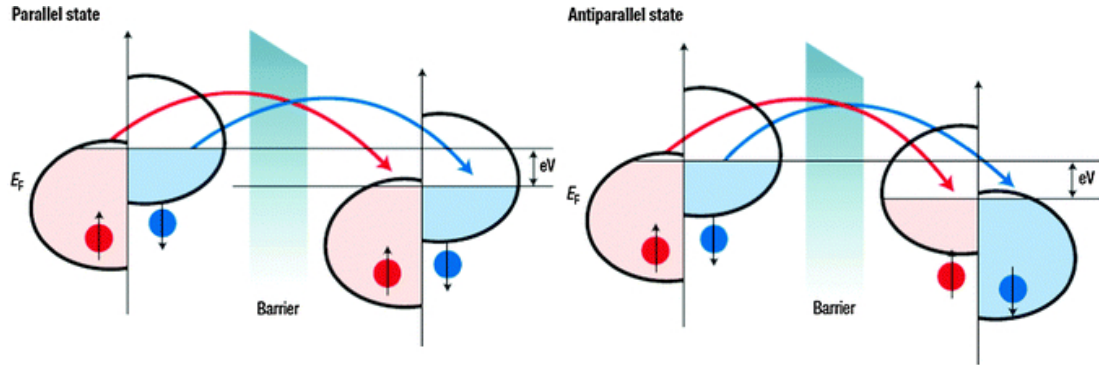
Figure 2.4: Two-current model for parallel and anti-parallel alignment of the magnetizations. In the case of parallel magnetizations, electrons will more easily find free states to tunnel to and the tunnelling probability is relatively high. For antiparallel magnetization, both the majority and minority spin channels experience lower tunnelling probabilities (from [7]).

the general definition of eq. 2.2, to express TMR in terms of spin polarization:

$$TMR = \frac{2P_1 P_2}{1 - P_1 P_2} \qquad (2.3)$$

P_1 and P_2 are the spin polarizations calculated as in eq. 2.1 for the left and right electrode respectively.

Record values of TMR up to 600% at room temperature and over 1100% at 4.2 K were observed in junctions of CoFeB/MgO/CoFeB [53]

2.2 Ferroelectricity

Whereas ferromagnetic materials present an asymmetry in spin, ferroelectric materials show instead an asymmetry in charge. This determines two discrete states of non zero electric polarization that can be reversed by a external electric field [54]. As in the case of ferromagnetic materials, ferroelectric switching is associated to an hysteresis cycle (Figure 2.5a).

In order to exhibit spontaneous polarization a material must have a non-centrosymmetric unit cell. In most of the ferroelectrics this is possible thanks

to the distortion (second order Jahn-Teller distortion) of a non-polar centrosymmetric prototype phase. The distortion causes displacement of ions inside the crystal unit cell and the formation of an electric dipole [56].

Typical examples of materials that show this behaviour are the ferroelectric perovskite oxides like $BaTiO_3$, that will be employed in this work. Perovskite oxides have structure ABO_3 where A and B are two different metallic cations. Under specific conditions, the cubic prototype phase of this crystals undergoes a distortion to lower its potential energy by shifting either A or B cations (or both) as shown in Figure 2.5b.

The local offcentering of ions alone is not sufficient to grant net macroscopic polarization: ferroelectrics analogously to ferromagnets require long range ordering. In this case, the role that quantum exchange has in magnetism is taken by dipole-dipole interactions. In $BaTiO_3$ this purely electrostatic effect favours ferroelectric ordering as demonstrated also by first principles calculations [57].

(a)   (b)
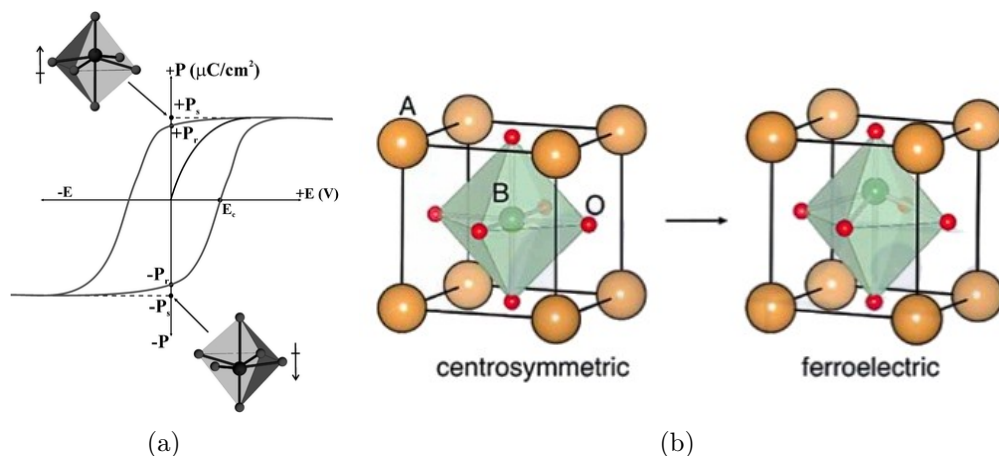
Figure 2.5: **a)** Ferroelectric hysteresis loop (from [55]) **b)** Centrosymmetric prototype unit cell of a perovskite with ABO_3 structure (left) and non-centrosymmetric distorted perovskite unit cell (right). The distorted structure may develop ferroelectricity if long range ordering of dipoles is favoured.

2.2.1 Tunneling Electroresistance

The concept of ferroelectric tunneling junctions was proposed by Esaki back in 1971 [58], however, at that time, there were no experimental techniques and capabilities to fabricate ferroelectric ultrathin films. Moreover, it was believed that the critical thickness for ferroelectricity was much higher than the few nanometers necessary for tunnelling to take place. Only with the discovery of ferroelectricity in nanometer-thick films [59, 60] FTJs have received again the attention of the scientific community.

The simplified band profile of a tunnelling junction with a ferroelectric barrier is shown in Figure 2.6. Polarization influences the band profile as the ferroelectric charges repel or attract electrons at metal interfaces and the incomplete screening of these charges gives rise to an additional electrostatic potential.

If we consider an asymmetric FTJ in which one electrode screens charges more efficiently than the other, the additional electrostatic potential will be different at the two interfaces as it depends on the ratio between screening length and
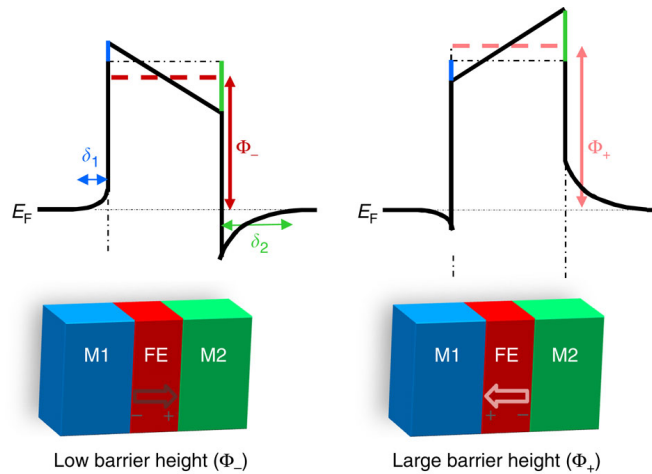
Figure 2.6: Polarization-induced variation of the tunnel barrier height in FTJs and potential profile across the metal 1 (M1)/ferroelectric/metal 2 (M2) heterostructure for two orientations (right and left) of the ferroelectric polarization (P). Ferroelectric charges are more efficiently screened in M1 than in M2 and, owing to electrostatic effects, the average barrier height is small (Φ_-) or large (Φ_+), when P points to the right or to the left, respectively (from [15]).

dielectric constant. In such a system, ferroelectric charge induces an asymmetric modulation of the electronic potential profile that is reversed by changing the polarization verse. As shown in Figure 2.6, this results in a greater average barrier height when polarization points towards the most screening-efficient electrode.

Since the tunnel transmission depends exponentially on the square root of the barrier height, the junction resistance will depend on the direction of polarization. The figure of mertit of this change of resistance is the tunnelling electroresisance ratio.

$$TER = \frac{R_{OFF} - R_{ON}}{R_{ON}} \tag{2.4}$$

R_{OFF} and R_{ON} are the highest and lowest states of resistance, respectively, measured in opposite states of polarization.

Besides the electrostatic effect, some other mechanisms related to ferroelectric polarization may contribute to the change of tunnelling resistance. The displacement of atoms in the barrier for opposite polarization orientations, for instance, may affect the atomic orbital hybridizations at the ferroelectric/metal interface determining a different transmission probability. Or else, polarization dependent strain of the ferroelectric material can modify the barrier width and consequently the tunnelling probability [61].

2.2.2   Brinkman model

To evaluate the role of electrostatic TER effect, Brinkman model for trapezoidal potential barriers [62] is commonly employed in FTJs characterization [26,63–65].

Assuming a barrier of width d and potential steps at the interfaces ϕ_1 and ϕ_2, Gruverman *et al.* [63] derived the following equation for tunnelling current

density J in the WKB approximation.

$$J \simeq C \frac{\exp\left\{\alpha(V)\left[\left(\phi_2 - \frac{eV}{2}\right)^{3/2} - \left(\phi_1 + \frac{eV}{2}\right)^{3/2}\right]\right\}}{\alpha^2(V)\left[\left(\phi_2 - \frac{eV}{2}\right)^{1/2} - \left(\phi_1 + \frac{eV}{2}\right)^{1/2}\right]^2} \times$$

$$\sinh\left\{\frac{3}{2}\alpha(V)\left[\left(\phi_2 - \frac{eV}{2}\right)^{1/2} - \left(\phi_1 + \frac{eV}{2}\right)^{1/2}\right]\frac{eV}{2}\right\} \tag{2.5}$$

where $C = -\frac{4em^*}{9\pi^2\hbar^3}$, $\alpha = \frac{4d(2m^*)^{1/2}}{3\hbar(\phi_1 + eV - \phi_2)}$, being m^* the effective tunnelling electron mass.

The parameters in this equation can be obtained by fitting current-voltage characteristics of FTJs. Of particular interest are the values of ϕ_1 and ϕ_2 and their variation in different polarization states, as it allows to quantify the change of the average barrier height that gives rise to TER.

2.3   Magnetoelectric coupling

Magnetoelectric coupling, in its most general definition, describes the interaction between electric and magnetic fields in matter (i. e. induction of magnetization (M) by an electric field (E) or polarization (P) by a magnetic field (H) as shown in Figure 1.5).

The general framework in which ME coupling could be described is the Landau theory of phase transitions [23,66]. The free energy F of a magnetoelectric system under an external electric field **E** and magnetic field **H** can be expanded as follows:

$$F(\mathbf{E}, \mathbf{H}) = F_0 - P_i^s E_i - M_i^s H_i - \frac{1}{2}\epsilon_0\epsilon_{ij}E_iE_j - \frac{1}{2}\mu_0\mu_{ij}H_iH_j +$$

$$- \alpha_{ij}E_iH_j - \frac{\beta_{ijk}}{2}E_iH_jH_k - \frac{\gamma_{ijk}}{2}H_iE_jE_k - \dots \tag{2.6}$$

where F_0 represents the ground state free energy, P_i^s and M_i^s the components of

spontaneous polarization and magnetization, $\epsilon_0\epsilon_{ij}$ and $\mu_0\mu_{ij}$ the dielectric constant and magnetic susceptibility of the material, and α_{ij}, β_{ijk}, γ_{ijk} the first order and higher order ME coupling coefficients. Different components of electric and magnetic fields are denoted by E_i, E_j, E_k, and H_i, H_j, H_k, respectively.

By differentiating Eq. 2.6 with respect to E_i and H_i respectively one gets the following expressions for P_i and M_i [23]:

$$
\begin{aligned}
P_i(\mathbf{E}, \mathbf{H}) &= -\frac{\partial F}{\partial E_i} \\
&= P_i^s + \epsilon_0\epsilon_{ij}E_j + \alpha_{ij}H_j + \frac{\beta_{ijk}}{2}H_jH_k + \gamma_{ijk}H_iE_j + \ldots
\end{aligned}
\tag{2.7}
$$

$$
\begin{aligned}
M_i(\mathbf{E}, \mathbf{H}) &= -\frac{\partial F}{\partial H_i} \\
&= M_i^s + \mu_0\mu_{ij}H_j + \alpha_{ij}E_j + \beta_{ijk}E_iH_j + \frac{\gamma_{ijk}}{2}E_jE_k + \ldots
\end{aligned}
\tag{2.8}
$$

From Eqs. 2.7 and 2.8 one can see the interdependence between the ferroelectric order and the ferromagnetic order in multiferroic materials, provided that at least one of the terms α_{ij}, β_{ijk}, γ_{ijk} is non zero. The control of polarization by means of a magnetic field (Eq. 2.7) is called magnetoelectic coupling, while the control of magnetization by means of an electric field (Eq. 2.8) is defined *converse* magnetoelectric coupling.

Values of the α coefficients in single phase material are tipically in the order of $10^{-13} - 10^{-11}$ s/m with a record value of $4.6 \cdot 10^{-10}$ s/m for TbPO$_4$ at 2 K [67]. For comparison, the record magnetoelectric coupling constant in composite multiferroics corresponds to $\alpha = 2 \cdot 10^{-15}$ s/m, as reported by Radaelli *et al.* [30] for Fe/BaTiO$_3$ interface at room temperature. This specific case will be discussed in more detail in the next section.

2.3.1   Ferrolectric Control of Magnetization in Fe/BaTiO$_3$

Among other FM/FE structures, Fe/BaTiO$_3$ has emerged as a prototypical composite multiferroic interface. Both these materials possess robust ferroic order at room temperature and a negligible lattice mismatch (1.6%), that allows for the epitaxial growth of heterostructures embedding Fe and BaTiO$_3$ [68]. For this reason, multiferroic structures of this kind have been widely investigated also by the group where my work has been done [30, 33, 34], and will be the subject of part of this work.

In the first work on direct (i. e. not strain mediated) ME effects, Duan *et al.* predicted with density-functional calculations that ME coupling could arise in the ideal Fe/BaTiO$_3$ (001) multilayer (Figure 2.7a) from a change of interface bonding configuration [39].

Fe magnetization is affected by displacement of Ti atoms due to ferroelectric polarization. The upward polarization pushes Ti atoms towards the interface (Figure 2.7a) and reduce the Fe-Ti bond length. Hybridization between 3d orbitals of Fe and Ti results in a minority-spin bonding state lying below the Fermi
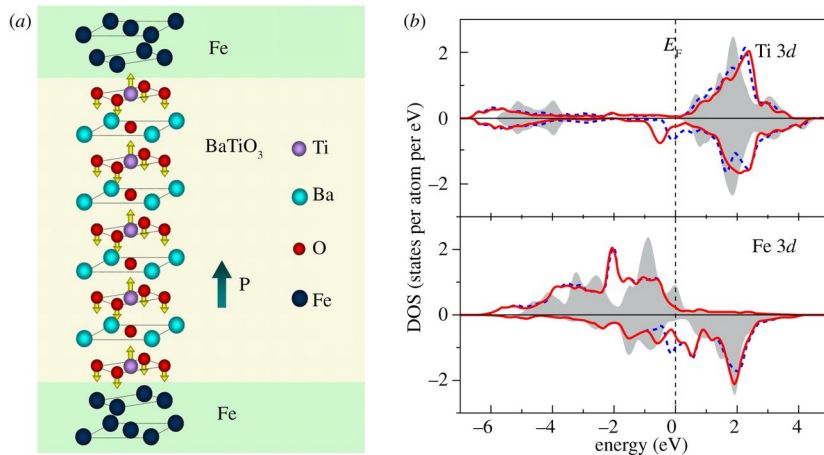
Figure 2.7: **a)** Atomic structure of Fe/BaTiO$_3$/Fe multilayer. **b)** Orbital-resolved DOS for Ti and Fe at BaTiO$_3$/Fe interface. Red solid line and blue dashed line represent DOS for upward and downward polarization respectively. Shaded plots are DOS for atoms far form the interface that can be regarded as bulk (from [39]).

level. For downward polarization, the smaller overlap between orbitals causes a shift in energy of the bonding state, thus giving rise to a considerable difference in the interface DOS in the two ferroelectric states (Figure 2.7b).

A greater magnetoelectric effect of quantum origin has been recently reported by Radaelli *et al.* at the same interface [30]. In this work, a transition from ferromagnetic to antiferromagnetic ordering of the first layer of oxidized Fe at the interface with $BaTiO_3$ has been demonstrated experimentally by means of X-ray Magnetic Circular Dichroism (XMCD). Part of the work has been done in the laboratories where my thesis took place and represents the starting point for the realization of the multiferroic tunnelling junctions that will be discussed in chapter 5.

To observe the magnetic transition of interfacial Fe atoms, X-ray absorption
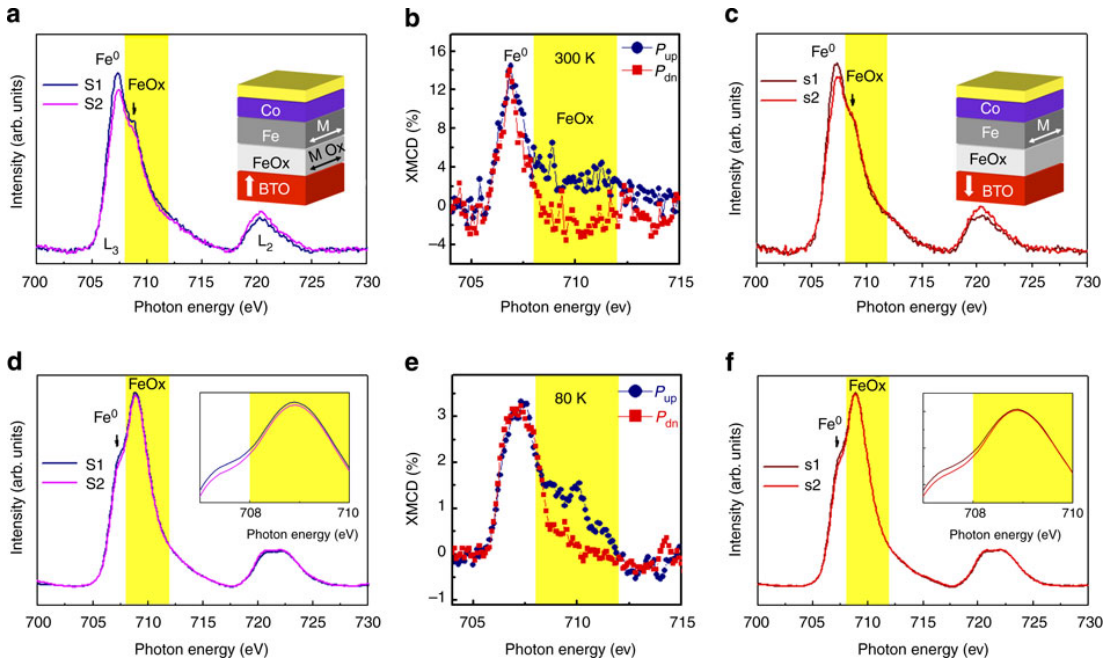
Figure 2.8: **a,c)** XAS Fe–$L_{2,3}$ spectra taken at 300K after upward and downward polarization of $BaTiO_3$ (BTO). **d,f)** XAS Fe–$L_{2,3}$ spectra taken at 80K after upward and downward polarization of BTO. **b,e)** XMCD signal in the Fe-L_3 energy region for upward BTO polarization (blue circles) and downward (red squares) (from [30]).

spectra of Fe-$L_{2,3}$ edge have been taken at 300 K and 80 K for both polarization directions (Figure 2.8). By taking the difference between absorption spectra obtained with left and right circularly polarized light (Figure 2.8b,e) it is possible to study the magnetization of the system. The absorption peak of oxidized Fe is shifted from the one of metallic Fe and can be easily distinguished (yellow band); in this peak, a dramatical change of XMCD response is observed between upward and downward polarization states(Figure 2.8b,e).

The disappearance of XMCD signal for downward polarization is explained by the transition of FeOx from ferromagnetic to antiferromagnetic. This hypothesis is supported also by *ab initio* calculations that predict a reduction, and possibly a change of sign, of the exchange constant in the interface layer.

2.3.2 Ferroelectric Control of Magnetic Anisotropy

In magnetic materials, rotational invariance is always broken by *anisotropy* effects, which make magnetization along particular space directions particularly favourable. Many effects concur to anisotropy such as crystalline structure, strain, shape and interface proximity [49].

Ferroelectric control of magnetic anisotropy in CoFeB/BaTiO$_3$ heterostructure will be shown in chapter 4, however, due to the disorder of CoFeB alloy, no theoretical predictions were made for this interface. Results for the well known Fe/BaTiO$_3$ interface will be exposed here instead.

Ab initio calculations performed on Fe/BaTiO$_3$ by Duan *et al.* show in fact that magnetic anisotropy energy (MAE) can be controlled through ME coupling with a ferroelectric [69]. The supercell structure investigated by the authors is composed of 3 BaTiO$_3$ unit cells with TiO$_2$ termination and 1 monolayer of Fe, and is depicted in Figure 2.9a. MAE is calculated within the force theorem as the difference of single particle energies corresponding to magnetization along the [100] and [001] directions, as MAE $= E^{[100]} - E^{[001]}$. The results of calculations

are shown in Figure 2.9b, denoting a variation of anisotropy energy as large as 46% between up and down polarization of $BaTiO_3$. Similar results were later confirmed by other calculations for thicker layer of Fe [70].

The positive value of MAE indicates a magnetic easy axis normal to the surface; the resulting out-of-plane magnetization arises from interface effects [71] and can be observed in ultrathin ferromagnetic films. This interface anistropy, often indicated as Perpendicular Magnetic Anisotropy (PMA), is particularly interesting for applications, since perpendicular magnetization may allow higher storage densities in memory devices [72]. Moreover, the potential coupling of PMA and ferroelectric polarization open new perspectives: electric field assisted magnetic recording can be obtained by decreasing the required magnetic field to reverse the magnetization [73] or, even better, an electrically controlled transition between in-plane and out-of-plane magnetization can be achieved by proper engineering of ME coupling and magnetic anisotropy [74].

This fully justifies the interest in the $CoFeB/BaTiO_3$ system; CoFeB is one of the most used materials in the framework of PMA [75–79] and electric control
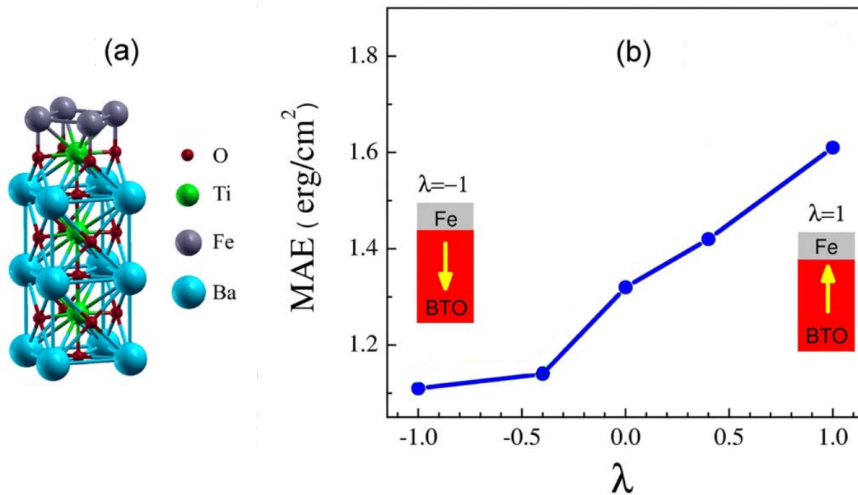
Figure 2.9: **a)**Unit cell of a monolayer-thick Fe film on $BaTiO_3$. **b)** calculated MAE as a function of polarization scaling factor λ. $\lambda = -1$ and $\lambda = 1$ correspond to polarization pointing down and up respectively (adapted from [69]).

of its magnetic properties is a significant result.

Chapter 3

Experimental Methods

This chapter will introduce the relevant methods and technologies that have been employed during this work.

The thin film growth equipments used in sample fabrication are described in section 3.1.

Afterwards, the optical lithography process required for device patterning is presented in section 3.2

At last, the principal characterization methods that have been used throughout the thesis (Ferroelectric, magneto-optical and magnetotransport measurements) are presented in section 3.3.

3.1 Sample Preparation Techniques

In this work, two different kind of devices are presented. The first, multiferroic capacitors based on the $Ta/CoFeB/BaTiO_3/La_{0.67}Sr_{0.33}MnO_3$ template, are grown by pulsed laser deposition (PLD) and sputtering, while the second, multiferroic tunnelling junctions realized on $Au/Co/Fe/BaTiO_3/La_{0.67}Sr_{0.33}MnO_3$ multilayers, are grown by PLD and molecular beam epitaxy (MBE).

Multiferroic tunnelling junctions and part of the multiferroic capacitors have

been realized in the multichamber system LASSE (Layered Artificial Structures for Spin Electronics), a cluster tool that allows combined growth by PLD and MBE in vacuum conditions. The system offers as well several *in situ* characterization techniques such as Reflection High-Energy Electron Diffracition (RHEED), Low Energy Electron Diffraction (LEED), X-ray and Ultraviolet Photoemission Spectroscopy (XPS,UPS), Spin resolved Inverse Photoemission (SPIPE) and Magneto-optical Kerr effect (MOKE) [80]. A schematic view of the complete system is sketched in Figure 3.1. The Introduction Chamber (IC) serves as fast entry lock and as connection between Pulsed Laser Deposition Chamber (PLDC) and the Sample Preparation Chamber (SPC). The Pulsed Lased Deposition Chamber (PLDC) is devoted to the growth by PLD; *in situ* high-pressure Reflection High-Energy Electron Diffracition (RHEED) is disposable to monitor the growth
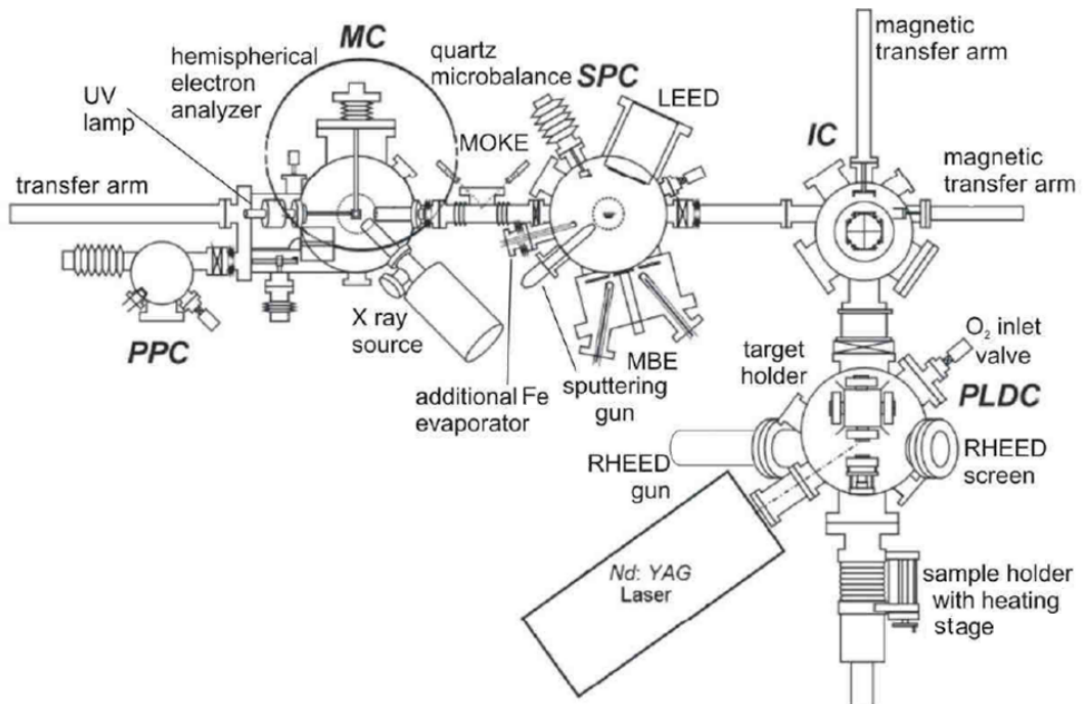
Figure 3.1: Schematic diagram of the LASSE cluster (top view). High and ultrahigh vacuum chambers are interconnected by gauge valves and samples can be moved from one chamber to the others by means of magnetic and mechanical transfer arms. (from [80])

process in real time. Sample Preparation Chamber (SPC) allows: *i*) sample and substrate cleaning by ion sputtering and thermal annealing, *ii*) growth by MBE, *iii*) surface quality characterization through Low Energy Electron Diffraction (LEED). At last, Measurement Chamber (MC) is dedicated to electron spectroscopies. PLDC and IC have a base pressure of about 10^{-8} mbar, SPC and MC chambers, instead, are maintained in Ultra High Vacuum (UHV) conditions, i. e. at a pressure lower than 10^{-9} mbar; this is necessary to avoid sample contamination and to grant a sufficient mean free path for particles during MBE deposition and spectroscopy experiments.

The four chambers are interconnected by gate valves and the different steps involved in the sample growth may be conducted without breaking the vacuum, as sample can be moved from one chamber to another by means of magnetic and mechanical transfer arms.

3.1.1 Pulsed Laser Deposition

Pulsed Laser Deposition is a well established technology for thin film preparation. In particular, this technique offers the possibility to obtain the correct stoichiometry also in very complex compounds such as ferroelectric (e.g. $BaTiO_3$), ferromagnetic (e.g. $La_{0.67}Sr_{0.33}MnO_3$) or high temperature superconducting oxides. These functional oxides, in fact, are typically ternary or quaternary compounds and their manifold structure is difficult to obtain with other deposition methods such as sputtering or co-evaporation of the single constituents.

The principle of PLD is shown in Figure 3.2. An high-energy pulsed laser beam is focused on the surface of a target with the stoichiometry to be transferred to the sample. The target is instantaneously heated up to 2000-3000K causing vaporization and ionization of the material. The continuous absorption of energy from the laser pulse increases rapidly temperature and pressure inside the plasma, that quickly expands perpendicularly to the target, forming the characteristic

plume (inset of Figure 3.2). The plume is highly directional and the chemical species move inside the plasma towards the substrate where they impinge and condensate.

The system in LASSE employs a quadrupled Nd:YAG laser source ($\lambda = 266$ nm) operating in Q-switched regime. Intensity, fluence, focalization and repetition rate can be independently tuned. Up to four stoichiometric targets can be lodged inside the chamber and selected at any time thanks to a rotating holder.

Even if targets have the correct stoichiometry, oxide films have a tendency to deoxygenate during growth. To compensate for this effect, a continuous flow of 0.2 SCCM of high purity ($> 99.9999\%$) oxygen, controlled through a flowmeter, is introduced in the chamber during deposition. Pressure of the oxygen gas is regulated manually by acting on a leak valve between the chamber and a turbomolecular pump.

Perovskite films, like $La_{0.67}Sr_{0.33}MnO_3$ and $BaTiO_3$, are usually grown at high temperature (800 K - 1200 K) in order to increase the mobility of atoms on the
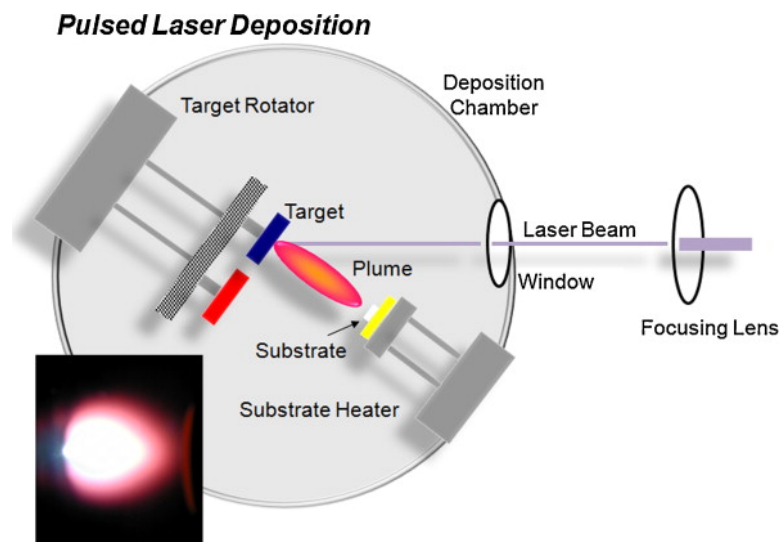
Figure 3.2: Schematic of a pulsed laser deposition system. The inset picture show an actual photograph of the plasma plume (from [81]).

	$La_{0.67}Sr_{0.33}MnO_3$	$BaTiO_3$
Oxygen pressure	$2.9 \cdot 10^{-1}$ mbar	$2.7 \cdot 10^{-2}$ mbar
Substrate Temperature	730℃	640℃
Beam Energy	40 mJ	9 mJ
Repetition Rate	2 Hz	2 Hz
Sample distance	37.5 mm	27.5 mm

Table 3.1: Parameters for growth of $BaTiO_3$ and $La_{0.67}Sr_{0.33}MnO_3$ by Pulsed Laser Deposition

surface and promote the rearrangement towards a stable crystalline order (at least in case of good lattice matching between film and substrate). For this reason, the substrate can be heated by a 400W infrared lamp lodged in an Al coated reflector. Temperature is regulated manually and controlled by means of an optical pyrometer.

During the growth process, targets are rotated and translated vertically in order to uniform the erosion of the material. Also the substrate is held in rotation to obtain uniform film growth. All the movements are realized by stepper motors remotely controlled with a PC.

PLD has been employed in this work to deposit ferroelectric insulator $BaTiO_3$ and ferromagnetic half-metal $La_{0.67}Sr_{0.33}MnO_3$ perovskite oxides on commercial 0.5 mm thick $SrTiO_3$ substrates. $BaTiO_3$ growth conditions had already been optimized in previous works of NaBiS group [82], while parameters for $La_{0.67}Sr_{0.33}MnO_3$ have been re-optimized during this thesis period to achieve atomically flat surfaces. The optimized growth parameters employed for these two materials are summarized in Table 3.1.

Growth rates for $La_{0.67}Sr_{0.33}MnO_3$ and $BaTiO_3$, at the conditions reported in table 3.1, have been measured from the RHEED oscillation period (Figure 3.3) and by X-Ray Reflectometry (XRR) on test samples, resulting 1.82 ± 0.2 nm/min and 1.85 ± 0.2 nm/min respectively. XRR measurements have been performed by Greta Radaelli at Thales Research - Universitè de Paris-Sud.
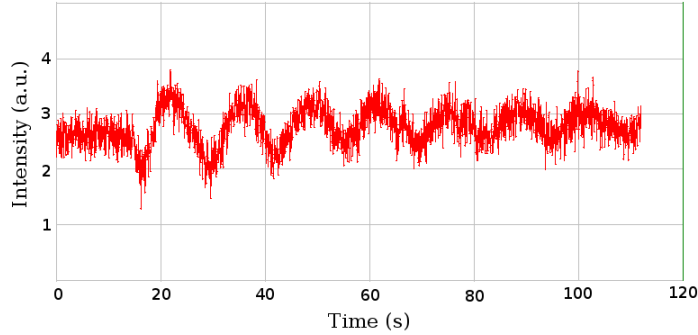
Figure 3.3: RHEED oscilation monitored during BaTiO$_3$ growth, each period is related to the completion of a unit cell layer (4.04 Å). The resulting growth rate is then 1.85 nm/min.

Upgrade of the PLD setup

As part of my thesis work, an upgrade of the PLD system has been developed in order to achieve uniformity of thin films over areas up to 1 sq inch.

Uniformity in PLD growth is limited by the extension and shape of the plasma plume: in our case, this corresponds to a uniformity radius of about 2.5 mm. To cover uniformly a radius larger than few millimetres, a relative motion of the plasma plume with respect to the substrate is commonly employed in large area deposition processes [83]. Since the sample holder in our system is not allowed to translate, a system was designed to scan the position of laser spot on the surface of the target, in order to achieve this relative motion. This method, upon proper optimization of the rastering algorithm, could allow uniformity over a area that is limited only by the target dimension, as the laser spot can be moved all over the target diameter (1 inch).

In the realized system, sketched in Figure 3.4, the laser beam is directed by means of two high reflectivity dielectric mirrors (R > 99.5% at λ=266 nm) of which one mounted on a motorized stage. The translation axis of the stage is chosen parallel to the target surface and the focusing lens is rigidly coupled with the moving mirror, in this way the beam focusing on the sample is maintained independently from the translation. To coordinate the movement of the mirror with

target and sample rotations, the proprietary software previously used to control the stepper motors of PLDC has been rewritten in the LabVIEW environment to include also the motorized stage.

The system has been successfully tested with a laser diode and will be soon introduced in the LASSE setup.
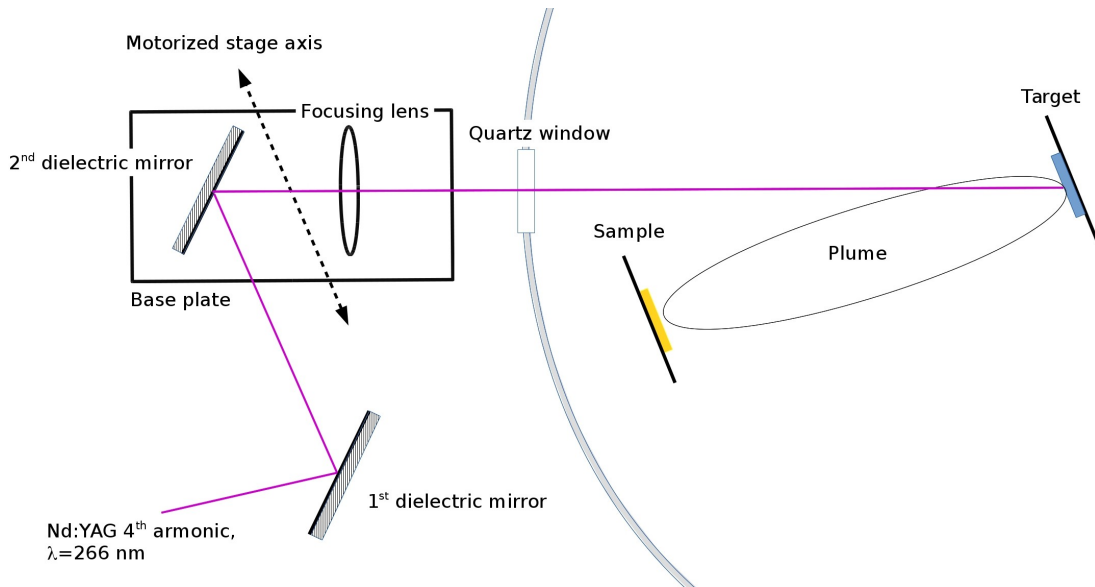
Figure 3.4: Sketch of the mechanical system for large area PLD (dimensions are not to scale).

3.1.2   Molecular Beam Epitaxy

Molecular Beam Epitaxy allows deposition of high quality epitaxial films in a UHV regime. Heating of a target source in a effusion cell causes thermal evaporation of atoms which travels freely in the UHV ($p < 10^{-9}$ mbar) environment until they impinge on the sample surface. Atomic level control is achieved via shuttering and resulting layers presents abrupt interfaces. Growth in UHV ensures low impurity incorporation even though deposition rates are rather low (few Å/min).

Deposition of Fe, Co and Au layers in multiferroic tunnelling junctions has

been obtained by MBE in the Sample Preparation Chamber. SPC is equipped with six confocal evaporator cells and an additional cell that can be moved near to the sample to achieve larger growth rate. Thermal evaporation is achieved by electron bombardment of high purity metal rods, as in the case of Fe and Co, or beads contained in Mo crucibles, as in the case of Au. Deposition rates are calibrated before each growth process with a quartz microbalance mounted in the SPC chamber.

3.1.3   Sputtering

Sputtering is a physical vapor deposition technique which allows a good film adhesion to the substrate and a high control on the thickness, uniformity and composition of the deposited material.

In a sputtering process, atoms of an inert gas (frequently Ar) are introduced into the high vacuum chamber and a negative bias voltage is applied to the target of material to deposit. Every free electron and Ar^+ ions is immediately accelerated by the electron field in proximity of the target and ionize by collision the Ar atoms leaving Ar^+ ions and e^- free electrons. The newly ionized Ar^+ ions and electrons, accelerated by the target potential, ionize other Ar atoms in a cascade process which ignites the plasma. At this point, positively charged Ar^+ ions are accelerated towards the negatively biased target material, which is eroded by ions via momentum transfer. This causes an ejection of the source material in the form of neutral atoms, clusters of atoms or molecules. As these neutral particles are ejected, they will mainly travel in a straight direction until they impinge on the sample and get incorporated in the growing thin film.

In this work, an AJA ATC Orion sputtering system has been used to grow the films of Ta and $Co_{0.4}Fe_{0.4}B_{0.2}$ on ferroelectric $BaTiO_3$ capacitors previously grown by PLD, as well as to deposit SiO_2 during the lithography of both capacitors and MFTJs. The specific system is provided with 10 confocal sputtering guns with

individual pneumatic shutters that ensure a control of the deposited film with a precision up to about 1 Å. Deposition rates have been measured with a quartz microbalance mounted in the vacuum chamber and by atomic force microscope profilometry.

3.1.4 Comparison of Growth Technologies

Each of the growth methods employed in this work (pulsed laser deposition, molecular beam epitaxy and sputtering) has its strengths and weaknesses. The choice of one technique over the others depends on the specific material to grow and the required characteristics of the deposited film.

Pulsed laser deposition allows growth of thin films with high control of stoichiometry and crystallinity also of complex compounds like functional oxides. Nevertheless, the already discussed problem of uniformity limits this technique to deposition on small substrates or wafers.

Molecular beam epitaxy is a very simple technique that allows epitaxial growth of thin films, high control of deposited thickness and abrupt interfaces. This high quality growth finds a drawback in the very low growth rates of MBE processes (not exceeding few Å/min). Moreover, MBE requires an ultra high vacuum setup, differently from the other two techniques here considered.

Sputtering deposition offers high growth rates and high surface uniformity over large areas (2 sq inch in our system), while preserving good chemical quality of the deposited compound. This comes at expenses of crystalline quality, as polycrystalline films are grown.

In conclusion, PLD and MBE are techniques for high quality film deposition. PLD is ideal to grow perovskite oxides like $BaTiO_3$ and $La_{0.67}Sr_{0.33}MnO_3$, while MBE allows epitaxial deposition of simple compounds like elemental 3d metals. Sputtering is the most efficient of the techniques here considered as long as epitaxy of the film is not required, as in the case of amorphous alloy CoFeB.

3.2   Optical Lithography

Ultraviolet Optical Lithography is a widespread technique for micro-fabrication of electronic devices. This technique employs an ultraviolet radiation source to transfer a pattern from a properly designed chromium mask to a radiation sensitive polymer (*photoresist*) deposited on sample surface. After exposition and a proper developing process, selected areas of sample remain covered with photoresist allowing for successive steps of deposition or etching.

The steps of lithographic process are illustrated in Figure 3.5 and are described in the following.

1. **Sample cleaning**. Superficial contaminations have a bad influence on the resist adhesion and on the quality of the transferred image. The cleaning of the sample consists in general in an ultrasonic bath in acetone or a soft bake in order to desorb water.

2. **Primer deposition**. A better adhesion of the resist is achieved on hydrophobic surfaces, because the polymer is a non-polar substance and the formation of polar bounds O-H prevent the resist from wetting the substrate. A promoter of the adhesion (primer, in our case TI-PRIME from MicroChemicals GmbH) makes the surfaces hydrophobic. The deposition
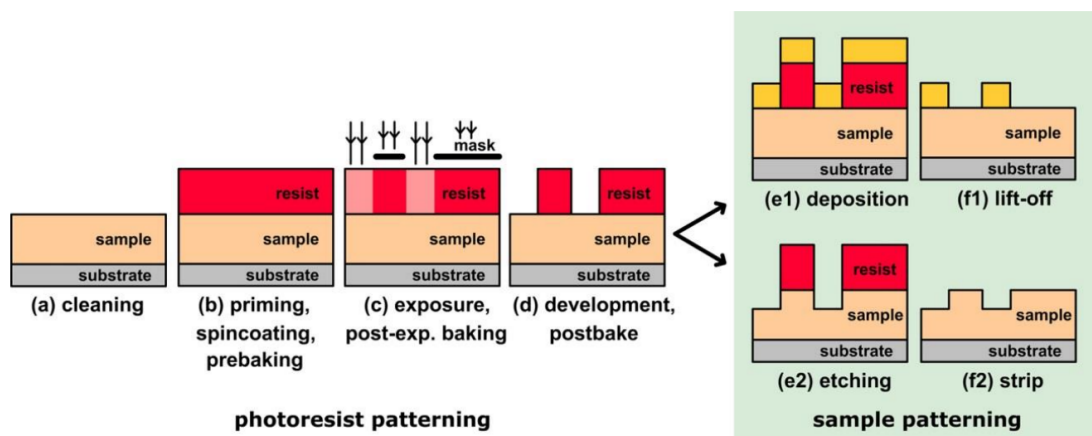
Figure 3.5: Schematic of an optical lithography process with positive resist.

of primer is achieved by spin-coating (see below) and is followed by a soft bake at 120 °C for 2 minutes in order to evaporate the solvent.

3. **Photoresist deposition**. The image reversal photoresist AZ5214E from MicroChemicals GmbH has been used for device lithography. It consists of a photoactive compound (naphthoquinone diazide) in a Novolak resin matrix.

The deposition from solution of phototoresist films 1.4 μm thick occurs via spin-coating. The sample is covered with some drops of liquid and put on rapid rotation so that the centrifugal force distributes the material uniformly on the sample surface. Thickness t of the resulting film depends on angular velocity ω and fluid viscosity η accordingly to the empirical relation

$$t = K \frac{C^{\alpha} \eta^{\beta}}{\omega^{\delta}}$$

where K, α, β, δ are specific constants of the system.

The spin coating method provides a high processing speed and a high homogeneity of the layer thickness for films up to a few microns. However, if the sample has no rotational symmetry, the spun material becomes thicker at the corners. In the case of photoresist deposition, this could lead to problems during development.

After the photoresist deposition, the solvent is evaporated by a soft bake at 110 °C for 50 seconds.

4. **Exposure**. The exposure to light radiation, over a certain dose, modifies the chemical properties of the photoresist, producing a different solubility of the exposed and unexposed part of the film. In the case of the positive resist AZ 5214E, the exposed regions become more soluble and can thus be easily removed in the development process. UV radiation has been used and the image transfer is realized through a mask patterned with Cr: where

the metals is present on the mask, it adsorbs the radiation protecting the underlying resist from the exposure. In this way it's possible to transfer the Cr pattern into a resist pattern on the sample.

To align the mask to the sample in the various lithographic steps a Karl Suss MA56 mask aligner has been used; the UV source is the Hg-I line (365 nm) of a mercury lamp with a power density of about 10 mW/cm^2.

5. **Development**. During the developing process, an appropriate solvent (AZ100 DEV from MicroChemicals GmbH) removes the part of resist not belonging to the image. In case of positive resist, the exposed part is dissolved, while the part protected from the light by the Cr mask remains onto the sample. For a negative resist (not used in this work) the mechanism is just the opposite.

6. **Addictive or subtractive processes**. As the sample is patterned, selective etching and/or material deposition can be performed. In the case of etching (done with the technique of ion beam etching described in section 3.2.1), resist protects the covered areas from being removed, whereas, in the case of deposition, it prevents the adhesion of material on the underlying layer.

7. **Strip or Lift-off**. After ion beam etching, strip of the resist gives a pattern with some parts in relief, corresponding to the metallic zone of the mask. In the case of deposition, the lift-off of the resist removes also the overlying material: the pattern consists in deposited material in correspondence of the exposed part of the sample surface. In both cases samples were kept in AZ100 Remover from MicroChemicals GmbH in order to remove the remaining resist. To check the completion of the process, samples were carefully examined with an optical microscope.

3.2.1   Ion Beam Etching

Ion Beam Etching is a physical dry etching technique where Ar^+ ions are accelerated towards the sample in a vacuum chamber ($p \simeq 10^{-7}$ Torr). Similarly to what happens with sputtering targets, the sample material is removed by momentum transfer between the accelerated Ar ions and the sample surface.

During the etching process, the sample holder is kept in rotation to ensure the uniformity of the etching on the whole surface. Furthermore, it is possible to tilt the sample holder with respect to the incident beam by a desired angle (tipically 30°or 60°) to avoid redeposition of material during the etching.

The etching rate depends on many factors, including the composition of the etched material. When dealing with critical lithographic processes such as the junction definition in MFTJs, we employed a visual method to determine when to stop the etching. *Flags*, i. e. exact replicas of the to-be etched part of the sample grown on a transparent substrate, are mounted together with the samples on the holder, so that they are etched in the same exact way. As shown in Figure 3.6, when the flags become transparent, it means that all the flag material and the correspondent part of the sample have been removed, thus the etching can be stopped.
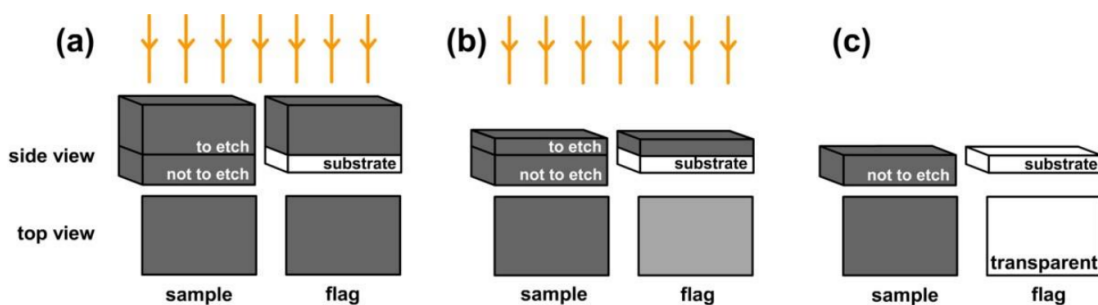
Figure 3.6: Visual method based on *flags*. **a)** At process beginning sample and flag have a similar surface colour. **b)** Appoaching the desired etching depth the flag clears up. **c)** When the flag becomes transparent the desired depth has been reached and the process is stopped.

3.3 Measurement and Characterization Techniques

3.3.1 Ferroelectric Properties Characterization

The measure of the polarization-voltage curve (becoming an hysteresis cycle in ferroelectric materials) is fundamental for the determination of ferroelectric properties like the coercive field and the remanent polarization. Traditionally, a capacitance bridge as first described by Sawyer and Tower in year 1930 [84] has been used for this purpose.

The Sawyer-Tower circuit is sketched in Figure 3.7. As the sample is in series with a reference capacitor, the charge is the same on both elements. The measurement of the voltage drop on the capacitor gives an estimation of the charge on the ferroelectric sample. The signal generator applies a sinusoidal voltage to the capacitance bridge, which is also sent to the oscilloscope. The oscilloscope measures this voltage as the x-signal and voltage drop on reference capacitor as the y signal, in order to display on screen the ferroelectric hysteresis loop.

Nevertheless, this method is not suitable in thin-film characterization for var-
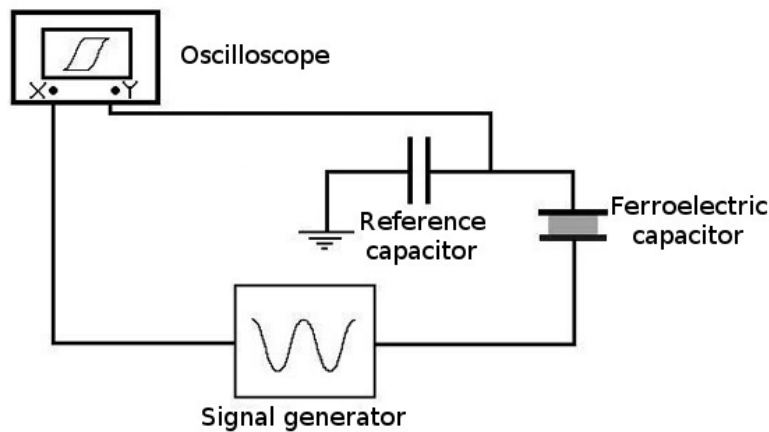
Figure 3.7: Sawyer-Tower circuit composed of a signal generator operating on the series of the sample and a reference capacitance. An oscilloscope measures the voltage drop on the capacitor.

ious reasons; for example, the need to compensate for dielectric loss and the fact that the film is being continuously cycled.

An alternative approach, that will be employed in this work, is to infer the ferroelectric properties directly from the current-voltage characteristics of planar ferroelectric capacitors. In fact, the I-V curve of an ideal ferroelectric capacitor presents an abrupt current peak in correspondence its coercive field (Figure 3.8c) related to the displacement of ions, which allows to disclose the extrinsic ferroelectric effect.

In the measurements, a voltage sweep of amplitude V_{max} and frequency ν_0 is applied to the sample and the current response signal is measured. Polarization P is then calculated as the ratio between charge (obtained integrating the current through time) and area A [85].

$$P = \frac{\int I(t)dt}{A} - C_1 = \frac{1}{4AV_{max}\nu_0} \oint |I(V)|dV - C_2 \qquad (3.1)$$

where C_1 and C_2 are integration constants that can be obtained from the boundary condition $P(V_{max}) = -P(-V_{max})$.

Ferroelectric characterization of thin films is particularly problematic, mainly because of spurious contributions to the hysteresis cycle. Due to the reduced thickness, conductive pinholes caused by defects can easily cross the film favoring leakage currents. Moreover, also dielectric charging current has to be taken in
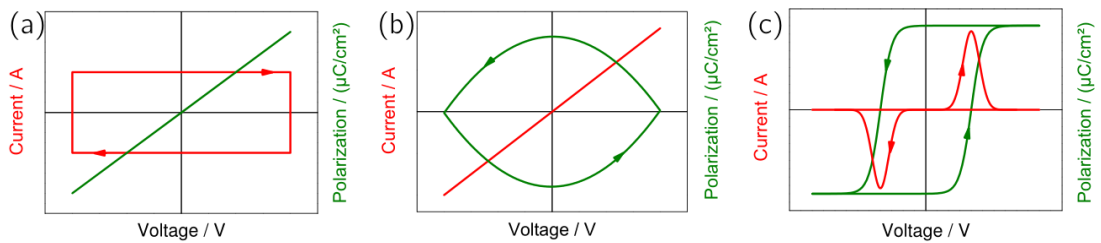
Figure 3.8: Ideal current-voltage characteristics and relative polarization-voltage curves of different circuital elements: **a)** Capacitor. **b)** Ohmic resistor. **c)** Ferroelectric (from [85]).

account, and its contribution increases with the inverse of thickness.

The effect of these parallel channels on the measured current and its consequence on polarization-voltage curves is sketched in Figure 3.8. In particular, the contribution of leakage to the hysteresis loops may be considerable, leading to fictitious values of relevant ferroelectric parameters, such as the remanent polarization and the coercive field, and even to the incorrect determination of the ferroelectric character [86].

In the present work, ferroelectric characterization has been performed using a TF Analyzer2000 (AixACCT System GmbH), which allows to measure I-V curves for applied voltages up to 25 V and frequencies between 10 mHz and 5 kHz.

I-V loops have been recorded with the method called Dynamic Hysteresis Measurement (DHM). Four bipolar triangular excitation signals of frequency ν_0 are applied with a delay time τ between them (Figure 3.9). The final I-V loop is obtained from the combination of the currents measured while applying the negative voltage during the second pulse and the positive voltage during the fourth pulse (negative and positive voltages, respectively). The first and the third pulses are necessary in order to obtain the same measurement conditions while recording the positive and the negative part of the final loop.

The I-V curves obtained by DHM can be corrected for leakage effects using the Dielectric Leakage Current Compensation (DLCC) method. This method
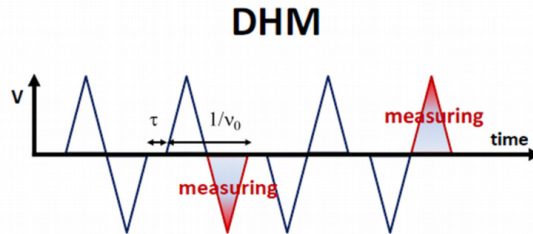
Figure 3.9: Voltage train pulses that are applied in dynamic hysteresis measurements, shaded areas correspond to the pulses at which the current measurement is performed. ν_0 is the measurements frequency and τ the delay time between pulses (from [87]).

is based on two assumptions: *i)*the leakage current is independent of frequency and *ii*) the dielectric current and the current due to the ferroelectric switching are both linearly depending on frequency. Under these hypotheses, measuring the DHM cycles at two frequencies (ν_0 and $\nu_0/2$) allows subtraction of leakage current, thus leaving only the displacement current.

A different method could be used to obtain reliable values of remanent polarization in case DLCC were not effective in removing leakage contribution, being either or both the hypothesis unsatisfied, or, in any case, to exclude also dielectric contribution. The Positive-Up-Negative-Down (PUND) technique employs a train of five voltage pulses applied to the sample (Figure 3.10). The first is a negative prepolarization pulse that leaves the sample in a negative polarization state. The second and the third pulses are positive: the second (P, for "positive") polarizes the sample and therefore the corresponding current contains the ferroelectric and non-ferroelectric contributions, while current during the third (U, for "up") pulse only contains the non-ferroelectric contributions; therefore, their subtraction allows to obtain, in principle, only the ferroelectric contribution. The same applies, for the negative state, to the fourth (N, for "negative") and the fifth pulse (D, for "down"), so that the current loop $I_{PUND} - V$ is obtained from $I_P - I_U$ for positive voltages and from $I_N - I_D$ for negative voltages. Consequently, PUND current only contains the switchable ferroelectric contribution,
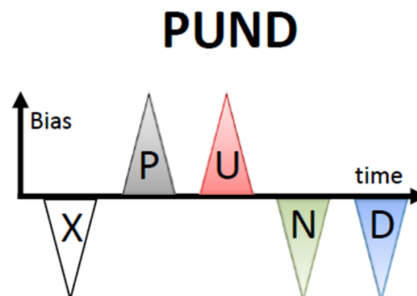
Figure 3.10: Voltage train pulses applied during PUND (Positive-Up-Negative-Down) measurements (from [87]).

while all the other contributions are excluded.

3.3.2   Magneto-Optic Kerr Effect

MOKE technique provides a powerful way for studying the magnetic properties of thin films by analysing the light reflected from their surface. A linearly polarized electromagnetic wave can be decomposed in one right-handed (RCP) and one left-handed (LCP) circularly polarized components of equal amplitude. A magnetized material reflects the two components in a different way, introducing a difference between their amplitudes (Kerr ellipticity) and phases (Kerr rotation) proportional to the magnetization. The Kerr rotation is associated to the different phase delay undergone by RCP and LCP components (birefringence), while the Kerr ellipticity to the different absorption of RCP and LCP light (dichroism).

In the basic configuration for MOKE measurements, the incident light, which is usually generated by a laser diode, is linearly polarized by a polarizer, before reaching the sample; the reflected light passes through through a second polarizer (the analyzer) and reaches a photodiode.

As depicted in Figure 3.11, different components of sample magnetization vector can be measured, depending on the relative direction of the magnetization to the plane of incidence. Whether the magnetization is parallel to the surface normal, parallel to the surface and in the plane of incidence, or parallel to the surface and perpendicular to the plane of incidence, it is called the polar Kerr
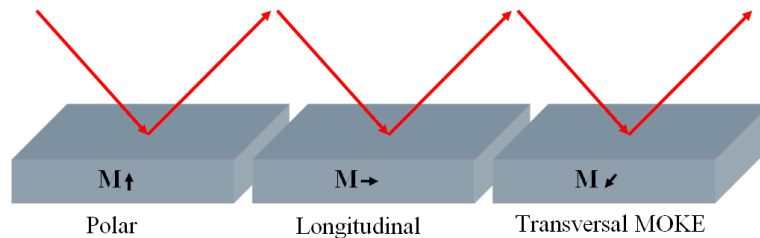
Figure 3.11: Schematic configurations of the sample magnetization for the polar, longitudinal, and transverse magneto-optical Kerr effects.

effect, the longitudinal Kerr effect, and the transversal Kerr effect, respectively.

The MOKE measurements performed during this thesis work were typically affected by a small signal-to-noise ratio, essentially due to the reduced thickness of the ferromagnetic material, leading to weak magneto-optical signals (rotation and ellipticity). A modulation-demodulation technique was therefore employed. The standard measurement scheme is the MOKE configuration as described in [88] and reported in figure 3.12.

A laser diode generates a collimated light beam that is linearly polarized by a polarizer (P1 at 0° or 90° with respect to the optical plane) before it is reflected from the sample. After the reflection, it crosses a Photoelastic Modulator (PEM) oscillating at a frequency $f = 50$ kHz that introduces a controlled phase delay between the electric field components parallel and perpendicular to the plane of incidence. After the PEM, a second polarizer (P2 at 45°) is placed as analyzer before the beam reaches the photodiode.

The phase modulation introduced by PEM, besides allowing a modulation-demodulation technique, disentangles the rotation and ellipticity variations after the reflection [88]. The demodulation either at the frequency of the PEM (f) or its double ($2f$) gives information about the Kerr ellipticity or rotation, respectively.

It is worth noting that a MOKE measurement does not provide quantitative information about the magnetization vector, but gives an accurate picture of the magnetization curve. Quantitative values of magnetic moment can be obtained
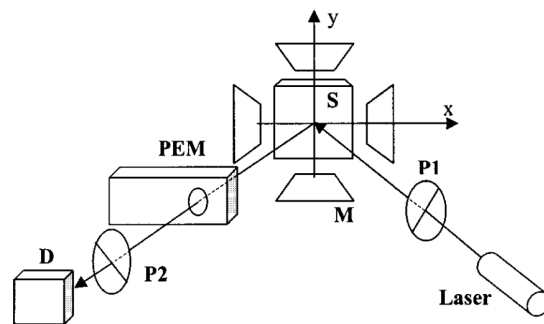
Figure 3.12: Scheme of the MOKE apparatus (from [88])

instead with other techniques such as Vibrating Sample Magnetometry (VSM) which, however, can be employed only on non patterned films, and is thus non suited for characterizing our devices.

Finally, although MOKE is a surface-sensitive method, the probing depth is on the order of 10–20 nm, then, if the films are thin enough, one can also obtain information about the magnetization of the underlying layers.

MicroMOKE setup

MOKE characterization of microcapacitors that will be presented in Chapter 4 requires a probing laser spot whose diameter could not exceed 70 μm (i. e. the smaller side of the rectangular capacitor surface), in order to collect the signal just from the device that is electrically controlled. For this reason the microMOKE setup sketched in Figure 3.13 has been used in all the measurements.

In addition to the standard setup, the polarized light passes through a beam splitter to a 10× objective lens in order to focalize the beam in a small spot. The diameter of the laser beam has been found to be around 60 μm at its smallest
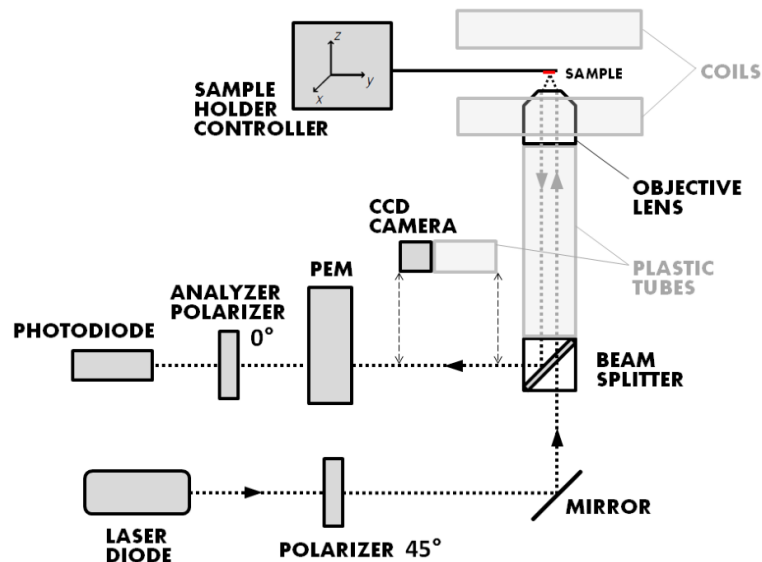
Figure 3.13: Scheme of the MicroMOKE setup.

size, i.e. when located close to the focal point of the objective lens (f= 4 mm). A CCD camera can conveniently placed on the reflected light path to get a magnified view of the sample and of the laser spot on it. The sample holder allows for the micrometric control of the position of the sample on the three axes. Referring to the coordinate system sketched in Figure 3.13, the x-y movement allows to accurately probe different zones of the sample, while the z movement allows to finely adjust the position of the sample close to the focal point of the objective lens, in order to work with the smallest diameter of the laser spot on the sample.

3.3.3   Transport Measurement

Electrical measurements in this work were used to study the I-V characteristic and magnetoresistive behavior of multiferroic tunneling junctions. In both cases, two-point or four-point probe measures have bee performed. In the former case, referring to the experimental setup in Figure 3.14a, each contact serves as a current and as a voltage probe. The intention is to determine the resistance R_{DUT} of the device under test (DUT). The total resistance is given by:

$$R_T = \frac{V}{I} = 2R_W + 2R_C + R_{DUT} \tag{3.2}$$

where R_W is the resistance of the wire used for the connections, R_C is the contact resistance and R_{DUT} is the device resistance. Unless the condition $R_{DUT} \gg$
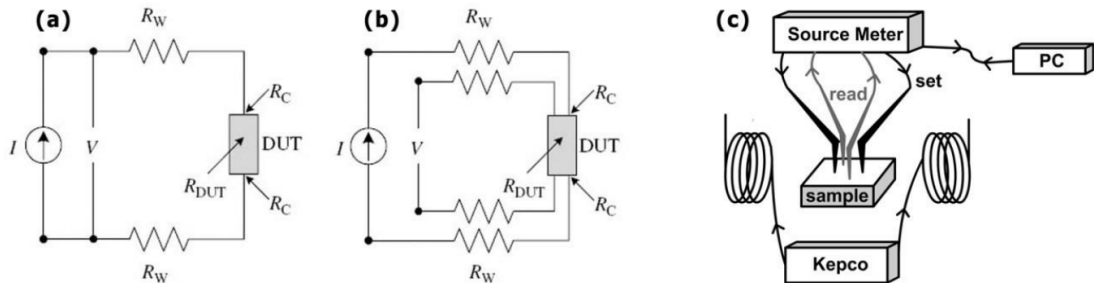
Figure 3.14: **a)** Two-points probe and **b)** Four-point probe resistance measurement arrangements. **c)** Sketch of a four-point system for TMR measurements.

$R_W + R_C$ holds true, it is impossible to measure R_{DUT} precisely with a two-point probe system.

The problem of parasitic resistances can be solved by using a four-point probe setup, whose circuital scheme is shown in Figure 3.14b. The current path is the same, but the voltage drop across R_{DUT} is measured by a voltmeter on a parallel circuit. Even though also this circuit is affected by wire and contact parasitic resistances, if the voltmeter input impedance is high enough (which is tipically true, since $R_{IN} \gtrsim 10^{12}$ Ω), the current flowing in this branch would be negligible and consequently also the voltage drop across the resistances. As a result, the actual measured resistance will be R_{DUT}.

Figure 3.14c shows the scheme of a four-point system for TMR measurements. The sample is located in the between the magnetic poles of an electromagnet. The current flowing in the coils comes from a KEPCO bipolar generator controlled remotely by a PC. A fixed junction voltage is set and the junction current is sensed for different values of applied magnetic field. The data are sent in real-time to a LabVIEW software for analysis.

Chapter 4

Magnetoelectric coupling at the CoFeB/BaTiO$_3$ interface

This chapter presents the part of this work devoted to growth and characterization of ferroelectric capacitors with magnetic electrodes. The optimization of the growth process and the first demonstration of electric control of magnetic anisotropy in Ta/CoFeB/BaTiO$_3$/La$_{0.67}$Sr$_{0.33}$MnO$_3$ structures have been previously performed by the NaBiS group, as reported in detail in reference [46]. Starting from this result, in this chapter we prove the presence of a stable magnetoelectric coupling between BaTiO$_3$ and CoFeB. The interaction is present also in absence of an external applied electric field and is associated to the non-volatile ferroelectric properties of BaTiO$_3$.

Ferroelectric control of magnetic anisotropy is a valuable technique to achieve a low power writing of magnetic states. A reversible, non-volatile, electrically-driven modification of the magnetic easy axis or, even better, a switch from out-of-plane to in-plane magnetization in a thin film, would determine a dramatical change of resistance in a MTJ-based structure in which this film is an electrode, and the other electrode is a ferromagnetic film with the magnetization pinned in-plane or out-of-plane. The advantages of magnetic reading and electric writing

could be combined, in this way, in a single scalable device.

In the work done prior to the beginning of this thesis, A. Manuzzi observed a variation of anisotropy constant (i. e. a modulation of the coercive field of the FM layer) up to 70% at room temperature in perpendicularly magnetized films [46]. During my activity, further optimization of the structure has been pursued in order to achieve the transition between out-of-plane and in-plane magnetization, but we realized that the criticalities of the process (e.g. the control of the magnetic layer thickness with atomic precision) make this objective absolutely non-trivial.

In this chapter, instead, we focus our attention on the ferroelectric characterization of different samples in order to better understand the entity of the magnetoelectric effect, and we demonstrate the stability of the electrical switching of magnetization in remanence conditions (magnetic states are stable for a time longer than the maximum measurement time of 24 hours).

Section 4.1 describes the growth process and the microfabrication steps employed for realizing the microcapacitors.

Section 4.2 presents ferroelectric characterization of BaTiO₃ on patterned capacitors, aiming at demonstrating existence of a remanent polarization. We demonstrate the existence of a ferroelectric loop of BTO with a ferromagnetic remancence of 3 μC/cm^2.

Section 4.3 shows the ferroelectric control of the perpendicular magnetic anisotropy of the CoFeB layer, with a change of the coercive field between upward and downward polarization of BaTiO₃ of 29% at room temperature.

4.1 Device Design

The ferroelectric/ferromagnetic capacitors were fabricated on Ta(1.2 nm)/CoFeB (t_{CoFeB})/ BTO(150 nm)/LSMO(50 nm) heterostructures. t_{CoFeB} is the CoFeB thickness, either 1.1 nm or 1.3 nm, BTO stands for BaTiO₃, and LSMO stands for La$_{0.67}$Sr$_{0.33}$MnO₃. The heterostructure has been grown on (001)-oriented SrTiO₃

(STO) single crystal substrates. By means of optical lithography, we have defined on each sample many identical Ta/CoFeB/BTO pillars. The structure of a pair of capacitors is represented in figure 4.1.

The layer of LSMO is chosen as bottom electrical contact. Being a perovskite oxide like STO and BTO, with similar lattice parameters, it allows for the growth of epitaxial BTO/LSMO/STO heterostructures [82]. The common bottom electrode allows the application of poling voltage between any pair of capacitors on the same sample (top-top configuration, Figure 4.1b).

CoFeB is used as magnetic top electrode because it is widely demonstrated that CoFeB ultrathin films may exhibit a perpendicular magnetic easy axis, resulting in out-of-plane magnetization [75–79]. The perpendicular magnetic anisotropy (PMA) responsible of out-of-plane magnetization is related to interface effects [71], and it has been theoretically demonstrated [69, 70] that if can be influenced by ferroelectric polarization of an adjacent BTO layer. Possibly, this may lead to a electrically-driven transition from out-of-plane to in-plane magnetization [74], or at least to a modification of the magnetic properties.

On top of CoFeB, a Ta layer is grown to protect the underlying layer from oxidation. Tantalum also promotes CoFeB crystallization and PMA stabilization by absorbing Boron atoms from CoFeB alloy during a post-annealing process in
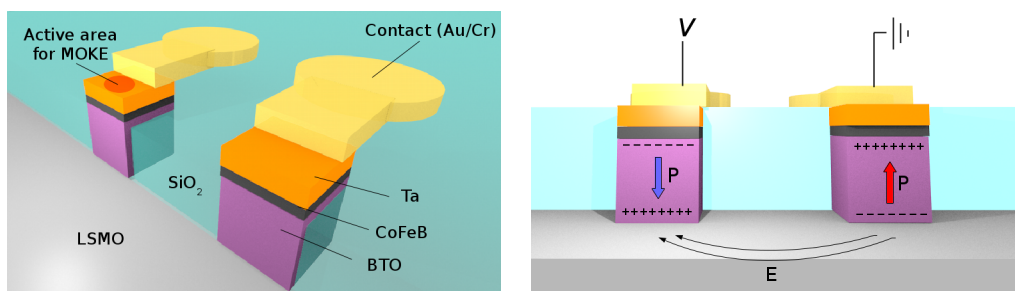
Figure 4.1: **a)** 3D view of a pair of capacitors. **b)** Side view of the structure. The continuous film of LSMO acts as common bottom contact for all the capacitors allowing for top-top measurements, applying a voltage difference to a couple of top contacts and polarizing the corresponding BTO pillars in opposite directions.

applied field [89–91].

During the last lithographic step, a gold contact is evaporated on top of each capacitor in order to allow the application of an electric potential across the BTO layer, thus setting the polarization of BTO in a desired direction. The contact does not cover completely the pillar structure, leaving most of the ferromagnetic layer accessible to magneto-optical probing methods (microMOKE). Insulation between gold contacts and LSMO is ensured by means of a 70 nm thick SiO$_2$ layer added during the lithographic process.

4.1.1   Growth Process

The multilayers required for the realization of capacitors were grown by combined use of pulsed laser deposition (PLD) and sputtering. The thickness of each layer and the process parameters had been previously optimized, as reported in reference [46].

A fundamental parameter in these structures is the thickness of the CoFeB layer. PMA is an interface effect and is dominant over other anisotropic contributions (like magnetocrystalline and shape anisotropy) only for ultrathin layers. In CoFeB, for instance, a transition to in-plane easy axis is expected for $t_{CoFeB} \sim 1.3$ nm (Figure 4.2). Samples fabricated prior to the beginning of this thesis work had t_{CoFeB}=1.1 nm. Although they show ferroelectric modulation of PMA, this is not sufficient to switch magnetization from out-of-plane to in plane. New samples were fabricated during my activity with t_{CoFeB}=1.3 nm in order to ease the transition, according to the steps listed here.

1. SrTiO$_3$ substrate annealing at 1000K for 30' to clean and order the surface.

2. Deposition of 50 nm of LSMO by PLD in the conditions reported in Table 3.1.

3. Deposition of 150 nm of BTO by PLD in the conditions reported in Table

3.1.

4. Annealing at 873K for 30' and cooling for 30' in oxygen atmosphere (0.5 bar) to improve BTO structure and oxygen stoichiometry.

5. Extraction of the sample from the LASSE system (see section 3.1) and insertion in the sputtering deposition system.

6. Soft-etch in Ar plasma (7W power) for 3' to clean the BTO surface after the exposure at the atmosphere.

7. Deposition of 1.3 nm of CoFeB by sputtering

8. Deposition of 1.2 nm of Ta by sputtering

After the growth, the samples were annealed in vacuum at 550 K for 15' to allow crystallization of CoFeB. During the process, a magnetic field of 4 kOe is maintained perpendicular to the sample in order to promote stabilization of PMA.
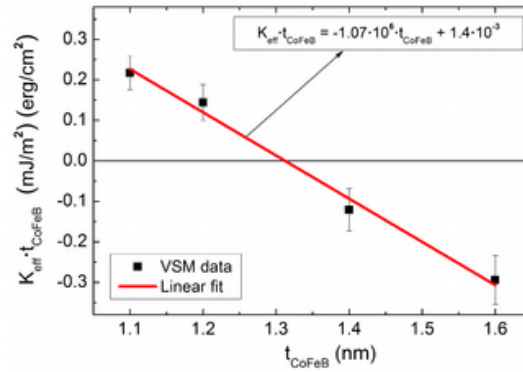
Figure 4.2: Plot of the product of $K_{eff} \cdot t_{CoFeB}$ versus t_{CoFeB}, calculated from the vibrating sample magnetometry (VSM) data, and corresponding linear fit. K_{eff} is the effective anisotropy constant of CoFeB, a positive value of K_{eff} is related to an out-of-plane easy axis, while a negative value is related to an in-plane easy axis (from [46]).

4.1.2   Lithographic Process

Rectangular capacitors with an area of 70×100 μm^2 have been realized with the two-steps lithographic process illustrated in Figure 4.3. Patterning has been done by UV lithography and Ar ions beam etching, as described in section 3.2. At the end of the process, a single substrate (10×10 mm^2) can host up to 26 capacitors each one having a gold contact in order to apply the external voltage.

The whole process is summarized here:

1. Definition of the capacitor structure (Figure 4.3a)

    (a) Deposition of 1.25 μm thick AZ5214E photoresist, exposition to about 125 mJ/cm^2 dose of UV light with mask 1 and development (30 sec in AZ 726 MIF, water as stopper).

    (b) Ion beam etching of the pillar leaving about 100 nm of BTO. The etching time has been calculated by using known etching rates previously calibrated by AFM profilometry on test samples. Note that, an error of few nanometres in the etching depth is not crucial, since the BTO film is 150 nm thick.
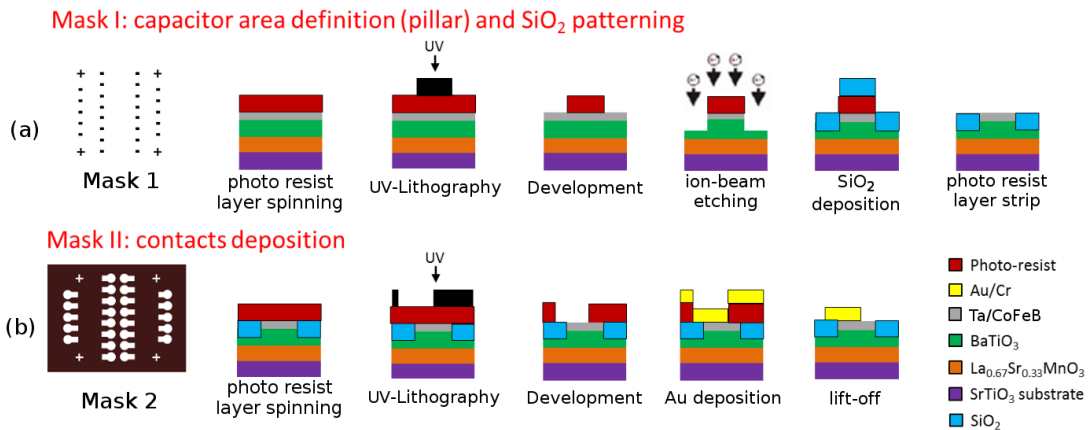
Figure 4.3: Schematic of the lithographic process employed to realize capacitors.

(c) Deposition of 70 nm SiO_2 insulating layer by sputtering to prevent from short circuits between the top and bottom electrodes.

(d) Lift-off in AZ 100 Remover.

2. Lithography of contacts (Figure 4.3b)

(a) Deposition of 1.25 μm thick AZ5214E photoresist, exposition to about 125 mJ/cm^2 dose of UV light with mask 2 and development.

(b) Electronic evaporation of the contacts (7 nm of chromium as adhesive layer, 300 nm of Au).

(c) Lift-off in AZ 100 Remover.

4.2 Ferroelectric Characterization

Dynamic hysteresis and PUND measurements, described in section 3.3.1, have been done on the patterned samples in order to probe ferroelectric properties such as coercive field and remanent polarization. The measurements have been performed in the top-top configuration connecting the capacitors to a TF Analyzer 2000E (AixACCT Systems GmbH) through a mechanical probe station. Ideally, in top-top configuration, the measured dielectric and ferroelectric properties should correspond to a series of two identical capacitors connected through the bottom electrode. This is in principle equivalent to the measurement of a single thin film capacitor with double thickness (300 nm).

Figure 4.4a shows current hysteresis loops taken on a pair of patterned capacitors with the dynamic hysteresis method at different frequencies. The dielectric contribution ($I = CdV/dt$) is dominant over the ferroelectric one, nevertheless, the ferroelectric peaks (see section 3.3.1) are distinguishable in every curve.

The peak position, indicated by black arrows, shifts with the excitation frequency from 2.7 V to 4.5 V between 100 Hz and 3100 Hz. Even though a small
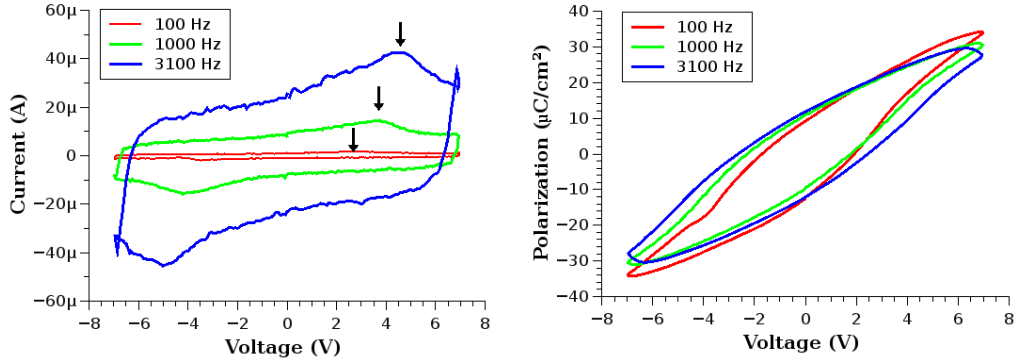
Figure 4.4: **a)** Current-voltage curves for a a pair of capacitors of area 70 × 100 μm^2 at frequency f =100, 1000, 3100 Hz. **b)** Polarization hysteresis cycle obtained integrating the current over time.

contribution from electrical inductance of the setup can be deducted from the rings at extremities of the curve taken at 3100 Hz, this alone can not account for this effect. The behaviour is imputable, instead, to the viscous dynamics of ferroelectric switching and its dependence on frequency [92].

The polarization hysteresis cycles, obtained by integrating the current over time for each fixed voltage, are plotted in Figure 4.4b. The results are summarized in table 4.1. Remanent polarization over 10 μC/cm^2 is measured, while the saturation polarization is about 30 μC/cm^2. The difference of saturation polarization between the three curves may be accounted by a reduction of capacitance with frequency, as confirmed also by direct calculation of capacitance as

$$C = I(V = 0)\frac{dV}{dt} \tag{4.1}$$

The parallel capacitance due to silicon dioxide has been neglected since its dielectric permittivity is more than 100 times smaller than the one of barium titanate.

As discussed in section 3.3.1, in order to disentangle the ferroelectric part from the other contributions (leakage and dielectric currents) present in the dynamic hysteresis cycle, it is useful to perform a measurement with the PUND method.

Frequency	Capacitance	Saturation polarization	Remanent polarization
100 Hz	342 pF	34.1 μC/cm^2	11.0 μC/cm^2
1000 Hz	302 pF	30.5 μC/cm^2	10.6 μC/cm^2
3100 Hz	260 pF	27.2 μC/cm^2	12.2 μC/cm^2

Table 4.1: Dielectric and ferroelectric properties obtained from dynamic hysteresis measurements on BTO capacitors.

The result of a measurement of this kind, obtained from a train of triangular pulses of amplitude $\pm$7V and frequency 3125 Hz, is shown in Figure 4.5. The difference of current flowing between "positive" and "up" pulses and, similarly, between "negative" and "down" pulses is represented in Figure 4.5a; the resulting polarization curve is shown in Figure 4.5b.

Remanent polarization calculated with this method is 3 ± 0.5 μC/cm^2, with a clear reduction with respect to the value obtained from dynamic hysteresis. This value is more reliable, since the subtraction of non-switching currents leaves only the ferroelectric contribution. In particular, the dynamic hysteresis cycle is inflated by the integration of leakage current.

The obtained value of remanent polarization is reduced with respect of the one of bulk BTO (24.3 μC/cm^2) [93]. In BTO thin films, remanent polarization depends heavily on thickness, morphology and strain. By a proper engineering
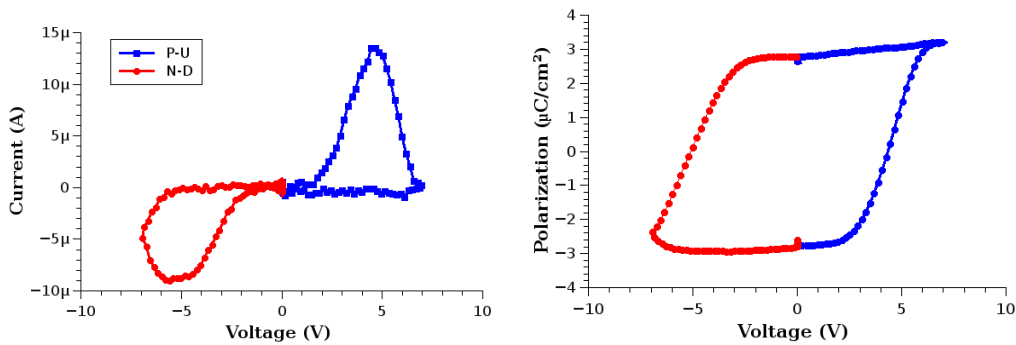
Figure 4.5: **a)** Ferroelectric switching current obtained from difference P-U (blue line) and N-D (red line) in a PUND measurement with amplitude 7V and frequency 3125 Hz. **b)** Ferroelectric polarization hysteresis cycle obtained from integration of the switching current over time.

of these parameters, remanent polarization values over 40 μC/cm^2 have been reported [94–96].

4.3   Electric Control of Magnetic Anisotropy

Control of magnetic anisotropy by application of a continuous voltage to BTO during measure has been widely discussed by A. Manuzzi [46]. Here we aim at demonstrating a purely ferroelectric control mechanism with the ferroelectric polarized in remanence, that is the operative condition of any realistic device. For this reason, magnetic measures described in this section have been performed in remanence upon polarization of BTO by voltage pulses.

Magnetic hysteresis cycles presented here are obtained by polar MOKE using the microMOKE setup described in section 3.3.2. Magnetic field is applied perpendicularly to the sample surface through coils driven by a KEPCO generator. The sample is wire bonded to a support and polarized before each measure by applying voltage pulses through the TF Analyzer 2000E employed also for ferroelectric characterization. With this specific apparatus, ferroelectric and ferromagnetic characterization can be made in a single setup, which allows to get an immediate feedback on a possible magnetoelectric coupling.

Each magnetic hysteresis cycle is taken upon application of three pulses (Fig-
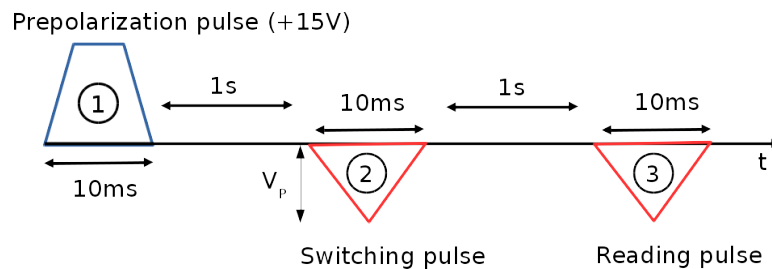
Figure 4.6: Pulse train applied to set ferroelectric polarization. Pulse ① saturates ferroelectric polarization in a specified direction. Pulse ② of amplitude V_P is applied in the opposite direction, possibly leading to a ferroelectric switch. Pulse ③ is the same as ② and is used to set a reference for non-switching current.

ure 4.6) to the device under test. Pulse ① (trapezoidal, 10 ms long) saturates ferroelectric polarization upward (downward) for V<0 (for V>0) . Pulse ② (triangular, 10 ms long) is applied with amplitude V_P in the opposite direction with respect to the first pulse. This is like a "positive" ("negative") pulse of a PUND measurement and allows to measure switching current. Finally, pulse ③ is identical in amplitude and duration to pulse ②. It is used to measure non-switching current like if it were a "up" ("down") pulse in a PUND train.

After this conditioning of the ferroelectric state, the MOKE measurement is performed. We note that for a magnetic characterization as a function of ferroelectric polarization would be sufficient to apply only the first two pulses, but since we are also interested to the ferroelectric characterization at the same time, a third pulse is also needed.

Examples of magnetic hysteresis loops measured by polar microMOKE, taken with this polarization method on a sample with t_{CoFeB}=1.1 nm presenting PMA, are shown in Figure 4.7a. Amplitude of pulse ① is -20 V in both cases. The red curve is taken upon application of V_P=-20 V so that the system remains in upward polarization state, while the blue curve is taken after application of
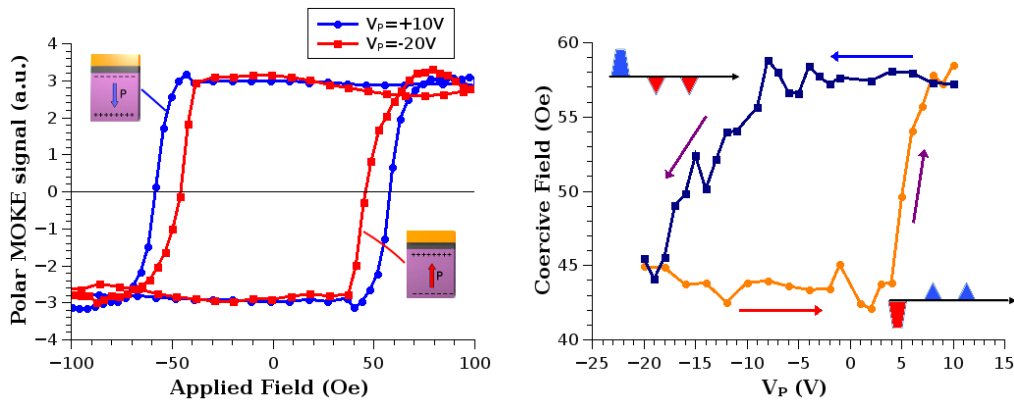
Figure 4.7: **a)** Magnetic signal versus applied field for different ferroelectric polarization. Red curve is for V_P=-20 V while blue curve is for V_P=+10 V. In both cases, prepolarization pulse ① amplitude is -20 V. **b)** Out-of-plane magnetic coercive field as a function of polarization pulse voltage V_P.

V_P=+10 V so that the system remains in downward polarization state. The consequent switch of polarization determines a variation of the coercive field of CoFeB, originated from a change of the magnetic anisotropy, from 45 Oe to 58 Oe at room temperature, with a modulation of 29%. Moreover, we verified that both states of polarization are stable, since no variation of coercive field have been observed for over 24 hours from application of the ferroelectric polarization. This is very important in view of applications in storage technology.

The trend of magnetic coercive field versus the amplitude V_P of pulses ② and ③ is shown in Figure 4.7b. Amplitude of pulse ① in the two branches of the cycle is respectively -20 V and +15 V. This choice is forced by the asymmetry of the leakage current (Figure 4.8) that, despite the intrinsic symmetry of the top-top measurements, presumably originates from defects in fabrication. Being the leakage asymmetric, the effective potential drop across the ferroelectric capacitor is different for positive and negative biases. This explains also the asymmetry in the hysteresis loop of Figure 4.7b (i. e. the ferroelectric coercive field for positive bias is lower than that at negative bias, namely +5 V and -10 V).

This sample, in particular, has been previously measured with application of
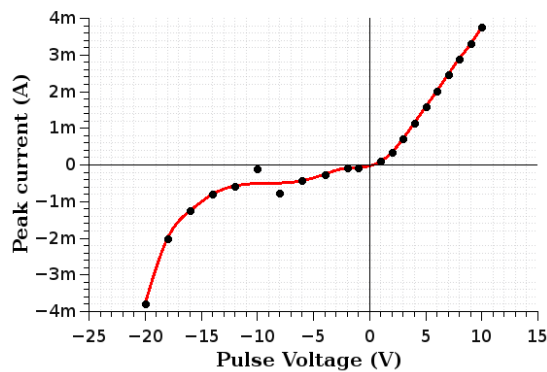
Figure 4.8: Peak current as a function of V_P. the red line is a guide for the eye. The asymmetric leakage determines different potential drop on ferroelectric capacitor for positive and negative biases resulting in a asymmetric ferroelectric hysteresis loop cycle.

large continuous voltage and the leakage is much higher than in newly fabricated samples. The leakage, in the order of mA, covers completely the ferroelectric switching current (few μA) and no meaningful information can be obtained from the current difference between pulse ② and ③. Nonetheless, despite the aging of the device, ferroelectric control of magnetic anisotropy is a persistent and robust effect that is still observable and reproducible.

Finally, the devices realized with nominal thickness of CoFeB layer 1.3 nm present an in-plane easy axis that is not affected by ferroelectric polarization. Since the macroscopic ferroelectric properties are similar in samples with 1.1 nm and 1.3 nm thick layers of CoFeB, this difference of behaviour has to be related to the different thickness of the magnetic layer. PMA, which is affected by polarization, is dominant, in fact, only for a small range of thicknesses; in thicker layers it becomes negligible compared to the shape anisotropy. Hence, to achieve the in-plane to out-of-plane transition, an equilibrium between different competing anisotropies has to be found. Considering that the contribution of interface effects leading to PMA decreases very rapidly with thickness, the tolerance related to the deposition (over 1 Å) may be too large to achieve such a delicate equilibrium.

4.4 Conclusions

Summarizing this first part of my experimental activity, we characterized ferroelectric capacitors with ferromagnetic electrodes based on the Ta/CoFeB/BTO/LSMO//STO (001) template, showing non-volatile ferroelectric control of perpendicular magnetic anisotropy.

Ferroelectric measurement were performed on different batches of devices, prepared in different times, with similar results. Dynamic hysteresis cycles showed, at all the frequencies, a saturation polarization of about 30 μC/cm^2. Since in hysteresis measurements dielectric and resistive (leakage) contributions are also

present, the value of remanent ferroelectric polarization has been measured with the PUND method, in order to exclude spurious contributions, giving a value of $3 \pm 0.5 \ \mu C/cm^2$.

On previously fabricated samples with CoFeB thickness 1.1 nm, we demonstrated ferroelectric control of perpendicular magnetic anisotropy in remanence, by observing a relative increase of coercive field between upward and downward polarization states of 29%. The variation of coercive filed in these samples by application of DC voltage, range from 25% to 70% [46]. However, from the applications point of view, a purely ferroelectric control as demonstrated here is more appealing, since there is no static dissipation of power.

It is worth to notice, at last, that the sign of this effect is the opposite of the one predicted for Fe/BaTiO$_3$ interface and discussed in section 2.3.2. If the theoretical results were right, this would mean that CoFeB PMA has a radically different origin from the one of epitaxial Fe on BTO.

Finally, the idea to increase CoFeB thickness to ease the transition from out-of-plane to in-plane magnetization has actually proven non-trivial to implement. A different approach would require instead an optimization of ferroelectric properties of BTO in order to be able to observe a larger modulation of the magnetic properties. In perspective, BTO growth will be re-optimized in order to increase the ferroelectric polarization above the actual 3 $\mu C/cm^2$, while maintaining, or improving, the PMA and its electrical control of the CoFeB film grown on top.

Another strategy to obtain the electrical control of magnetism is based on the Fe/BTO/FM system, where the Fe at BTO interface can undergo a FM/AFM transition caused by the change in ferroelectric polarization of the thin BTO layer used as a barrier. In the next chapter, we are going to investigate this different solution employing Fe instead of CoFeB according to the very encouraging results achieved by the NaBiS group on the Fe/BTO systems [30].

Chapter 5

Fe/BaTiO$_3$/La$_{0.67}$Sr$_{0.33}$MnO$_3$ Multiferroic Tunneling Junctions

This chapter describes the part of this thesis work dedicated to realization and characterization of Multiferroic Tunneling Junctions (MFTJs) based on the Au/Co/Fe/BTO/LSMO template. Samples with different BTO barrier thickness, were grown, patterned and characterized in terms of their magnetoresistive and electroresistive properties.

At first, section 5.1 presents the preliminary measurements that confirmed ferroelectricity of ultrathin BaTiO$_3$ films. Then, in section 5.2, the structure of MFTJs and the processing needed for device realization is described.

In section 5.3, results of electrical characterization and analysis within the Brinkman model are shown, demonstrating a clear tunnelling electroresistance of over 100% in thicker samples (BTO barrier 4 nm thick). In section 5.4, instead, spin dependent tunnelling characterization is described, with measured values for TMR below 1%. Despite the low TMR, coupling between magnetism and ferroelectric polarization is proven by demonstrating ferroelectric control of the tunnel magnetoresistance.

5.1 Characterization of Ultrathin BTO Films

Before the realization of MFTJs, no previous work of NaBiS group employed ultrathin ferroelectric films. To confirm that ferroelectricity is preserved despite the low thickness (2-4 nm) of BTO, piezoresponse force microscopy (PFM) has been performed on a BTO (4 nm)/LSMO (50 nm)// STO (001) test sample (the same template is used in the junctions). PFM analysis is necessary in this case since no information can be obtained on ferroelectric films so thin from the characterization techniques described in section 3.3.1.

A PFM image is shown in Figure 5.1a. The stable ferroelectric remanence is confirmed by the clear contrast between the 3×3 μm^2 square previously written with upward polarization and the internal 1.5×1.5 μm^2 square written with downward polarization. The phase versus applied voltage (Figure 5.1b) shows a squared hysteresis cycle with phase jumps at about -3V and +1.5V.

Surface roughness (RMS) of 1.6 Å has been measured on 3×3 μm^2 area by AFM , and resulted to be essentially the same one measured on the annealed STO substrate (1.2 Å). This confirms that the growth conditions employed for BTO and LSMO are the optimal ones for obtaining atomically flat surfaces.

<center>(a)   (b)</center>
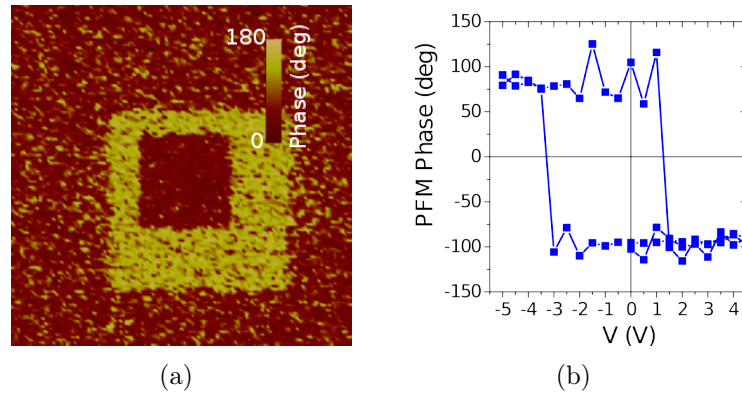
Figure 5.1: **a)** PFM phase image of a 4 nm thick BTO film grown on LSMO. Image recorded after writing an area of 3×3 μm^2 with -5 V and then the central 1.5×1.5 μm^2 square with +5 V using a biased conductive tip. **b)** PFM phase as function of applied voltage.

5.2   Device Design

Multiferroic tunneling junctions were fabricated on Au(10 nm)/Co(1 nm)/Fe (0.28 nm)/BTO(t_{BTO})/LSMO(50 nm) heterostructures with t_{BTO}=2,3,4 nm grown on (001)-oriented $SrTiO_3$ single crystal substrates. We note that 0.28 nm of Fe corresponds to 2 monolayers (the layer spacing of bcc Fe(001) is 0.14 nm). The structure of a complete MFTJ is represented in Figure 5.2.

LSMO is chosen as bottom electrode because, being a perovskite oxide with similar lattice parameter with respect to BTO and STO, it allows epitaxial growth of BTO; moreover it is a ferromagnetic half metal, for which it is predicted a spin polarization (see Section 2.1.1) near unity at cryogenic temperature (95% at 4 K [97]). BTO and Fe are chosen as ferroelectric barrier and ferromagnetic top electrode, respectively, because of the expected ME coupling effects described in section 2.3.1. Furthermore, epitaxial growth of Fe on BTO (with a relative rotation of 45 degrees between the two lattices to minimize lattice mismatch) has been previously optimized by the NaBiS group [98].

To reproduce the conditions in which the magnetoelectric transition of Fe oxide from ferromagnetic to antiferromagnetic was demonstrated in a recent work of our group [30], thickness of the Fe layer has been mantained the same (2 mono-
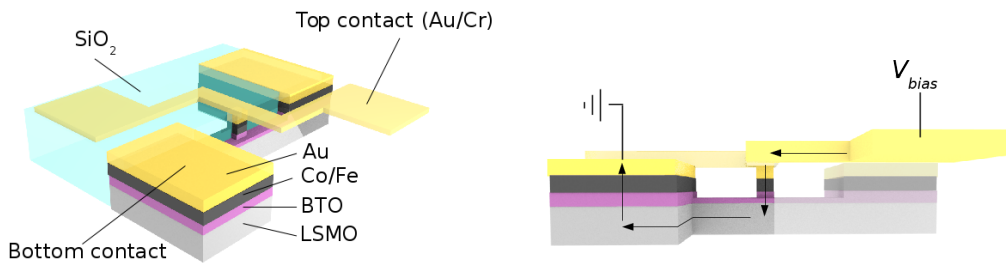
Figure 5.2: **a)** 3D view of a complete multiferroic tunneling junction. The bottom contact is a junction itself but its dimension give rise to a low resistance, negligible respect to the real junction one. **b)** Side view of the structure illustrating the current flow from top to bottom contact in a two probe measurement.

layers). Cobalt is then grown on top in order to stabilize the magnetization of the ultrathin iron film. Finally, a gold capping is added to protect the underlying layers from oxidation due to air exposure.

Each junction is connected in cross-strip geometry (Figure 5.2a) by two top and two bottom contact pads, thus allowing four points measurements. The current path across the tunnelling barrier is sketched in Figure 5.2b. Bottom contacts are junctions themselves but, thanks to their greater area, their series resistance is negligible respect to the real junction one. To grant proper insulation between top and bottom contacts, a 30 nm thick layer of SiO$_2$ is added during the lithographic process.

5.2.1   Growth Process

Multilayers required for MFTJs were grown by combined use of pulsed laser deposition and molecular beam epitaxy in the LASSE system described in section 3.1.

Samples with BTO thickness of 2, 3 and 4 nm were realized in order to investigate dependence of electroresistive and magnetoresistive behaviour on barrier width. Except for the ferroelectric barrier thickness, the multilayer is similar to the one employed in reference [30] and the previously optimized growth conditions have been maintained the same.

The various steps of the growth process are listed below. Each step is taken consecutively without breaking the vacuum regime, in order to obtain surfaces as clean as possible and free of contaminations.

1. SrTiO$_3$ substate annealing at 1000K for 30' to clean and order the surface.

2. Deposition of 50 nm of LSMO by PLD in the conditions reported in Table 3.1.

3. Deposition of 2-4 nm of BTO by PLD in the conditions reported in Table 3.1.

4. Annealing at 873K for 30' and cooling for 30' in oxygen atmosphere (0.5 bar) to improve BTO structure and oxygen stoichiometry.

5. Deposition by MBE of 2 monolayer of Fe (2.86Å).

6. Annealing at 473K for 20' to improve Fe crystalline quality.

7. Deposition of 1 nm by MBE of Co to stabilize Fe magnetization.

8. Deposition of 10 nm of Au by MBE to protect underlying layers from oxidation.

Steps 5-8 are performed in ultra high vacuum conditions ($p \leq 1 \cdot 10^{-9}$ mbar). Before and after the Fe deposition, X-ray photoemission spectroscopy (XPS) analysis is conducted on the sample in order to have a feedback on BTO stoichiometry and deposited Fe thickness. After growth completion, the sample is removed from the vacuum system and undergoes the lithographic process described in the next section.

5.2.2   Lithograhic Process

Lithography of MFTJs require three steps of process, as illustrated in Figure 5.3. Patterning is done by UV lithography and Ar ion beam etching as described in section 3.2. The whole process is summarized here:

1. Definition of the mesa structure (Figure 5.3a)

    (a) Deposition of 1.25 μm thick AZ5214E photoresist, exposition to about 125 mJ/cm^2 dose of UV light with mask 1 and development (30 sec in AZ 726 MIF, water as stopper).

(b) Ion beam etching down to the insulating substrate (STO). Etching depth in this step is not crucial as long as any conductive path between different mesas is removed. Process time is calculated upon etching rates previously obtained by AFM profilometry on test samples. At the end of the process, effective insulation between different structures is checked by electrical measurements.

(c) Photoresist strip in AZ 100 Remover.

2. Definition of junction area and bottom electrodes (Figure 5.3b)

   (a) Deposition of 1.25 μm thick AZ5214E photoresist, exposition to about 125 mJ/cm^2 dose of UV light with mask 2 and development (30 sec in AZ 726 MIF, water as stopper).

   (b) Ion beam etching to define the pillar and bottom pads. In this step a *flag* made of Au/Co/Fe layers is used as reference for the etching
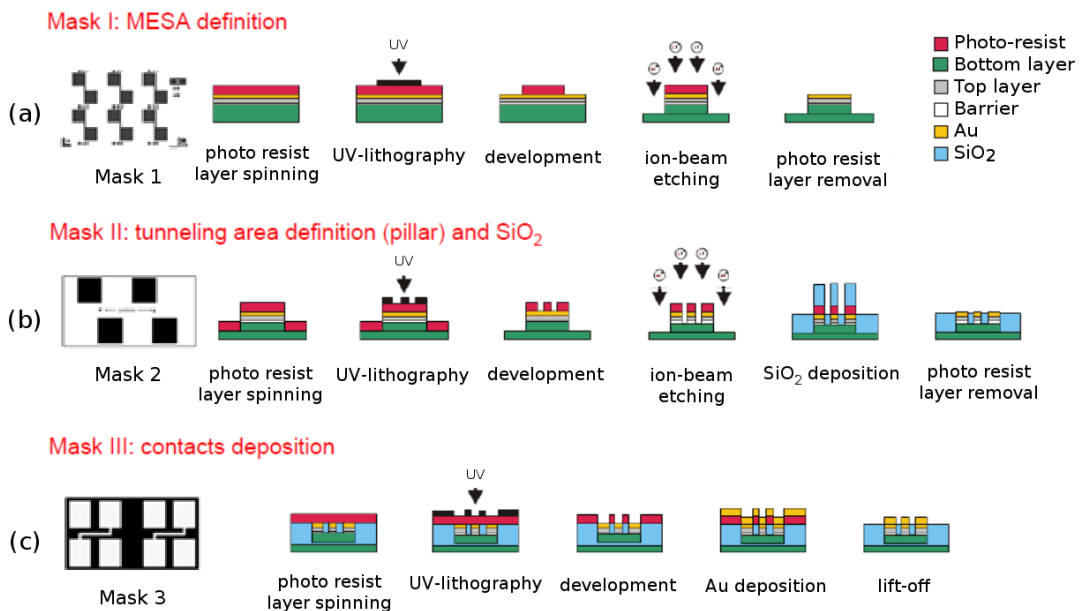
Figure 5.3: Schematic of the lithographic process employed to realize multiferroic tunnelling junctions.

time. An excessive etching leads to erosion of the bottom layer and consequent disconnection of the bottom electrodes from the junction; a short etching leaves part of the top layer which cortocircuits the junctions.

(c) Deposition by sputtering of SiO_2 (30 nm) to prevent shorcuts between top and bottom electrodes.

(d) Lift-off in AZ 100 Remover.

3. Lithography of top contacts (Figure 5.3c)

   (a) Deposition of 1.25 μm thick AZ5214E photoresist, exposition to about 125 mJ/cm^2 dose of UV light with mask 3 and development (30 sec in AZ 726 MIF, water as stopper).

   (b) Electronic evaporation of the contacts (7 nm of chromium as adhesive layer, 300 nm of Au).

   (c) Lift-off in AZ 100 Remover.

At the end of the process a single substrate (10 x 10 mm) can arrange up to 36 junctions with different shape and area ranging from 4 μm^2 to 1600 μm^2.

5.3   Electrical Characterization

Electrical measurements were performed in two and four-probe geometry (for details see section 3.3.3). In most of the devices, the junction resistance is over 100 times larger than the one of the contacts, and the two methods give almost identical results.

Measurements were taken both at room temperature and in a helium cooled cryostat. In the first case a Keithley 236 sourcemeter and a Keithley 182 voltmeter were employed connected to a mechanical probe station. In the second,

(a)   (b)
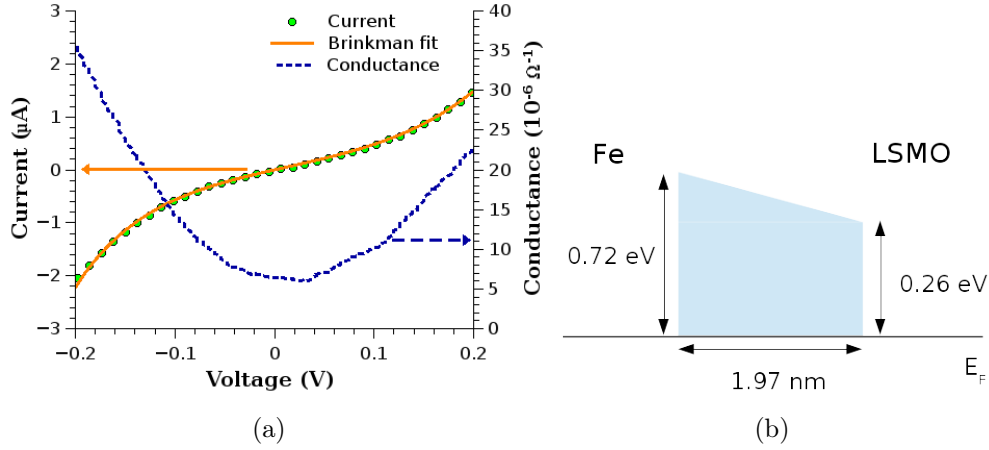
Figure 5.4: **a)** Current-voltage characteristic (green dots), fit with Brinkman model (orange line) and differential conductance (blue dashed line) of a 15 $\times$ 15 μm^2 junction with 2 nm thick BTO barrier measured at room temperature. **b)** Representation of the trapezoidal potential barrier resulting from the fit with Brinkman model.

junctions were wire bonded to a support and connected to a Keithley 2611 sourcemeter + voltmeter.

In order to investigate tunnelling transport, the I-V curve of each junction has been measured. The typical electrical current-voltage characteristic (green circles) and differential conductance (blue dashed line) of a 2 nm thick junction at room temperature is shown in Figure 5.4a. In this figure and in the following a positive voltage correspond to current flow from top to bottom contacts.

As expected for tunnelling transport, the characteristic is highly nonlinear. The conductance, calculated as dI/dV, has a minimum near zero and shows a parabolic-like trend.

The asymmetry of the curve is attributable to different barrier heights at the electrode interfaces. To estimate these quantities, numerical fitting of the data has been carried on within the Brinkman model (equation 2.5).

By imposing multivariable regression on left and right barrier heights as well as on the barrier width, a reasonable approximation of the curve is achieved. Best results have been obtained fixing in the model a effective tunnelling mass $m^* \simeq$

$2m_0$ (m_0 is the electron rest mass), coherently to the fit done by Chanthbouala *et al.* with the same model, on Co/BTO/LSMO FTJs [64]. In particular, for the junction of Figure 5.4a, barrier heights of 0.26 eV and 0.72 eV are estimated. Barrier witdh d results 1.97 nm, in good agreement with the nominal thickness of BTO (2nm). The resulting trapezoidal potential barrier is represented in Figure 5.4b.

A further confirmation of tunnelling behaviour comes from the analysis of the junctions resistance as a function of temperature. The peculiar bell shaped curve of Figure 5.5 is typical of LSMO-based MTJs [26, 29, 99] and follows from the transition of the LSMO surface from paramagnetic oxide to ferromagnetic half-metal at about 200K. Moreover, the bell shape allows to exclude short circuits between electrodes, that would introduce a parallel ohmic transport channel, and oxygen vacancies in BTO, that would be detrimental for its ferroelectric properties [100]. In fact, if a short circuit were present, the continuous decrease of resistance typical of metals would be observed. At the contrary, if oxygen vacancies were present in BTO, a continuous increase of resistance would be measured [101].
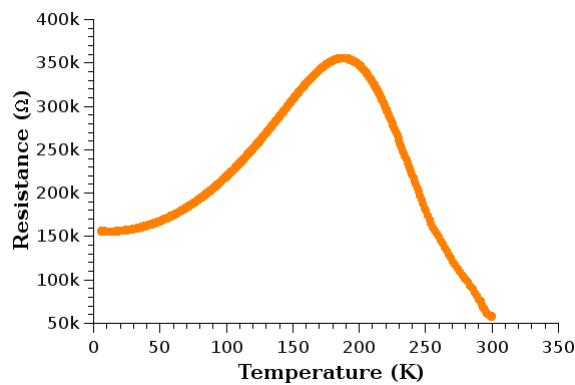
Figure 5.5: Resistance at V_{bias} = 50 mV as a function of temperature in the case of a 15×15 μm^2 junction with 2 nm thick BTO barrier.

5.3.1 Electroresistance measurements

In order to investigate electroresistive behaviour of MFTJs, the ferroelectric polarization of the BTO barrier layer was changed by manually applying bipolar voltage pulses with amplitude up to 3 V and 0.5 s duration.

I-V curves were collected upon polarizing BTO barrier layer with positive or negative V_{write} pulses, corresponding to the ferroelectric polarization of BTO pointing down ($P_\downarrow$) or up ($P_\uparrow$) respectively.

Figure 5.6a,b show electrical characteristic upon V_{write} =-3 V and V_{write} =+3 V poling (red and blue lines, respectively) of two representative junctions with nominal barrier thickness of 3 nm and 4 nm.

The curves reveal a clear resistance difference between positively ($P_\downarrow$) and negatively ($P_\uparrow$) poled devices. Junctions are in high resistance state when a sufficiently high positive V_{write} is applied to the contacts to polarize BTO downward ($P_\downarrow$), and switches to low resistance state when ferroelectric polarization is revered by large enough negative V_{write} ($P_\uparrow$). TER ratio measured at +300 mV is about 40% in junctions with barrier thickness of 3 nm and over 100% for junctions with barrier of 4 nm.

Barrier representations obtained from Brinkman model in these two cases are shown in Figure 5.6c,d. The values obtained from fitting of these curves are reported in Tables 5.1 and 5.2. Asymmetry $\Delta\phi = \phi_L - \phi_R$ of the barrier changes coherently with ferroelectric polarization of about 0.24 eV. The average barrier height $\phi_{av} = (\phi_L + \phi_R)/2$ changes as well and is higher of 0.03-0.04 eV for polarization pointing towards LSMO ($P_\downarrow$), suggesting, in the picture of section 2.2.1, a shorter screening length for LSMO than for Fe. Finally, the similar barrier profile resulted from fitting implies that the difference in terms of TER modulation between these two devices, with nominal barrier thickness of 3 nm and 4 nm, has to be related only to the different barrier width and not to different interface conditions or ferroelectric properties.
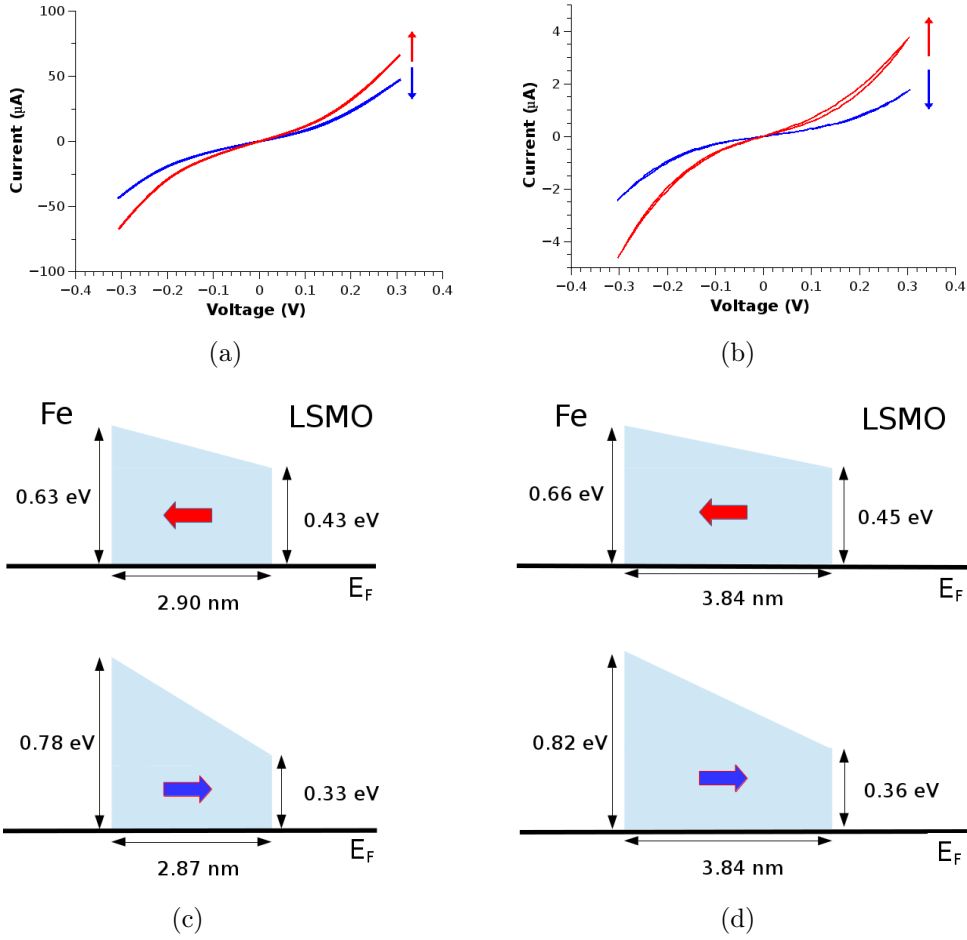
Figure 5.6: I-V curves taken at room temperature in $P_\uparrow$ and $P_\downarrow$ states (red and blue lines, respectively) of a MFTJ with **a)** BTO thickness 3 nm and junction area 125 μm^2, and **b)** BTO thickness 4 nm and junction area 900 μm^2 . **c),d)** Trapezoidal barrier representation for the different states of polarization as obtained from fitting of data in the Brinkman equation.

State	ϕ_L (eV)	ϕ_R (eV)	$\Delta\phi$ (eV)	ϕ_{av} (eV)	d (nm)
$P_\downarrow$	0.78	0.33	0.45	0.56	2.87
$P_\uparrow$	0.63	0.43	0.20	0.53	2.90
Variation	0.15	-0.10	0.24	**0.03**	-0.03

Table 5.1: Values obtained from fitting of current-voltage characteristic represented in Figure 5.6a (BTO 3 nm)

State	ϕ_L (eV)	ϕ_R (eV)	$\Delta\phi$ (eV)	ϕ_{av} (eV)	d (nm)
$P_\downarrow$	0.81	0.36	0.45	0.59	3.84
$P_\uparrow$	0.66	0.45	0.21	0.55	3.84
Variation	0.15	-0.9	0.24	**0.04**	0

Table 5.2: Values obtained from fitting of current-voltage characteristic represented in Figure 5.6b (BTO 4 nm)

Differently from the other two, the sample with 2 nm thick BTO did not show TER at room temperature. However, measures performed at 20 K gave TER ratio up to 10% and the expected hysteretic loop of resistance versus V_{write} (Figure 5.7). In this sample, TER rapidly decreases with temperature and halves already at 80 K. This behaviour is probably due to a lowering of the ferroelectric Curie temperature in approaching the thickness limit for ferroelectricity.
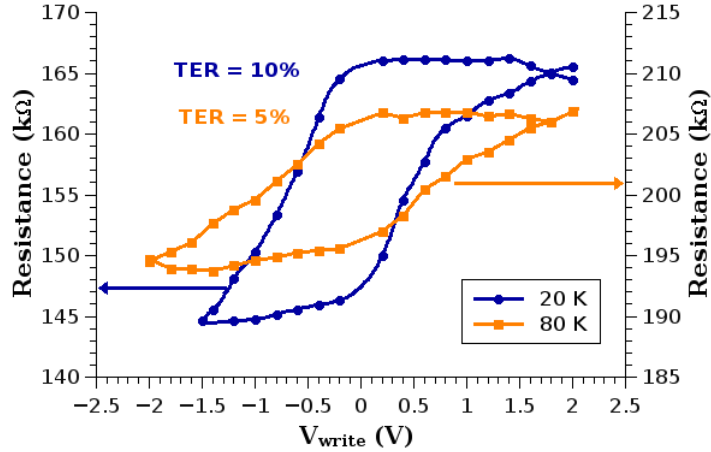
Figure 5.7: Resistance at V_{bias}= 50 mV as a function of polarization voltage V_{write} in the case of a 15 × 15 μm^2 junction with 2 nm thick BTO barrier cooled at 20K (blue line) and 80K (orange line).

5.4 Tunnel Magnetoresistance Measurements

Magnetoresistance measurements of the junctions were performed in four-probe geometry in a helium cooled cryostat with the same methods and conventions

described in the previous section. Magnetic field was applied externally with an electromagnet powered by a Kepco generator. The field direction was set in the plane of the sample, parallel to the (100) crystallographic axis of Fe, that is also its magnetic easy axis.

Resistance versus field curves were collected upon polarizing BTO barrier with positive or negative V_{write} pulses, corresponding again to downward $(P_\downarrow)$ and upward $(P_\uparrow)$ polarization respectively. Magnetoresistive characterization has been performed in detail only on BTO(2 nm) sample obtaining values of TMR below 0.6%. Even though TMR was still detectable on BTO(3 nm) sample, with comparable values, measures were affected by noise of order of 0.2% related to higher resistance and ferroelectric creep.

Examples of TMR curves taken at 20 K on a 15×15 μm^2 junction with 2 nm thick barrier are shown in Figure 5.8a for -80 mV bias voltage and 5.8b for +80 mV bias voltage. In both cases the polarization state is $P_\uparrow$.

The resistance versus magnetic field loops present a butterfly shape that indicates spin dependent tunnelling of electrons. Maximum value of TMR is calculated at an applied field of 48 Oe, however, there is not a clear *plateau* that proves fully antiparallel alignment. This is probably due to very similar coercive fields

(a) TMR curves at -80 mV bias   (b) TMR curves at +80 mV bias
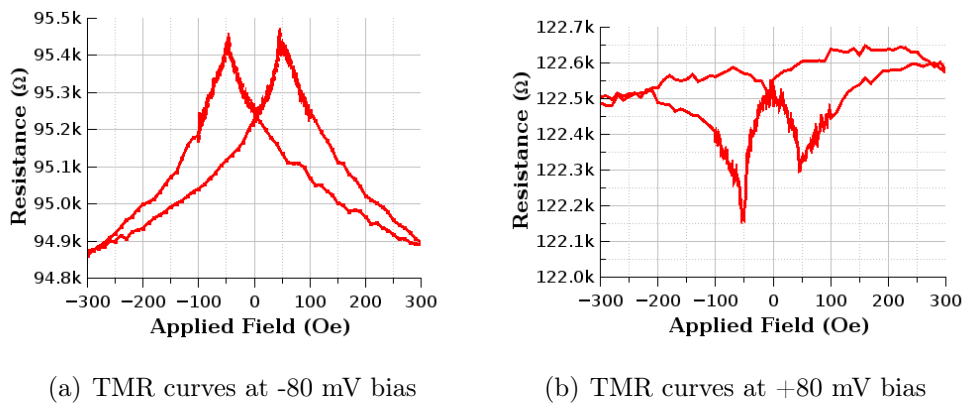
Figure 5.8: TMR measurements at 20 K on a 15×15 μm^2 junction with 2 nm thick BTO barrier. **a)** Resistance at -80 mV versus field in $P_\uparrow$ state. **b)**Resistance at +80 mV versus field in $P_\uparrow$ state

of epitaxial Co/Fe and LSMO layers and to interaction between magnetic layers. Coupled magnetic layers tend to stay aligned even during ferromagnetic switching and magnetic moments of the two layers are never in antiparallel configuration. The net effect is a small disalignment of magnetization and, consequently, a very small change of resistance. Nonetheless, TMR values even under 0.6% are fairly well measurable in this sample.

Furthermore, the curves represented in Figure 5.8 show a radical different behaviour at -80 mV and at + 80 mV. In the first case the "antiparallel" (AP) state of magnetization (denoting with antiparallel the point of maximum resistance variation with respect to the parallel state) presents an higher resistance than the parallel (P) state. In the second case, the opposite is true: the lower resistance is measured in the AP configuration.

In other systems that show this behaviour [102–106], the phenomenon is commonly explained considering the alignment of bands at different bias voltage, as pictured in Figure 5.9. Inverse TMR ($R_P > R_{AP}$) is favoured when regions of the DOS with opposite spin polarizations are aligned in the first and in the second ferromagnetic layer (Figure 5.9a), while normal TMR ($R_P < R_{AP}$) is observed
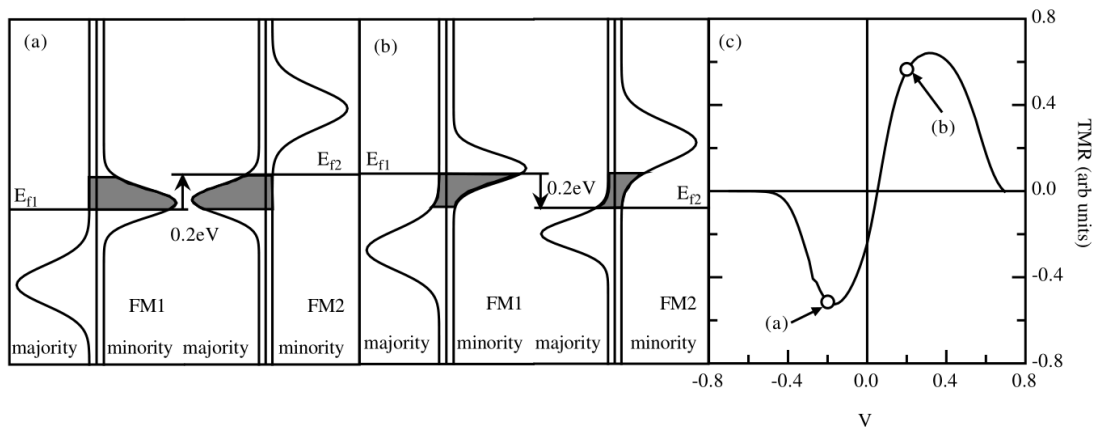
Figure 5.9: Simple model to explain inverse magnetoresistance for an hypothetical DOS. Shaded regions show portions of the DOS that take part in the tunnelling process. **a),b)** FM2 biased at -0.2V (+0.2V) with respect to FM1, **c)** Resultant TMR versus bias curve (from [102]).

when the sign of spin polarizations is the same (Figure 5.9b). In this way, the relative shift of eV_{bias} between electronic bands of the two ferromagnets FM1 and FM2 may determine a change of sign of TMR (Figure 5.9c).

5.4.1 Ferroelectric control of spin dependent transport

We consider now the role of ferroelectric polarization on spin dependent transport. A comparison of TMR curve taken at 20 K in opposite states of polarization is shown in Figure 5.10a for V_{bias}=-80 mV and 5.10b for V_{bias}=+80 mV. At this

(a) TMR curves at -80mV bias

(b) TMR curves at +80mV bias

(c) Bias dependence of TMR
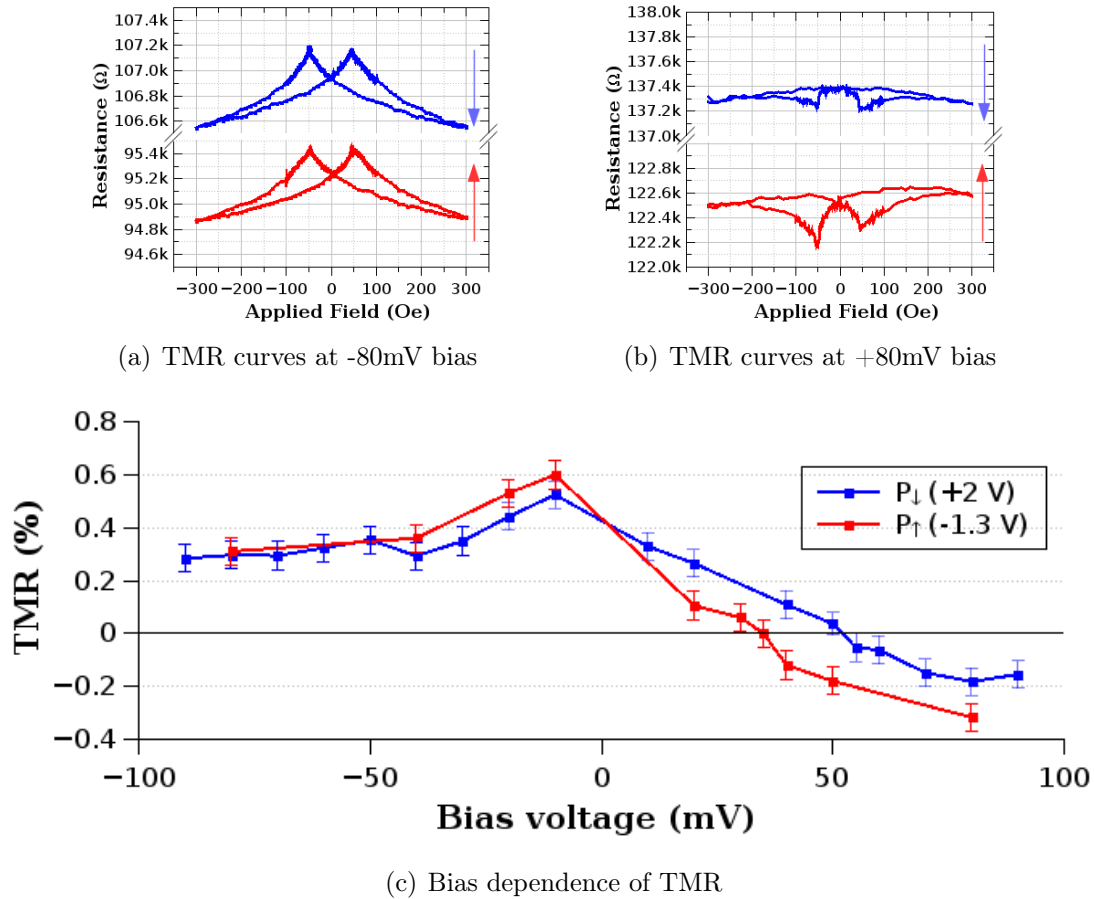
Figure 5.10: TMR measurements at 20 K. **a),b)** Resistance versus field loops at -80mV (+80mV) for two opposite states of polarization in a $15 \times 15 \ \mu m^2$ junction with 2 nm thick BTO barrier. **c)** TMR ratio as a function of bias voltage for the same device.

temperature, V_{write} has been limited in the range +2V and -1.3V in order to avoid current densities higher than $8 \cdot 10^3 A/cm^2$ and to preserve the junction.

At V_{bias}=-80 mV, TMR values are mostly similar in the two ferroelectric polarizations and the only macroscopic difference between the two resistance versus field curves is due to the TER (11.8%) of the junction. Nevertheless, for +80 mV, a larger absolute value of TMR is measured for upward polarization (0.32%) than for downward polarization (0.17%). Furthermore, also the point in which TMR changes its sign is dependent on ferroelectric polarization, as can be seen from the plot of TMR as a function of bias voltage and polarization (Figure 5.10). For upward polarization, a shifts toward smaller biases (+35 mV instead of +50 mV) of the inversion point is registered.

Finally, ferroelectric control of spin polarization is utterly confirmed by the repeatable switch between negative and positive TMR at +40mV bias voltage upon positive and negative polarization of the ferroelectric barrier as shown in Figure 5.11.
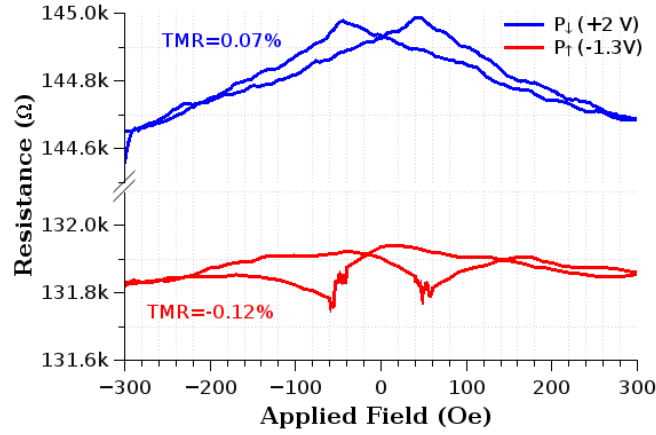
Figure 5.11: Resistance versus field curve at V_{bias}= 40 mV in the case of a 15 × 15 μm^2 junction with 2 nm thick BTO barrier measured at 20 K. TMR sign changes from positive to negative between downward polarization (blue curve) and upward polarization (red curve).

5.4.2 Temperature dependence of TMR

To further investigate dependence on temperature of the behaviour observed at 20 K, cycles of TMR versus bias voltage were collected also at 80 K and 110 K. The results are shown in Figure 5.12. The change of sign is not influenced by temperature, and is repeated almost at the same bias. In the curve taken at 110 K, however, the low ferroelectric polarization does not allow to see a clear difference in the curves for opposite states of polarization, even if a TER=3% is still measurable.

(a) 80 K (b) 110 K
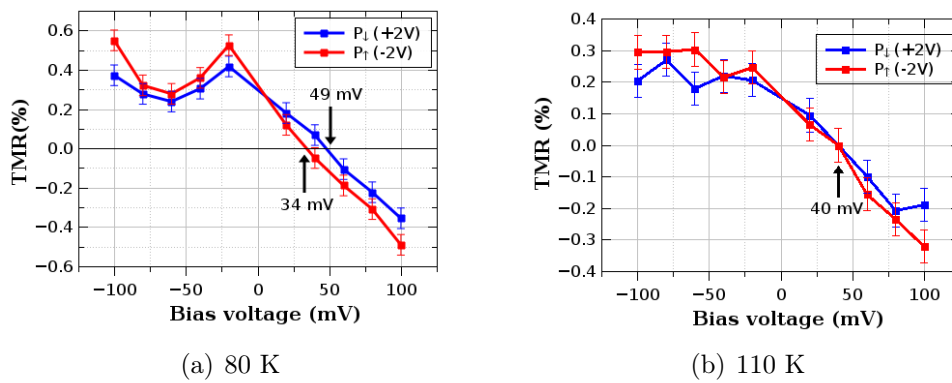
Figure 5.12: TMR as a function of bias voltage in a $15 \times 15 \ \mu m^2$ junction with 2 nm thick BTO barrier. **a)** Measure at 80 K. **b)** Measure at 110 K.
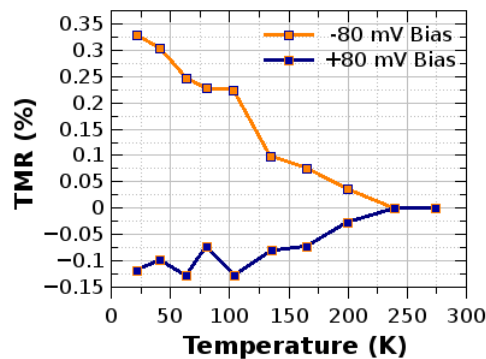
Figure 5.13: TMR as a function of temperature in the $P_\downarrow$ state. Positive (negative) TMR is calculated at -80 mV (+80 mV). TMR is not observed over 200 K coherently with the phase transition of LSMO interface.

TMR values decrease with temperature as shown in Figure 5.13, and disappear at about 200 K, in correspondence of the phase transition of the manganite interface (peak of Figure 5.5).

In conclusion, the four states of resistance, determined by the relative orientation (P or AP) of the magnetic electrodes and direction of the ferroelectric polarization ($P_\downarrow$ and $P_\uparrow$), are observed only below room temperature. Further optimization of the stack is needed in order to achieve larger TMR values and, possibly, to realize a four-state memory that works at room temperature.

5.5   Discussion

We fabricated multiferroic tunneling junctions by means of optical lithography, starting from epitaxial Au/Co/Fe/BTO/LSMO//STO (001) heterostructures grown by PLD and MBE.

We measured devices at room temperature for different states of polarization, and found non linear I-V curves indicating that tunnelling across the ferroelectric barrier is the main transport mechanism. Tunnelling electroresistance is in the order of 40% for 3 nm thick BTO sample and 100% for the 4 nm thick one, with very small dependence on reading voltage. Sample with 2 nm thick barrier show TER only at low temperature. By fitting the curves with the Brinkman model, we estimated barrier heights (on the Fe and LSMO sides) for both polarization verses and found a relevant change of barrier profile.

We performed also TMR measurements at low temperature on BTO (2 nm) showing both TMR and TER. TMR values are limited to values below 1%, probably due to the coupling of magnetic layers. The TMR of these devices is positive for negative bias, while becomes negative for big enough positive voltages (inverse TMR). Such a inverse MR depends on the polarization state of BTO: for upward polarization, inverse TMR values are higher and sign inversion shifts accordingly to lower bias voltage.

Ferroelectric control of spin polarization was already observed in similar MFTJ structures. In Fe/BTO/LSMO nanojunctions, a TMR change from -3% to -17% between downward and upward polarization states was reported in reference [26], anyway, the results here presented are quite different. In the case of nanojunctions, the greater coercive field of Fe (over 1 kOe at 4 K) allowed to see more defined TMR peaks. Nevertheless, only inverse TMR and no sign inversion was reported. This could be related to the different interface conditions between sputtered Fe of nanojunctions [26] and epitaxial Fe grown on BTO in situ of our devices. This difference is suggested also by the reduced barrier height at Fe interface (0.475 eV), calculated for nanojunctions with respect to ours (0.6-0.8 eV).

The sign of the modulation of TMR observed in our junctions is coherent with the electrically-driven transition of Fe oxyde from ferromagnetic to antiferromagnetic reported by our group in reference [30] and discussed in section 2.3.1. In fact, the additional antiferromagnetic layer expected for downward polarization would reduce the spin polarization at Fe interface and hence cause a reduced TMR. However, since the modulation is clearly distinguishable for inverse TMR, but not so clearly in the case of normal TMR, this behaviour could be also accounted on the base of the effect predicted by Duan *et al.* in reference [39] (see section 2.3.1). In conclusion, even if the results are in agreement with the electrically-driven magnetic transition of the oxidized Fe layer, they could not be unequivocally related to this magnetoelectric effect.

Regarding instead the bias dependence of TMR, even though a complete description would require dedicated *ab initio* transport calculations, we could make some assumptions.

As introduced in section 5.4, bias dependence of TMR sign is related to the alignment of bands with opposite spin polarization depending on the applied potential. Being LSMO a ferromagnetic half metal, it is predicted that only majority-spin electrons are present near the Fermi level. So, as a first approximation, the change of sign we observed should be related only to the DOS of the
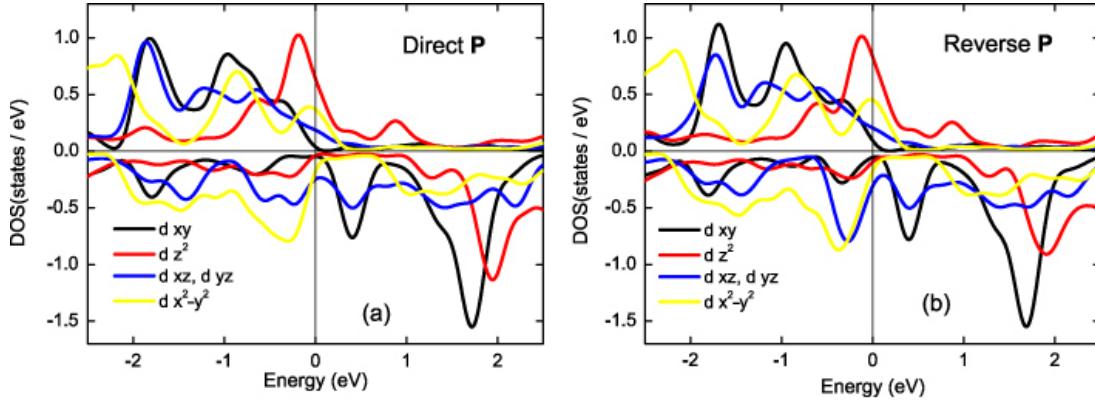
Figure 5.14: Calculated orbital resolved DOS for the first layer of Fe in an ideal BaTiO$_3$/Fe interface, for upward polarization (left) and downward polarization (right) (from [70]).

Fe layer.

Symmetry based spin filtering is predicted for BTO barriers [107,108] and the only propagating states expected have symmetry $\Delta_1(s, p_z, d_{z^2})$ or $\Delta_5(p_x, p_y, d_{xz}, d_{yz})$. Limiting our analysis to d electrons, this result would suggests to consider primarily d_{xz}, d_{yz} (which are degenerate in absence of spin orbit coupling) and d_{z^2} bands of Fe.

In Figure 5.14, calculated orbital resolved DOS for Fe at BTO interface is shown for both states of polarization. From the plot results that the d_{z^2} band (red line) has a definite majority-spin character anywhere near the Fermi level and below. However, the orbital DOS rapidly decrease above E_F where d_{xz} and d_{yz} bands (blue line) have instead a definite minority-spin character.

Assuming that only these electronic states participate in tunnelling, even without considering different attenuation in the barrier, we obtain a simplified DOS as sketched in figure 5.15, with positive spin polarization at Fermi level and below, and negative spin polarization a little above E_F.

In agreement with the description given in Figure 5.9, this would determine two opposite behaviour for large enough positive and negative biases.

For V < 0 (Figure 5.15a), electrons tunnel from occupied states of Fe to
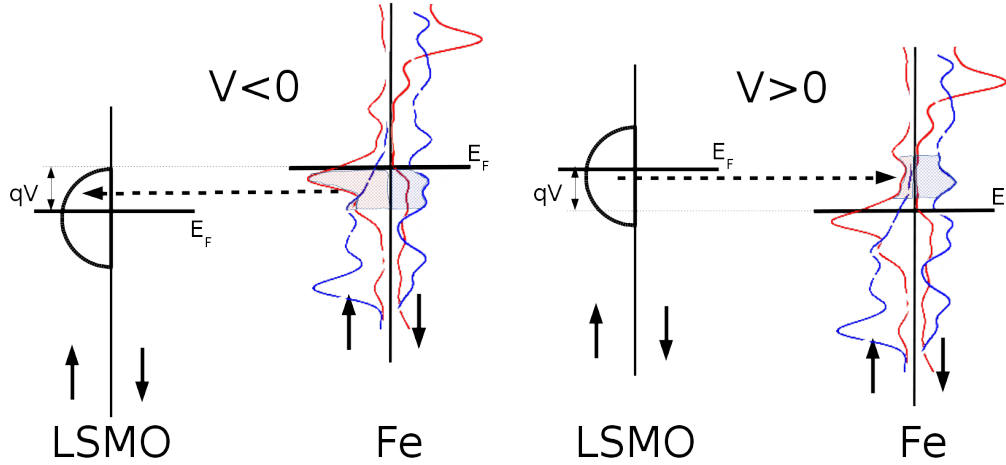
Figure 5.15: Hypothetical coherent tunnelling process in epitaxial LSMO/BTO/Fe multiferroic tunnelling junctions. **a)** Band alignment for negative bias. Effective spin polarization of Fe is positive and normal TMR is expected. **b)** Band alignment for sufficiently high positive bias. Due to the rapid decrease of d_{z^2} orbital DOS above Fermi level, the effective spin polarization of Fe may become negative, resulting in inverse TMR.

empty states of LSMO. The latter have only majority-spin character; likewise, the occupied Fe states have positive spin polarization and tunnelling is favoured for parallel alignment (normal TMR).

For $V > 0$ (Figure 5.15b), majority spin electrons tunnel from LSMO to Fe. Near the Fermi level, spin polarization of Fe states is still positive due to the high majority-spin DOS of d_{z^2} electrons. Since this band rapidly decreases and the d_{xz}/d_{yz} minority-spin DOS increases above E_F, for larger positive biases the effective spin polarization becomes negative, and tunnelling is favoured for antiparallel alignment (inverse TMR).

Furthermore, both d_{z^2} and d_{xz}/d_{yz} orbital DOS results from calculations to be dependent on BTO polarization (comparison between Figure 5.14a and b). In particular, the rigid shift towards higher energies in majority-spin d_{z^2} band for downward polarization could explain the higher crossing point and the lower inverse TMR values observed in our junctions with respect to the case of upward polarization.

In conclusion, spin filtering of the BTO barrier selects tunnelling states on the base of the symmetry of the electron wave function. The specific symmetries allowed (Δ_1 and Δ_5) may account, in the case of a Fe electrode analyzed by means of a ferromagnetic half-metal such as LSMO, for the following features of the TMR versus bias curve:

1. Normal TMR for negative bias, due to the tunnelling of electronic states with symmetry Δ_1 from the majority-spin d_{z^2} band.

2. Inverse TMR for high enough positive bias, due to the tunnelling of electronic states with symmetry Δ_5 to the minority-spin states in the empty d_{xz}/d_{yz} bands above Fermi level.

3. Dependence of TMR sign and entity on BTO polarization, due to the variation of both d_{z^2} and d_{xz}/d_{yz} orbital DOS for opposite directions of ferroelectric polarization.

Chapter 6

Conclusions and Perspectives

In the present thesis work the investigation of composite multiferroic heterostructures exhibiting magnetoelectric coupling between ferroelectric and ferromagnetic materials is reported. Besides being a very intriguing phenomenon in fundamental condensed matter physics, electric control of magnetism may find application in the field of information storage technology, as it could be the key element to achieve energy-efficient, fast and nonvolatile writing in magnetic random access memories. The relative scarcity of single phase materials that present both magnetic and ferroelectric ordering at room temperature leads to investigate primarily composite systems made of ferroelectric/ferromagnetic heterostructures, like the ones described in the present thesis.

Two different approaches have been employed.

1. Ferroelectric control of perpendicular magnetic anisotropy in $CoFeB/BaTiO_3$ heterostructures

2. Ferroelectric control of spin polarization in $Fe/BaTiO_3/La_{0.67}Sr_{0.33}MnO_3$ tunnelling junctions

In the first approach, in order to investigate ferroelectric control of magnetic anisotropy, $CoFeB/BaTiO_3$ bilayers have been grown on $La_{0.67}Sr_{0.33}MnO_3//SrTiO_3$

(001) by pulsed laser deposition (oxides) and sputtering (metals). The thickness of the CoFeB layer has been proved to be a critical parameter for achieving perpendicular magnetic anisotropy (PMA) and for observing a seizable influence of the $BaTiO_3$ (BTO) polarization on the magnetic properties. In samples with CoFeB layer thickness of 1.1 nm, perpendicular magnetic anisotropy, essentially arising from symmetry breaking at the interface, is prevalent over other anisotropic effects, leading to out-of-plane remanent magnetization. In this work it has been shown that ferroelectric polarization affects the PMA, leading to a modulation of the coercive field of CoFeB, in the order of 30% at room temperature, when the BTO remanent polarization is switched from upward to downward (or viceversa).

In samples with nominal CoFeB layer thickness of 1.3 nm, instead, the volume contributions, in particular shape anisotropy, largely prevail. This results not only in a spin reorientation transition towards in-plane magnetization, but also in absence of any detectable variation of the anisotropy.

An equilibrium condition between competing in-plane and out-of-plane anisotropies should be in principle achievable by finely controlling the CoFeB layer thickness. This could allow, in principle, to determine not only coercivity, but also magnetization direction (parallel or perpendicular to the interface) by ferroelectric polarization. However, we found that the control and reproducibility of the heterostructure fabrication process is extremely crucial and, at the current stage, it does not possess a sufficient precision to achieve this goal.

Since the ferroelectric characterization performed on BTO capacitors has given a lower remanent polarization value (3 $\mu C/cm^2$) with respect to the state of the art (over 40 $\mu C/cm^2$) [94–96], a totally different approach could be to improve the ferroelectric remanent polarization acting on the $BaTiO_3$ film, in order to enhance the magnetoelectric effect observed.

Whatever will be the chosen path (improving the precision of the fabrication process or optimizing the BTO ferroelectric properties), finding a way to control

the direction of magnetic easy axis in a ferromagnetic thin film would set a milestone in the route of electrically controlled MRAM devices. As a matter of fact, the same principle could be extended, in principle, to multiferroic tunnelling junctions with structure $CoFeB/MgO/CoFeB/BaTiO_3$, where the magnetization of the first electrode is fixed and that of the second can be electrically switched through the $CoFeB/BaTiO_3$ magnetoelectric coupling, thus finally realizing a purely electrically controlled MRAM.

In the second approach proposed by this thesis work, a complete device based on the tunnelling junctions paradigm has been realized on the fully epitaxial stack $Au/Co/Fe/BaTiO_3/La_{0.67}Sr_{0.33}MnO_3$. The heterostructure has been grown *in situ* by pulsed laser deposition (oxides) and molecular beam epitaxy (metals) in a high-vacuum cluster tool, in order to preserve the interface quality. Thanks to the coexistence of tunnelling magnetoresistance (due to the two magnetic electrodes Co/Fe and $La_{0.67}Sr_{0.33}MnO_3$ separated by the BTO insulating barrier) and electroresistance (due to the ferroelectricity of the BTO barrier), the devices realized can exhibit four different states of resistance according to the two possible alignments (parallel and antiparallel) of the electrodes magnetization and to the two polarization directions in the barrier.

We found that tunnelling electroresistance values depend strongly on the ferroelectric barrier thickness, and range from 10% at 20 K for junctions with 2 nm thick barrier to over 100 % at room temperature for devices with 4 nm thick barrier. Tunnelling magnetoresistance values, instead, are in the order of 0.3-0.6%, suggesting that the two magnetic layers are not completely decoupled. Larger values of TMR could be expected upon optimization of the structure. A possible improvement in this direction may come simply by employing a thicker Co layer which should harden the magnetization in the top layer.

A peculiar bias dependence of TMR has been evidenced in devices with 2 nm ferroelectric barrier, with a change of TMR sign for small positive voltages. Both the inversion point (i. e. the bias voltage at which the TMR sign changes from

positive to negative) and the values of inverse TMR are affected by ferroelectric polarization, demonstrating actual magnetoelectric coupling.

A previous experimental work have already demonstrated magnetoelectric coupling mechanisms in $Fe/BaTiO_3/La_{0.67}Sr_{0.33}MnO_3$ junctions [26], but the multiferroic tunnelling junctions there described were not fully-epitaxial, differently from our junctions [68]. Moreover, only inverse TMR was initially predicted and observed for junctions of this kind with a 3d metal as top layer, while both in our samples with 2 nm and 3 nm barrier normal TMR is observed at zero bias.

A possible explanation of this behaviour has been given in terms of symmetry based spin filtering, predicted in $BaTiO_3$ barriers by first principles calculations [107, 108]. If this hypothesis were confirmed by further investigation, this would be the first demonstration of coherent tunnelling and spin filtering in $BaTiO_3$-based devices.

This would be particularly appealing since, as in the case of Fe/MgO/Fe tunnelling junctions [109], a specifically engineered device could employ spin-filtering of the barrier to achieve high value of TMR up to room temperature, which is fundamental for any industrial application. Before to conclude, it is worthwhile to stress that devices of this kind would benefit of the additional degree of freedom given by ferroelectric polarization, thus allowing the realization of a four-state memory, and in perspective the design of a four-values (0,1,2,3) logic, instead than the usual binary (0,1) one.

Bibliography

[1] V. Turner and J. F. Gantz, "The Digital Universe of Opportunities: Rich Data and the Increasing Value of the Internet of Things," IDC, Framingham, Tech. Rep. [Online]. Available: http://www.emc.com/leadership/digital-universe/index.htm

[2] G. Grynkewich, J. Åkerman, P. Brown, B. Butcher, R. Dave, M. DeHerrera, M. Durlam, B. Engel, J. Janesky, S. Pietambaram, N. Rizzo, J. Slaughter, K. Smith, J. Sun, and S. Tehrani, "Nonvolatile magnetoresistive random-access memory based on magnetic tunnel junctions," *MRS Bulletin*, vol. 29, pp. 818–821, 11 2004. [Online]. Available: http://journals.cambridge.org/article_S0883769400016754

[3] E. Grochowski and R. D. Halem, "Technological impact of magnetic hard disk drives on storage systems," *IBM Syst. J.*, vol. 42, no. 2, pp. 338–346, Apr. 2003. [Online]. Available: http://dx.doi.org/10.1147/sj.422.0338

[4] T. McGuire and R. Potter, "Anisotropic magnetoresistance in ferromagnetic 3d alloys," *Magnetics, IEEE Transactions on*, pp. 1018–1038, 1975. [Online]. Available: http://ieeexplore.ieee.org/xpls/abs_all.jsp?arnumber=1058782

[5] M. Baibich, J. Broto, A. Fert, and F. V. Dau, "Giant magnetoresistance of (001) Fe/(001) Cr magnetic superlattices," *Physical Review Letters*,

vol. 61, no. 001, pp. 2472–2475, 1988. [Online]. Available: http://journals.aps.org/prl/abstract/10.1103/PhysRevLett.61.2472

[6] M. Julliere, "Tunneling between ferromagnetic films," *Physics Letters A*, vol. 54, no. 3, pp. 225 – 226, 1975. [Online]. Available: http://www.sciencedirect.com/science/article/pii/0375960175901747

[7] C. Chappert, A. Fert, and F. N. Van Dau, "The emergence of spin electronics in data storage." *Nature materials*, vol. 6, no. 11, pp. 813–23, Nov. 2007. [Online]. Available: http://www.ncbi.nlm.nih.gov/pubmed/17972936

[8] S. Tehrani, E. Chen, M. Durlam, M. DeHerrera, J. M. Slaughter, J. Shi, and G. Kerszykowski, "High density submicron magnetoresistive random access memory (invited)," *Journal of Applied Physics*, vol. 85, no. 8, p. 5822, 1999. [Online]. Available: http://scitation.aip.org/content/aip/journal/jap/85/8/10.1063/1.369931

[9] S. Tehrani, B. Engel, J. Slaughter, E. Chen, M. DeHerrera, M. Durlam, P. Naji, R. Whig, J. Janesky, and J. Calder, "Recent developments in magnetic tunnel junction MRAM," *IEEE Transactions on Magnetics*, vol. 36, no. 5, pp. 2752–2757, 2000. [Online]. Available: http://ieeexplore.ieee.org/lpdocs/epic03/wrapper.htm?arnumber=908581

[10] R. Sousa and I. Prejbeanu, "Non-volatile magnetic random access memories (MRAM)," *Comptes Rendus Physique*, no. October, 2005. [Online]. Available: http://www.sciencedirect.com/science/article/pii/S1631070505001519

[11] A. V. Khvalkovskiy, D. Apalkov, S. Watts, R. Chepulskii, R. S. Beach, A. Ong, X. Tang, A. Driskill-Smith, W. H. Butler, P. B. Visscher, D. Lottis, E. Chen, V. Nikitin, and M. Krounbi, "Basic

principles of STT-MRAM cell operation in memory arrays," *Journal of Physics D: Applied Physics*, vol. 46, no. 13, p. 139601, Apr. 2013. [Online]. Available: http://stacks.iop.org/0022-3727/46/i=13/a=139601? key=crossref.de8de76f28baa2dc01864ee7497afbcf

[12] D. Ralph and M. Stiles, "Spin transfer torques," *Journal of Magnetism and Magnetic Materials*, vol. 320, no. 7, pp. 1190–1216, Apr. 2008. [Online]. Available: http://linkinghub.elsevier.com/retrieve/pii/S0304885307010116

[13] J. F. Scott, *Ferroelectric Memories.* Springer, 2000.

[14] Y. A. Hiroshi Ishiwara, Masanori Okuyama, *Ferroelectric Random Access Memories: Fundamentals and Applications.* Springer, 2004.

[15] V. Garcia and M. Bibes, "Ferroelectric tunnel junctions for information storage and processing." *Nature communications*, vol. 5, p. 4289, Jan. 2014. [Online]. Available: http://www.ncbi.nlm.nih.gov/pubmed/25056141

[16] Z. Wen, C. Li, D. Wu, A. Li, and N. Ming, "Ferroelectric-field-effect-enhanced electroresistance in metal/ferroelectric/semiconductor tunnel junctions." *Nature materials*, vol. 12, no. 7, pp. 617–21, Jul. 2013. [Online]. Available: http://www.ncbi.nlm.nih.gov/pubmed/23685861

[17] H. Yamada, V. Garcia, S. Fusil, and S. Boyn, "Giant electroresistance of super-tetragonal BiFeO3-based ferroelectric tunnel junctions," *ACS Nano*, no. 6, pp. 5385–5390, 2013. [Online]. Available: http://pubs.acs.org/doi/abs/10.1021/nn401378t

[18] A. Chanthbouala, V. Garcia, R. O. Cherifi, K. Bouzehouane, S. Fusil, X. Moya, S. Xavier, H. Yamada, C. Deranlot, N. D. Mathur, M. Bibes, A. Barthélémy, and J. Grollier, "A ferroelectric memristor." *Nature materials*, vol. 11, no. 10, pp. 860–4, Oct. 2012. [Online]. Available: http://www.ncbi.nlm.nih.gov/pubmed/22983431

[19] D. J. Kim, H. Lu, S. Ryu, C.-W. Bark, C.-B. Eom, E. Y. Tsymbal, and a. Gruverman, "Ferroelectric tunnel memristor." *Nano letters*, vol. 12, no. 11, pp. 5697–702, Nov. 2012. [Online]. Available: http://www.ncbi.nlm.nih.gov/pubmed/23039785

[20] A. Quindeau, D. Hesse, and M. Alexe, "Programmable ferroelectric tunnel memristor," *Frontiers in Physics*, vol. 2, no. February, pp. 1–5, 2014. [Online]. Available: http://journal.frontiersin.org/Journal/10.3389/fphy. 2014.00007/full

[21] M. Bibes, "Nanoferronics is a winning combination." *Nature materials*, vol. 11, no. 5, pp. 354–7, May 2012. [Online]. Available: http: //www.ncbi.nlm.nih.gov/pubmed/22522625

[22] N. a. Spaldin and M. Fiebig, "Materials science. The renaissance of magnetoelectric multiferroics." *Science (New York, N.Y.)*, vol. 309, no. 5733, pp. 391–2, Jul. 2005. [Online]. Available: http://www.ncbi.nlm.nih. gov/pubmed/16020720

[23] M. Fiebig, "Revival of the magnetoelectric effect," *Journal of Physics D: Applied Physics*, vol. 38, no. 8, pp. R123–R152, Apr. 2005. [Online]. Available: http://stacks.iop.org/0022-3727/38/i=8/a=R01?key=crossref. debaec7d983bfa8c9af8c02008b6e621

[24] N. a. Hill, "Why Are There so Few Magnetic Ferroelectrics?" *The Journal of Physical Chemistry B*, vol. 104, no. 29, pp. 6694–6709, Jul. 2000. [Online]. Available: http://pubs.acs.org/doi/abs/10.1021/jp000114x

[25] E. Y. Tsymbal, "Spintronics: Electric toggling of magnets." *Nature materials*, vol. 11, no. 1, pp. 12–3, Jan. 2012. [Online]. Available: http://www.ncbi.nlm.nih.gov/pubmed/22169910

[26] V. Garcia, M. Bibes, L. Bocher, S. Valencia, F. Kronast, a. Crassous, X. Moya, S. Enouz-Vedrenne, a. Gloter, D. Imhoff, C. Deranlot, N. D. Mathur, S. Fusil, K. Bouzehouane, and a. Barthélémy, "Ferroelectric control of spin polarization." *Science (New York, N.Y.)*, vol. 327, no. 5969, pp. 1106–1110, Feb. 2010. [Online]. Available: http://www.ncbi.nlm.nih.gov/pubmed/20075211

[27] S. M. Wu, S. a. Cybart, P. Yu, M. D. Rossell, J. X. Zhang, R. Ramesh, and R. C. Dynes, "Reversible electric control of exchange bias in a multiferroic field-effect device." *Nature materials*, vol. 9, no. 9, pp. 756–61, Sep. 2010. [Online]. Available: http://www.ncbi.nlm.nih.gov/pubmed/20657590

[28] Y.-W. Yin, M. Raju, W.-J. Hu, X.-J. Weng, K. Zou, J. Zhu, X.-G. Li, Z.-D. Zhang, and Q. Li, "Multiferroic tunnel junctions," *Frontiers of Physics*, vol. 7, no. 4, pp. 380–385, Aug. 2012. [Online]. Available: http://link.springer.com/10.1007/s11467-012-0266-8

[29] D. Pantel, S. Goetze, D. Hesse, and M. Alexe, "Reversible electrical switching of spin polarization in multiferroic tunnel junctions." *Nature materials*, vol. 11, no. 4, pp. 289–93, Apr. 2012. [Online]. Available: http://www.ncbi.nlm.nih.gov/pubmed/22367005

[30] G. Radaelli, D. Petti, E. Plekhanov, I. Fina, P. Torelli, B. R. Salles, M. Cantoni, C. Rinaldi, D. Gutiérrez, G. Panaccione, M. Varela, S. Picozzi, J. Fontcuberta, and R. Bertacco, "Electric control of magnetism at the Fe/BaTiO3 interface." *Nature communications*, vol. 5, p. 3404, Jan. 2014. [Online]. Available: http://www.ncbi.nlm.nih.gov/pubmed/24584546

[31] M. Bibes and A. Barthélémy, "Towards a magnetoelectric memory," *Nat. Mater*, vol. 7, no. June, pp. 7–8, 2008. [Online]. Available: http://www.matdl.org/matdlwiki/images/9/91/Magnetoelectric_memory.pdf

[32] H. Zheng, J. Wang, S. E. Lofland, Z. Ma, L. Mohaddes-Ardabili, T. Zhao, L. Salamanca-Riba, S. R. Shinde, S. B. Ogale, F. Bai, D. Viehland, Y. Jia, D. G. Schlom, M. Wuttig, a. Roytburd, and R. Ramesh, "Multiferroic BaTiO3-CoFe2O4 Nanostructures." *Science (New York, N.Y.)*, vol. 303, no. 5658, pp. 661–3, Jan. 2004. [Online]. Available: http://www.ncbi.nlm.nih.gov/pubmed/14752158

[33] S. Sahoo, S. Polisetty, and C. Duan, "Ferroelectric control of magnetism in Ba Ti O 3/Fe heterostructures via interface strain coupling," *Physical Review B*, 2007. [Online]. Available: http://journals.aps.org/prb/abstract/10.1103/PhysRevB.76.092108

[34] S. Brivio, D. Petti, R. Bertacco, and J. C. Cezar, "Electric field control of magnetic anisotropies and magnetic coercivity in Fe/BaTiO[sub 3](001) heterostructures," *Applied Physics Letters*, vol. 98, no. 9, p. 092505, 2011. [Online]. Available: http://scitation.aip.org/content/aip/journal/apl/98/9/10.1063/1.3554432

[35] S. Geprags, A. Brandlmaier, M. Opel, R. Gross, and S. T. B. Goennenwein, "Electric field controlled manipulation of the magnetization in Ni/BaTiO[sub 3] hybrid structures," *Applied Physics Letters*, vol. 96, no. 14, p. 142509, 2010. [Online]. Available: http://scitation.aip.org/content/aip/journal/apl/96/14/10.1063/1.3377923

[36] S. Zhang, Y. G. Zhao, P. S. Li, J. J. Yang, S. Rizwan, J. X. Zhang, J. Seidel, T. L. Qu, Y. J. Yang, Z. L. Luo, Q. He, T. Zou, Q. P. Chen, J. W. Wang, L. F. Yang, Y. Sun, Y. Z. Wu, X. Xiao, X. F. Jin, J. Huang, C. Gao, X. F. Han, and R. Ramesh, "Electric-field control of nonvolatile magnetization in $co_{40}fe_{40}b_{20}/Pb(mg_{1/3}nb_{2/3})_{0.7}ti_{0.3}o_3$ structure at room temperature," *Phys. Rev. Lett.*, vol. 108, p. 137203, Mar 2012. [Online]. Available: http://link.aps.org/doi/10.1103/PhysRevLett.108.137203

[37] H. J. a. Molegraaf, J. Hoffman, C. a. F. Vaz, S. Gariglio, D. van der Marel, C. H. Ahn, and J.-M. Triscone, "Magnetoelectric Effects in Complex Oxides with Competing Ground States," *Advanced Materials*, vol. 21, no. 34, pp. 3470–3474, Sep. 2009. [Online]. Available: http://doi.wiley.com/10.1002/adma.200900278

[38] Y. Sun, J. D. Burton, and E. Y. Tsymbal, "Electrically driven magnetism on a Pd thin film," *Physical Review B*, vol. 81, no. 6, p. 064413, Feb. 2010. [Online]. Available: http://link.aps.org/doi/10.1103/PhysRevB.81.064413

[39] C. G. Duan, S. S. Jaswal, and E. Y. Tsymbal, "Predicted magnetoelectric effect in Fe/BaTiO3 multilayers: Ferroelectric control of magnetism," *Physical Review Letters*, vol. 97, no. 4, p. 047201, Jul. 2006. [Online]. Available: http://link.aps.org/doi/10.1103/PhysRevLett.97.047201

[40] M. Fechner, I. V. Maznichenko, S. Ostanin, A. Ernst, J. Henk, P. Bruno, and I. Mertig, "Magnetic phase transition in two-phase multiferroics predicted from first principles," *Phys. Rev. B*, vol. 78, p. 212406, Dec 2008. [Online]. Available: http://link.aps.org/doi/10.1103/PhysRevB.78.212406

[41] J. P. Velev, C.-G. Duan, K. D. Belashchenko, S. S. Jaswal, and E. Y. Tsymbal, "Effects of ferroelectricity and magnetism on electron and spin transport in Fe/BaTiO3/Fe multiferroic tunnel junctions," *Journal of Applied Physics*, vol. 103, no. 7, p. 07A701, 2008. [Online]. Available: http://scitation.aip.org/content/aip/journal/jap/103/7/10.1063/1.2828512

[42] L. Bocher, A. Gloter, A. Crassous, and V. Garcia, "Atomic and electronic structure of the BaTiO3/Fe interface in multiferroic tunnel junctions," *Nano letters*, vol. 12, no. 1, pp. 376–382, 2011. [Online]. Available: http://pubs.acs.org/doi/abs/10.1021/nl203657c

[43] S. Valencia, A. Crassous, L. Bocher, V. Garcia, X. Moya, R. O. Cherifi, C. Deranlot, K. Bouzehouane, S. Fusil, A. Zobelli, A. Gloter, N. D. Mathur, A. Gaupp, R. Abrudan, F. Radu, A. Barthélémy, and M. Bibes, "Interface-induced room-temperature multiferroicity in BaTiO3." *Nature materials*, vol. 10, no. 10, pp. 753–8, Oct. 2011. [Online]. Available: http://www.ncbi.nlm.nih.gov/pubmed/21857674

[44] P. Bruno, "Theory of interlayer magnetic coupling," *Physical Review B*, vol. 52, no. 1, 1995. [Online]. Available: http://journals.aps.org/prb/abstract/10.1103/PhysRevB.52.411

[45] M. Fechner, P. Zahn, S. Ostanin, M. Bibes, and I. Mertig, "Switching magnetization by 180° with an electric field," *Phys. Rev. Lett.*, vol. 108, p. 197206, May 2012. [Online]. Available: http://link.aps.org/doi/10.1103/PhysRevLett.108.197206

[46] A. Manuzzi, "Electric Control of the Perpendicular Magnetic Anisotropy in CoFeB/BaTiO3 Heterostructures," Master's thesis, Politecnico di Milano, 2013.

[47] M. Gajek, M. Bibes, S. Fusil, K. Bouzehouane, J. Fontcuberta, A. Barthélémy, and A. Fert, "Tunnel junctions with multiferroic barriers." *Nature materials*, vol. 6, no. 4, pp. 296–302, Apr. 2007. [Online]. Available: http://www.ncbi.nlm.nih.gov/pubmed/17351615

[48] J. Coey, *Magnetism and Magentic Materials*. Cambridge University Press, 2010.

[49] S. Blundell, *Magnetism in Condensed Matter*. Oxford University Press, 2004.

[50] J. M. D. Coey and M. Venkatesan, "Half-metallic ferromagnetism: Example of CrO2," *Journal of Applied Physics*, vol. 91, no. 10, p. 8345,

2002. [Online]. Available: http://scitation.aip.org/content/aip/journal/jap/91/10/10.1063/1.1447879

[51] G. Binasch, P. Grünberg, F. Saurenbach, and W. Zinn, "Enhanced magnetoresistance in layered magnetic structures with antiferromagnetic interlayer exchange," *Physical review B*, vol. 39, no. 7, pp. 4828–4830, 1989. [Online]. Available: http://journals.aps.org/prb/abstract/10.1103/PhysRevB.39.4828

[52] S. Parkin, X. Jiang, and C. Kaiser, "Magnetically engineered spintronic sensors and memory," *Proceedings of the IEEE*, vol. 91, no. 5, 2003. [Online]. Available: http://ieeexplore.ieee.org/xpls/abs_all.jsp?arnumber=1200120

[53] S. Ikeda, J. Hayakawa, Y. Ashizawa, Y. M. Lee, K. Miura, H. Hasegawa, M. Tsunoda, F. Matsukura, and H. Ohno, "Tunnel magnetoresistance of 604% at 300 K by suppression of Ta diffusion in CoFeB/MgO/CoFeB pseudo-spin-valves annealed at high temperature," *Applied Physics Letters*, vol. 93, no. 8, p. 082508, 2008. [Online]. Available: http://scitation.aip.org/content/aip/journal/apl/93/8/10.1063/1.2976435

[54] K. M. Rabe, M. Dawber, C. Lichtensteiger, C. H. Ahn, and T. Jean-Marc, *Physics of Ferroelectics. A Modern Perspective.* Springer, 2007, ch. Modern Physics of Ferroelectrics: Essential Background.

[55] K. M. Ok, E. O. Chi, and P. S. Halasyamani, "Bulk characterization methods for non-centrosymmetric materials: second-harmonic generation, piezoelectricity, pyroelectricity, and ferroelectricity." *Chemical Society reviews*, vol. 35, no. 8, pp. 710–7, Aug. 2006. [Online]. Available: http://www.ncbi.nlm.nih.gov/pubmed/16862271

[56] N. A. Spaldin, *Physics of Ferroelectics. A Modern Perspective.* Springer, 2007, ch. Analogies and Differences between Ferroelectrics and Ferromagnets.

[57] K. M. Rabe, W. Zhong, and D. Vanderbilt, "Phase Transition in BaTiO3 from First Principles," *Physical Review Letters*, vol. 73, no. 13, pp. 1861–1864, 1994.

[58] L. Esaki, R. B. Laibowitz, and P. J. Stiles, "Polar switch," *IBM Tech. Discl. Bull*, vol. 13, p. 2161, 1971.

[59] D. D. Fong, G. B. Stephenson, S. K. Streiffer, J. A. Eastman, O. Auciello, P. H. Fuoss, and C. Thompson, "Ferroelectricity in ultrathin perovskite films," *Science*, vol. 304, no. 5677, pp. 1650–1653, 2004. [Online]. Available: http://www.sciencemag.org/content/304/5677/1650.abstract

[60] C. Lichtensteiger, J.-M. Triscone, J. Junquera, and P. Ghosez, "Ferroelectricity and tetragonality in ultrathin $pbtio_3$ films," *Phys. Rev. Lett.*, vol. 94, p. 047603, Feb 2005. [Online]. Available: http://link.aps.org/doi/10.1103/PhysRevLett.94.047603

[61] E. Y. Tsymbal and H. Kohlstedt, "Applied physics. Tunneling across a ferroelectric." *Science (New York, N.Y.)*, vol. 313, no. 5784, pp. 181–3, Jul. 2006. [Online]. Available: http://www.ncbi.nlm.nih.gov/pubmed/16840688

[62] W. F. Brinkman, "Tunneling Conductance of Asymmetrical Barriers," *Journal of Applied Physics*, vol. 41, no. 5, p. 1915, 1970. [Online]. Available: http://scitation.aip.org/content/aip/journal/jap/41/5/10.1063/1.1659141

[63] a. Gruverman, D. Wu, H. Lu, Y. Wang, H. W. Jang, C. M. Folkman, M. Y. Zhuravlev, D. Felker, M. Rzchowski, C.-B. Eom, and E. Y. Tsymbal, "Tunneling electroresistance effect in ferroelectric tunnel junctions at the

nanoscale." *Nano letters*, vol. 9, no. 10, pp. 3539–43, Oct. 2009. [Online]. Available: http://www.ncbi.nlm.nih.gov/pubmed/19697939

[64] A. Chanthbouala, A. Crassous, V. Garcia, K. Bouzehouane, S. Fusil, X. Moya, J. Allibe, B. Dlubak, J. Grollier, S. Xavier, C. Deranlot, A. Moshar, R. Proksch, N. D. Mathur, M. Bibes, and A. Barthélémy, "Solid-state memories based on ferroelectric tunnel junctions." *Nature nanotechnology*, vol. 7, no. 2, pp. 101–4, Feb. 2012. [Online]. Available: http://www.ncbi.nlm.nih.gov/pubmed/22138863

[65] G. Radaelli, D. Gutiérrez, F. Sánchez, R. Bertacco, M. Stengel, and J. Fontcuberta, "Large room-temperature electroresistance by dual-modulated ferroelectric tunnel barriers," *to be published*.

[66] W. Eerenstein, N. D. Mathur, and J. F. Scott, "Multiferroic and magnetoelectric materials." *Nature*, vol. 442, no. 7104, pp. 759–65, Aug. 2006. [Online]. Available: http://www.ncbi.nlm.nih.gov/pubmed/16915279

[67] H. Schmid, *Introduction to Complex Mediums for Optics and Electromagnetics*. SPIE, 2003, ch. Magnetoelectric effects in insulating magnetic materials.

[68] G. Radaelli, M. Cantoni, L. Lijun, M. Espahbodi, and R. Bertacco, "Two dimensional growth of ultrathin Fe films on BaTiO3 with sharp chemical interface," *Journal of Applied Physics*, vol. 115, no. 6, p. 063501, Feb. 2014. [Online]. Available: http://scitation.aip.org/content/aip/journal/jap/115/6/10.1063/1.4864375

[69] C. G. Duan, J. P. Velev, R. F. Sabirianov, W. N. Mei, S. S. Jaswal, and E. Y. Tsymbal, "Tailoring magnetic anisotropy at the ferromagnetic/ferroelectric interface," *Applied Physics Letters*, vol. 92,

no. 12, p. 122905, 2008. [Online]. Available: http://scitation.aip.org/
content/aip/journal/apl/92/12/10.1063/1.2901879

[70] P. V. Lukashev, J. D. Burton, S. S. Jaswal, and E. Y. Tsymbal,
"Ferroelectric control of the magnetocrystalline anisotropy of the
Fe/BaTiO(3)(001) interface." *Journal of physics. Condensed matter : an
Institute of Physics journal*, vol. 24, no. 22, p. 226003, Jun. 2012. [Online].
Available: http://www.ncbi.nlm.nih.gov/pubmed/22551672

[71] Néel, Louis, "Anisotropie magnétique superficielle et surstructures
d'orientation," *J. Phys. Radium*, vol. 15, no. 4, pp. 225–239, 1954. [Online].
Available: http://dx.doi.org/10.1051/jphysrad:01954001504022500

[72] H. J. Richter, "The transition from longitudinal to perpendicular record-
ing," *JOURNAL OF PHYSICS D: APPLIED PHYSIC*, vol. 409, pp. R149–
R177, 2007.

[73] F. Zavaliche, T. Zhao, H. Zheng, F. Straub, M. P. Cruz, P.-L. Yang, D. Hao,
and R. Ramesh, "Electrically Assisted Magnetic Recording in Multiferroic
Nanostructures," *Nano Letters*, vol. 7, no. 6, pp. 1586–1590, 2007, pMID:
17497818. [Online]. Available: http://dx.doi.org/10.1021/nl070465o

[74] a. Mardana, S. Ducharme, and S. Adenwalla, "Ferroelectric control of
magnetic anisotropy." *Nano letters*, vol. 11, no. 9, pp. 3862–7, Sep. 2011.
[Online]. Available: http://www.ncbi.nlm.nih.gov/pubmed/21823660

[75] S. Ikeda, K. Miura, H. Yamamoto, K. Mizunuma, H. D. Gan,
M. Endo, S. Kanai, J. Hayakawa, F. Matsukura, and H. Ohno, "A
perpendicular-anisotropy CoFeB–MgO magnetic tunnel junction," *Nat
Mater*, vol. 9, no. 9, pp. 721–724, Sep. 2010. [Online]. Available:
http://dx.doi.org/10.1038/nmat2804

[76] D. C. Worledge, G. Hu, D. W. Abraham, J. Z. Sun, P. L. Trouilloud, J. Nowak, S. Brown, M. C. Gaidis, E. J. O'Sullivan, and R. P. Robertazzi, "Spin torque switching of perpendicular Ta/CoFeB/MgO-based magnetic tunnel junctions," *Applied Physics Letters*, vol. 98, no. 2, p. 022501, 2011. [Online]. Available: http://scitation.aip.org/content/aip/journal/apl/98/2/10.1063/1.3536482

[77] K. Lee, J. J. Sapan, S. H. Kang, and E. E. Fullerton, "Perpendicular magnetization of CoFeB on single-crystal MgO," *Journal of Applied Physics*, vol. 109, no. 12, p. 123910, 2011. [Online]. Available: http://scitation.aip.org/content/aip/journal/jap/109/12/10.1063/1.3592986

[78] W. X. Wang, Y. Yang, H. Naganuma, Y. Ando, R. C. Yu, and X. F. Han, "The perpendicular anisotropy of Co40Fe40B20 sandwiched between Ta and MgO layers and its application in CoFeB/MgO/CoFeB tunnel junction," *Applied Physics Letters*, vol. 99, no. 1, p. 012502, 2011. [Online]. Available: http://scitation.aip.org/content/aip/journal/apl/99/1/10.1063/1.3605564

[79] V. B. Naik, H. Meng, and R. Sbiaa, "Thick CoFeB with perpendicular magnetic anisotropy in CoFeB-MgO based magnetic tunnel junction," *AIP Advances*, vol. 2, no. 4, p. 042182, 2012. [Online]. Available: http://scitation.aip.org/content/aip/journal/adva/2/4/10.1063/1.4771996

[80] R. Bertacco, M. Cantoni, M. Riva, a. Tagliaferri, and F. Ciccacci, "Epitaxial growth and characterization of layered magnetic nanostructures," *Applied Surface Science*, vol. 252, no. 5, pp. 1754–1764, Dec. 2005. [Online]. Available: http://linkinghub.elsevier.com/retrieve/pii/S0169433205005787

[81] L. W. Martin, Y. Chu, and R. Ramesh, "Advances in the growth and characterization of magnetic , ferroelectric , and multiferroic oxide thin films," *Materials Science & Engineering R*, vol. 68, no. 4-6, pp. 89–133, 2010. [Online]. Available: http://dx.doi.org/10.1016/j.mser.2010.03.001

[82] G. Radaelli, S. Brivio, I. Fina, and R. Bertacco, "Correlation between growth dynamics and dielectric properties of epitaxial BaTiO3 films," *Applied Physics Letters*, vol. 100, no. 10, p. 102904, 2012. [Online]. Available: http://scitation.aip.org/content/aip/journal/apl/100/10/10.1063/1.3692732

[83] J. Greer, "Large-area commercial pulsed laser deposition," in *Pulsed Laser Deposition of Thin Films*, 2006, pp. 191–214. [Online]. Available: http://books.google.com/books?hl=en&lr=&id=0jIO3cwkiOIC&oi=fnd&pg=PA191&dq=Large-Area+Commercial+Pulsed+Laser+Deposition&ots=PWKU9B3OWF&sig=WBKsF8qYzDGW-6QbwTZVA1_g9Yk

[84] C. B. Sawyer and C. H. Tower, "Rochelle salt as a dielectric," *Phys. Rev.*, vol. 35, pp. 269–273, Feb 1930. [Online]. Available: http://link.aps.org/doi/10.1103/PhysRev.35.269

[85] A. Herpers, "Electrical characterization of manganite and titanate heterostructures," PhD thesis, Rheinisch-Westfälischen Technischen Hochschule Aachen, 2014. [Online]. Available: http://books.google.com/books?hl=en&lr=&id=CEwyAwAAQBAJ&oi=fnd&pg=PA1&dq=Electrical+characterization+of+manganite+and+titanate+heterostructures&ots=ie8palPfvK&sig=yWkWNrJHhUmPf00fL-W0aFCsGRw

[86] J. F. Scott, "Ferroelectrics go bananas," *Journal of Physics: Condensed Matter*, vol. 20, no. 2, p. 021001, Jan. 2008. [Online]. Available: http://stacks.iop.org/0953-8984/20/i=2/a=021001?key=crossref.b02da526674ad3581b148f43ec7683c0

[87] I. F. Martínez, "Ferroelectricity and magnetoelectric coupling in magnetic ferroelectrics and artificial multiferroic heterostructures,"

PhD thesis, Universitat de Barcelona, 2012. [Online]. Available: http://www.tdx.cat/handle/10803/81981

[88] P. Vavassori, "Polarization modulation technique for magneto-optical quantitative vector magnetometry," *Applied Physics Letters*, vol. 77, no. 11, p. 1605, 2000. [Online]. Available: http://scitation.aip.org/content/ aip/journal/apl/77/11/10.1063/1.1310169

[89] S. V. Karthik, Y. K. Takahashi, T. Ohkubo, K. Hono, S. Ikeda, and H. Ohno, "Transmission electron microscopy investigation of CoFeB/MgO/CoFeB pseudospin valves annealed at different temperatures," *Journal of Applied Physics*, vol. 106, no. 2, p. 023920, 2009. [Online]. Available: http://scitation.aip.org/content/aip/journal/jap/106/ 2/10.1063/1.3182817

[90] T. Miyajima, T. Ibusuki, S. Umehara, M. Sato, S. Eguchi, M. Tsukada, and Y. Kataoka, "Transmission electron microscopy study on the crystallization and boron distribution of CoFeB/MgO/CoFeB magnetic tunnel junctions with various capping layers," *Applied Physics Letters*, vol. 94, no. 12, p. 122501, 2009. [Online]. Available: http://scitation.aip.org/content/aip/ journal/apl/94/12/10.1063/1.3106624

[91] a. a. Greer, a. X. Gray, S. Kanai, a. M. Kaiser, S. Ueda, Y. Yamashita, C. Bordel, G. Palsson, N. Maejima, S.-H. Yang, G. Conti, K. Kobayashi, S. Ikeda, F. Matsukura, H. Ohno, C. M. Schneider, J. B. Kortright, F. Hellman, and C. S. Fadley, "Observation of boron diffusion in an annealed Ta/CoFeB/MgO magnetic tunnel junction with standing-wave hard x-ray photoemission," *Applied Physics Letters*, vol. 101, no. 20, p. 202402, 2012. [Online]. Available: http: //scitation.aip.org/content/aip/journal/apl/101/20/10.1063/1.4766351

[92] M. Bozgeyik, "Frequency Dependent Ferroelectric Properties of BaZrO3 Modified Sr0.8Bi2.2Ta2O9 Thin Films," *Chinese Journal of Physics*, vol. 51, no. 2, pp. 327–336, 2013. [Online]. Available: http://psroc.phys. ntu.edu.tw/cjp/download.php?type=full&vol=51&num=2&page=327

[93] S. M. Nakhmanson, K. M. Rabe, and D. Vanderbilt, "Polarization enhancement in two-and three-component ferroelectric superlattices," *Applied Physics Letters*, vol. 8019, pp. 1–4, 2005. [Online]. Available: http://ieeexplore.ieee.org/xpls/abs_all.jsp?arnumber=4816533

[94] N. Yanase, K. Abe, N. Fukushima, and T. Kawakubo, "Thickness dependence of ferroelectricity in heteroepitaxial BaTiO3 thin film capacitors," *Japanese Journal of Applied Physics*, vol. 5305, 1999. [Online]. Available: http://iopscience.iop.org/1347-4065/38/9S/5305

[95] D. J. Kim, J. Y. Jo, Y. S. Kim, Y. J. Chang, J. S. Lee, J.-G. Yoon, T. K. Song, and T. W. Noh, "Polarization relaxation induced by a depolarization field in ultrathin ferroelectric batio$_3$ capacitors," *Phys. Rev. Lett.*, vol. 95, p. 237602, Dec 2005. [Online]. Available: http://link.aps.org/doi/10.1103/PhysRevLett.95.237602

[96] a. Petraru, N. a. Pertsev, H. Kohlstedt, U. Poppe, R. Waser, a. Solbach, and U. Klemradt, "Polarization and lattice strains in epitaxial BaTiO[sub 3] films grown by high-pressure sputtering," *Journal of Applied Physics*, vol. 101, no. 11, p. 114106, 2007. [Online]. Available: http: //scitation.aip.org/content/aip/journal/jap/101/11/10.1063/1.2745277

[97] M. Bowen, M. Bibes, and A. Barthélémy, "Nearly total spin polarization in La2/3Sr1/3MnO3 from tunneling experiments," *Applied Physics Letters*, no. 001, pp. 10–12, 2003. [Online]. Available: http: //scitation.aip.org/content/aip/journal/apl/82/2/10.1063/1.1534619

[98] S. Brivio, C. Rinaldi, D. Petti, R. Bertacco, and F. Sanchez, "Epitaxial growth of Fe/BaTiO3 heterostructures," *Thin Solid Films*, vol. 519, no. 17, pp. 5804–5807, Jun. 2011. [Online]. Available: http://linkinghub.elsevier.com/retrieve/pii/S0040609010018596

[99] M. Viret, M. Drouet, and J. Nassar, "Low-field colossal magnetoresistance in manganite tunnel spin valves," *EPL (Europhysics letters)*, vol. 545, 1997. [Online]. Available: http://iopscience.iop.org/0295-5075/39/5/545

[100] V. C. Lo, "Modeling the role of oxygen vacancy on ferroelectric properties in thin films," *Journal of Applied Physics*, vol. 92, no. 11, p. 6778, 2002. [Online]. Available: http://scitation.aip.org/content/aip/journal/jap/92/11/10.1063/1.1520718

[101] I. Vera Marún, F. Postma, J. Lodder, and R. Jansen, "Tunneling magnetoresistance with positive and negative sign in La0.67Sr0.33MnO3/SrTiO3/Co junctions," *Physical Review B*, vol. 76, no. 6, p. 064426, Aug. 2007. [Online]. Available: http://link.aps.org/doi/10.1103/PhysRevB.76.064426

[102] M. Sharma, S. Wang, and J. Nickel, "Inversion of Spin Polarization and Tunneling Magnetoresistance in Spin-Dependent Tunneling Junctions," *Physical Review Letters*, vol. 82, no. 3, pp. 616–619, Jan. 1999. [Online]. Available: http://link.aps.org/doi/10.1103/PhysRevLett.82.616

[103] J. D. Teresa, A. Barthélémy, and A. Fert, "Inverse tunnel magnetoresistance in Co/SrTiO 3/La 0.7 Sr 0.3 MnO 3: new ideas on spin-polarized tunneling," *Physical Review Letters*, pp. 80–83, 1999. [Online]. Available: http://journals.aps.org/prl/abstract/10.1103/PhysRevLett.82.4288

[104] C. Tiusan, C. Bellouard, M. Hehn, E. Jouguelet, and A. Schuhl, "Interfacial Resonance State Probed by Spin-Polarized Tunneling in

Epitaxial Fe/MgO/Fe Tunnel Junctions," *Physical Review Letters*, no. September, pp. 3–6, 2004. [Online]. Available: http://journals.aps.org/prl/abstract/10.1103/PhysRevLett.93.106602

[105] M. a. Tanaka, T. Hori, S. Hori, K. Kondou, S. Kasai, T. Ono, and K. Mibu, "Bias-voltage-dependence of magnetoresistance for epitaxial Fe/MgO/Co 2 MnSn tunnel junctions," *Journal of Physics: Conference Series*, vol. 266, p. 012107, Jan. 2011. [Online]. Available: http://stacks.iop.org/1742-6596/266/i=1/a=012107?key=crossref.2a2f33be1316e8f04a0db1ddb112895d

[106] A. Kalitsov and P. Zermatten, "Bias dependence of tunneling magnetoresistance in magnetic tunnel junctions with asymmetric barriers," *Journal of Physics: Condensed Matter*, vol. 25, no. 49, pp. 1–8, 2013. [Online]. Available: http://iopscience.iop.org/0953-8984/25/49/496005

[107] J. P. Velev, C.-G. Duan, J. D. Burton, A. Smogunov, M. K. Niranjan, E. Tosatti, S. S. Jaswal, and E. Y. Tsymbal, "Magnetic tunnel junctions with ferroelectric barriers: prediction of four resistance States from first principles." *Nano letters*, vol. 9, no. 1, pp. 427–32, Jan. 2009. [Online]. Available: http://www.ncbi.nlm.nih.gov/pubmed/19113889

[108] N. M. Caffrey, T. Archer, I. Rungger, and S. Sanvito, "Coexistance of giant tunneling electroresistance and magnetoresistance in an all-oxide composite magnetic tunnel junction," *Phys. Rev. Lett.*, vol. 109, p. 226803, Nov 2012. [Online]. Available: http://link.aps.org/doi/10.1103/PhysRevLett.109.226803

[109] C. Tiusan, F. Greullet, M. Hehn, F. Montaigne, S. Andrieu, and a. Schuhl, "Spin tunnelling phenomena in single-crystal magnetic tunnel junction systems," *Journal of Physics: Condensed Matter*, vol. 19, no. 16, p. 165201, Apr. 2007. [Online]. Available: http://stacks.iop.org/0953-8984/19/i=16/a=165201?key=crossref.5ec861b5e9ba3de12aed528784f27f09